

HIGH-THROUGHPUT PARTICLE/CELL SEPARATION USING PRESSURE DIFFERENCE
AND QUASI INERTIAL FOCUSING IN CURVILINEAR PARALLEL MICROCHANNEL

A Thesis

by

BYUNG-HEE CHOI

Submitted to the Office of Graduate and Professional Studies of
Texas A&M University
in partial fulfillment of the requirements for the degree of

MASTER OF SCIENCE

Chair of Committee,	Victor M. Ugaz
Committee Members,	Hung-Jen Wu
	Arul Jayaraman
	Yassin A. Hassan
Head of Department,	M. Nazmul Karim

May 2018

Major Subject: Chemical Engineering

Copyright 2018 Byung-Hee Choi

ABSTRACT

A microfluidic filtration device based on the configuration of two curved parallel lanes connected through a narrow bridge is investigated in this study. The bridge is oriented perpendicular to the main flow direction, making it possible to operate the device at high throughput without clogging. A pressure difference established between these parallel lanes produces fluid transfer across the bridge, while also enabling the migration of particles smaller than the bridge height and retaining and enriching bigger particles. In addition, Dean vortices, induced in the curved segment of the channel, can be used to enhance separation efficiency in this design. The device will be employed for separating and enriching circulating tumor cells (CTCs) from blood components such as red blood cells (RBCs) and white blood cells (WBCs).

Separation efficiency of the filtration system is quantified by computational simulation, which has rarely been conducted until now. To do so, full 3D flow and particle simulations are conducted by using STAR-CCM+ software. The Saffman lift force, two-way coupling, and discrete element method (DEM) are considered in the particle simulation to obtain accurate results. This approach allows us to rationally optimize channel design in terms of separation efficiency, which can be quantified by simulating hundreds of particle trajectories within the separation device. Geometry and operation parameters, such as flow-rate, inlet length, and particle size, are investigated in terms of particle separation efficiency. Preliminary simulation results indicate the presence of unexpected quasi-inertial focusing observed in the curved segment of the flow path. Depending on the particle size, this focusing effect can reduce separation efficiency by limiting entry into the narrow bridge region, as well as offering an alternative explanation to conventional inertial focusing in curved channels. Preliminary experiments yield results comparable to the

computational simulation. These findings reveal how the device design can be optimized for CTC enrichment by controlling the extent of inertial focusing experienced by each species to be separated. Future work will focus on applying these insights to demonstrate high-throughput isolation and enrichment of CTCs from whole blood.

DEDICATION

To my loving parents and sister

ACKNOWLEDGEMENTS

I would like to thank my committee chair, Dr. Ugaz, and my committee members, Dr. Wu, Dr. Jayaraman, Dr. Hassan.

I would like to thank to Dr. Contreras Naranjo. I could complete this course under his guidance.

Thanks to my friends and colleagues. I could endure this program with them.

Finally, thanks to my mother, father and sister for their encouragement and limitless support.

CONTRIBUTORS AND FUNDING SOURCES

This work was supported by a thesis committee consisting of Professor Victor M. Ugaz(Advisor), Hung-Jen Wu and Arul Jayaraman of the Department of Chemical Engineering and Professor Yassin A. Hassan of the Department of Nuclear Engineering.

Fabrication of microfluidic device employed in Section 5 is conducted by Design 1 Solution, LLC and design of experiment in Section 5 was guided by Dr. Jose Clemente Contreras-Naranjo of the Department of Chemical Engineering.

All other work conducted for the thesis was completed by the student independently.

Graduate study was supported by the Cancer Prevention & Research Institute of Texas under grant number RP150421.

TABLE OF CONTENTS

	Page
ABSTRACT.....	ii
DEDICATION.....	iv
ACKNOWLEDGEMENTS.....	v
CONTRIBUTORS AND FUNDING SOURCES.....	vi
TABLE OF CONTENTS.....	vii
LIST OF FIGURES.....	ix
LIST OF TABLES.....	xiii
1. INTRODUCTION.....	1
2. BACKGROUND KNOWLEDGE.....	5
2.1 Fundamental parameters.....	5
2.2 Forces acting on particles.....	7
2.3 Microfiltration.....	24
2.4 Inertial focusing.....	27
2.5 Characteristics of the particles.....	44
3. PARTICLE SIMULATION.....	46
3.1 Channel design and particles for simulation.....	46
3.2 Separation efficiency: performance indicator.....	47
3.3 Simulation methods.....	48
3.4 What parameters are important for particle separation?.....	50
3.5 Conclusion.....	69
4. PRESSURE MODELING AND SIMULATION.....	71
4.1 Hagen-Poiseuille equation.....	71
4.2 Electric circuit analogy model for estimating pressure distribution.....	75
4.3 Conclusion.....	80
5. EXPERIMENT.....	84
5.1 Fabrication of the channel.....	84
5.2 Particle separation test.....	89
5.3 Imaging investigation.....	95
5.4 Conclusion.....	113

6. SUMMARY AND FUTURE WORK	116
6.1 Investigation of the effect of curve segment	116
6.2 New fluid path design	120
6.3 Improvement of channel fabrication	126
6.4 Multiple enrichment stages for CTCs	132
6.5 Experiment plan	141
REFERENCES	143
APPENDIX.....	153

LIST OF FIGURES

	Page
Figure 2-1 Schematic diagram for particles and surrounding flow in microchannel	8
Figure 2-2 Schematic diagram for shear-gradient-induced lift force.....	14
Figure 2-3 Pressure contour in the proximity of wall and particles.....	15
Figure 2-4 Filtration methods	25
Figure 2-5 Assembled filtration device at previous work.....	26
Figure 2-6 Schematic diagram of separation mechanism	26
Figure 2-7 Focusing of particles in the straight channel.....	29
Figure 2-8 Inertial focusing in rectangular straight channels of different aspect ratios	30
Figure 2-9 Inertial focusing in non-rectangular channel.....	30
Figure 2-10 Schematic diagram for new equilibrium positions in curved channel explained by Di Carlo.....	32
Figure 2-11 Inertial focusing for difference ratio value Δ	33
Figure 2-12 Inertial focusing in serpentine curvilinear channel	35
Figure 2-13 Experimental verification of inertial focusing in spiral channel.....	35
Figure 2-14 Relationship between R_f and focusing tendency.....	36
Figure 2-15 Inertial focusing in spiral channel by Martel	37
Figure 2-16 Non-parabolic velocity profiles and inertial focusing in curved channel	38
Figure 2-17 Velocity profiles in trapezoidal channels.....	39
Figure 2-18 Normalized primary velocity profiles in curved channel in a variety of flow-rate...	39
Figure 2-19 Multiple vortices	40
Figure 2-20 Particle focusing in multiple vortices.....	41
Figure 2-21 Plot of the critical Dean number as a function of the aspect ratio AR	41
Figure 2-22 Experiment and simulation of dye entrapment by vortices in curved channel	42

Figure 2-23 Experiment and simulation by particle entrapment by vortices in curved channel.	43
Figure 2-24 Quasi-inertial focusing in curved channel, vertical shear-induced lift force plays an important role.....	44
Figure 3-1 Microchannel modeled in simulation.....	48
Figure 3-2 Separation efficiency in terms of flow rate for different inlet lengths and particle sizes.....	52
Figure 3-3 Relationship between pressure difference and particle migration	53
Figure 3-4 Simulation results for primary velocity at inlet length.....	53
Figure 3-5 The P value as a function of flow-rate	55
Figure 3-6 Cross section of channel at the beginning of the straight channel	55
Figure 3-7 Graph for separation efficiency in terms of P value	56
Figure 3-8 SEM image of actual cross section of the channel.....	57
Figure 3-9 Separation efficiency graph in terms of position for channels with rectangular and trapezoidal cross sections.....	58
Figure 3-10 Separation efficiency for different injection angles	59
Figure 3-11 Filtration architecture : particle separation based on their size.....	61
Figure 3-12 Mechanism for pseudo-inertial focusing.....	63
Figure 3-13 Separation efficiency in terms of particle size	65
Figure 3-14 Separation efficient in terms of location for different particle sizes.....	66
Figure 3-15 Separation efficiency as a function of normalized pressure defined by Priye for various simulation cases in this study.....	68
Figure 3-16 Separation efficiency as a function of a modified normalized pressure defined by equation [E3-5] for various simulation cases in this study	68
Figure 4-1 Configuration of current microchannel design	71
Figure 4-2 Schematic diagram for circular external tubing and pressure drop calculation	74
Figure 4-3 Schematic diagram for rectangular internal tubing and pressure calculation for different height.....	74

Figure 4-4 Pressure drop in the micro-filtration part, computed by STAR-CCM+	75
Figure 4-5 Simplest circuit model for microchannel design we have	76
Figure 4-6 Improved circuit model for U-type channel.....	78
Figure 4-7 Pressure distribution comparison 1	79
Figure 4-8 Pressure distribution comparison 2	79
Figure 4-9 Pressure distribution at filtration part for current device and system	81
Figure 4-10 Pressure distribution at filtration part for previous device and system.....	82
Figure 4-11 Operation curve for this system in terms of flow-rate	83
Figure 5-1 Channel for experiment by Design 1 Solution, LLC; lengths are given in millimeters	85
Figure 5-2 Configuration of particle separation test.....	90
Figure 5-3 Picture by particle counting machine.....	91
Figure 5-4 Correlation between actual particle size and area on the picture	91
Figure 5-5 Analyzed binary data by <i>ImageJ</i> (left) its counting histogram (upper right) and total number of particles counted on the picture (lower right)	92
Figure 5-6 Particle aggregation on the channel	94
Figure 5-7 Configuration for image processing.....	96
Figure 5-8 Good bonding at entrance (B10).....	98
Figure 5-9 Water test images for C9 (left) and C21(right) channel.....	98
Figure 5-10 Pattern generated by micro-milling on bottom of the lane	100
Figure 5-11 CNC milling comparison	100
Figure 5-12 Classification of bad channel among batch A.....	103
Figure 5-13 Cases solvent bonding is not well established	104
Figure 5-14 Importance of temperature annealing.....	104
Figure 5-15 Major features for channel B1-B14 made by solvent bonding	105
Figure 5-16 Minor features for channel B1-B14 made by solvent bonding.....	106

Figure 5-17 Fluorescence particle images for good prototype channel	109
Figure 5-18 Particle aggregation on the channel	110
Figure 5-19 Fluorescence particle images	110
Figure 5-20 Particle trajectories for 2 μm fluorescent particle.....	112
Figure 5-21 Particle trajectories for 20 μm fluorescent particle.....	112
Figure 5-22 Particle aggregates at filtration part	113
Figure 6-1 Effect of radius of curvature	119
Figure 6-2 Schematic diagram of new device operation	121
Figure 6-3 Symmetric and asymmetric retrieving lines.....	123
Figure 6-4 Graph for pressure distribution for enlarged channel	124
Figure 6-5 Schematic diagram of new design for a separation device employing slanted straight channel	125
Figure 6-6 New device design to take advantage of inertial focusing.....	126
Figure 6-7 Schematic illustration for solvent bonding with groove	127
Figure 6-8 Groove in the channel	128
Figure 6-9 Existence of groove for gasket.....	129
Figure 6-10 Fabrication of multi-level master mold using greyscale photomask	131
Figure 6-11 Multi-level microstructure with slit mask.....	131
Figure 6-12 Separation efficiency and solution transferred ratio	137
Figure 6-13 Graph for the number of stage required for the goal of enrichment ratio	137
Figure 6-14 Diagram of multi-stage enrichment	140
Figure 6-15 Diagram of squeezing solution and the imaging chamber	140

LIST OF TABLES

	Page
Table 1-1 Microfluidic-based cell separation from diluted human blood	2
Table 2-1 Characteristics of cells in the blood.....	45
Table 5-1 Summaries of microchannel fabrication for previous and current one	85
Table 5-2 Information for A batch channel	86
Table 5-3 Information for B batch channel.....	87
Table 5-4 Information for C batch channel.....	88
Table 5-5 Separation efficiency evaluation using experiment and simulations	93
Table 5-6 Repeating water injection tests for A16 channel	95
Table 5-7 Relationship between bonding method and image investigation	105
Table 5-8 Feature summaries for B batch channels.....	107
Table 5-9 Feature summaries for C batch channels.....	108
Table 6-1 Non-dimensional values for spiral channels in the literature	119
Table 6-2 Enlarged microchannel geometry, keeping its microfluidic characteristics.....	122
Table 6-3 Evaluation of the number of layers in the image channel (NL)	136
Table 6-4 Examples of multi stages CTCs enrichment.	138

1. INTRODUCTION

As the biotechnology field is dramatically being developed, the demand for separating and sorting cells has greatly increased. For instance, circulating tumor cells (CTCs), cells that detach from a primary tumor and get into the vascular system, are an emerging topic nowadays and represents the ultimate topic of the research discussed here. Cancer can be diagnosed by detecting circulating tumor cells in the blood of a patient, through what is called a “liquid biopsy”. However, the use of CTCs as a clinical biomarker offers an important technological challenge: CTCs are too sparsely distributed in the blood to be isolated and measured. Thus, techniques to enrich CTCs from whole blood are essential. Because the size of common cells including tumor cells is one or two orders of micrometers, methods for separating micron-sized particles are urgently needed.

There are numerous methods to separate micron-sized particles, with one of the earliest and more common ways to do it being the use of filtration. Particles bigger than the pore size of the filtration membrane are trapped and retained on the membrane, whereas smaller species can pass through it. However, it has a natural disadvantage as it operates as a batch system. First, particles deposited on the membrane need to be separated from it on every batch run, which hinders high throughput operation. Second, it takes a lot of energy. Since the particle solution must pass through the narrow holes, high pressure drop occurs in the system. Thus, lots of energy is required to keep the flow through the membrane. Furthermore, membrane damage and clogging problems resulting from the high pressure required cannot be neglected. Microfluidics is an emerging technology for cell separation. Cells injected into microfluidic devices are subjected to various forces exerted by the fluid flow inside microchannels. The resultant force could make cells migrate to specific

locations and develop inertial focusing behavior, which, if used properly, can enhance cell separation performance and enable high throughput operation up to the ml/min range [1]. Different designs of microchannels (see Table 1-1 for details) have been suggested including straight, spiral [2-5], serpentine [6] and expansion/contraction channels [7-9].

Table 1-1 Microfluidic-based cell separation from diluted human blood

Cells	Shape	Purity	Dilution	Flow-rate per module [ml/min]	Module manifold	Whole blood flow-rate [ml/min]	Ref.
CTC	Weir-like bi-curved	~99	1/5	1	1	0.2	[10]
CTC	Spiral with sheath flow	>85	1/3 with lysis	0.1	3	0.1	[2]
CTC	Expansion/contraction	80	1/20	0.4	1	0.02	[11]
CTC	Expansion/contraction	85	1/40	4.5	1	0.11	[9]
RBC	Spiral, trapezoidal	~100	1/45	1.5	16	0.533	[4]
Plasma	Serpentine	~99.75	1/20	0.35	8	0.140	[6]
Plasma	Spiral	~100	1/20	0.7	1	0.035	[3]
Bacteria	Expansion	~80	1/20	0.2	40	0.400	[7]

Although there are many publications about particle separation with microfluidics, separation efficiency is hardly estimated by means of computational simulations, particularly for curved channels. This could be attributed to undeveloped theories for the behavior of particles in microchannels and huge requirements of computational power, critical challenges for quantifying performance by “computational experiments”. Hence, most computational works have been limited to figure out the position of inertial focusing by single particle circulations [12-15],

and some papers explain their experimental result only based on velocity profiles without particle tracking [5, 16-18]. Thus, if thousand-of-particles simulations are possible, separation efficiency can be estimated by computational methods and the phenomena of particle motion and transport in microchannels could be more clearly elucidated, especially for curvilinear channels.

The main goal of this study is to determine optimum geometric design and operational parameters of a microfluidic device for CTC isolation and enrichment from blood. The basic design of the device to be investigated is the weir-like bi-curvilinear channel suggested by Huang [10]. It is based on weir-filter filtration but it avoids typical disadvantages of microfiltration, such as high pressure drops and batch processing, by employing pressure difference perpendicular to the main flow direction. The advantages of this device will be explained in detail on section 2.3 . In addition, Section 2 covers background information related to particle behavior in microchannels including the characteristics of inertial focusing, which we aim to exploit in our design. Different kinds of geometric and operational factors that affect separation efficiency, employed here as an indicator for best performance, are investigated by conducting 3D simulations of particle and flow transport in Section 3. Also, the mechanism of particle separation in curvilinear microchannels will be elucidated using these computational methods. Particle separation efficiency is estimated both by computational simulations, in Section 3 and experimentally, in Section 5.2. Section 3.6 reveals that pressure distribution is the one of main factor to determine particle separation efficiency. Thus, in section 4, electric circuit analogy model is developed to estimate pressure distribution along the fluid path and problem of current design is investigated. Experiment with microfiltration device produced by Design 1 solution is conducted in Section 5. Distilled water and fluorescent particles is injected into the microchannel and its response is observed by fluorescent microscope. Finally, Section 6 provides discussion on future experimental and

simulation work needed to achieve our goal. The new insights provided by our approach will advance fundamental understanding of inertial focusing in microfluidic systems, and make it possible to design devices tailored toward high-throughput isolation and enrichment of CTCs.

2. BACKGROUND KNOWLEDGE

2.1 Fundamental parameters

2.1.1 Channel Reynolds number

Laminar flow of Newtonian fluids in microchannels can be described using the incompressible Navier-Stokes equation [E2-1]

$$\rho \left(\frac{\partial}{\partial t} + \mathbf{u} \cdot \nabla \right) \mathbf{u} = \nabla p + \mu \nabla^2 \mathbf{u} + \mathbf{f} \quad [\text{E2-1}]$$

Here, ρ is density, \mathbf{u} is velocity of fluid, p is pressure, μ is dynamic viscosity and \mathbf{f} is external forces.

The Reynolds number associated with flow through the microchannel Re_c [E2-2] emerges from non-dimensioned Navier-Stokes equation as a parameter describing the relative contribution of inertial and viscous terms. Taking an average flow velocity U_m and the hydraulic diameter D_h ($D_h = 4A/P$, where A is the cross-sectional area and P is the wetted perimeter) as characteristic velocity and length scales respectively yields

$$\text{Re}_c = \frac{\rho U_m D_h}{\mu} = \frac{U_m D_h}{\nu} \quad [\text{E2-2}]$$

Here, ρ is density, U_m is average of fluid velocity, D_h is hydraulic diameter, μ is dynamic viscosity and ν is kinematic viscosity.

Other length scales (e.g., channel height [19, 20]) have been used in the Reynolds number definition, however D_h is the most commonly used and will be adopted here. Aspect ratio, defined as height of the channel divided by its width is another geometric factor that is important in inertial focusing.

2.1.2 Dean number

In curved channels, secondary Dean flows characterized by counter-rotating vortices perpendicular to the primary flow direction can emerge. The dimensionless Dean number [E2-3], expressing the relative influence of centripetal and inertial forces relative to viscous forces, quantifies the range of conditions that lead to the onset of secondary flows.

$$De = \sqrt{\delta} Re_c = \sqrt{\frac{D_H}{2R_c}} \cdot \frac{U_m D_H}{\nu} = \frac{\sqrt{(centripetal) \cdot (inertial)}}{(viscous)} \quad [E2-3]$$

Here, D_H is hydraulic diameter, R_c is radius of curvature of the channel, δ is curvature ratio ($D_H/2R$), U_m is maximum velocity of the channel, ν is kinematic viscosity and Re_c is channel Reynolds number [21-23]. No secondary flows exist if De is less than unity, a pair of counter-rotating vortices are generated in moderate Dean numbers, unity order of magnitude [Figure 2-12], with additional vortices starting to appear at $De > 25$ [Figure 2-21]. It can also be interpreted as a ratio of geometric average of centripetal forces and inertial forces to viscous forces. Ookawara [24] suggested an empirical relation between the Dean number and the average secondary flow velocity scale $U_{ave, Dean}$ [E2-4]

$$\rho U_{ave, dean} = 1.8 \times 10^{-4} De^{1.63}, \quad De = \frac{UD_H}{\nu} \cdot \sqrt{\frac{D_H}{2R_c}} \quad [E2-4]$$

where U is defined as inlet velocity.

Examples of how Dean flows have been applied in microfluidic systems include Sudarsan [25] who explored applied Dean effects to enhance levels of mixing, Seo [26] and Bhagat [27] who employed spiral microchannels to separate particles by size, and Zhang [28] who introduced a spiral channel with trapezoidal cross-section to generate Dean vortices with variable strength. Simulations by Ha [29] demonstrated the possibility of achieving multiple vortices in curved channels at high flow rates, suggesting a new way to separate particles using the location of the

stagnation point between vortices. Similar kinds of secondary flows have also been generated in straight channels with embedded obstacles for particle separation applications. For instance, contraction-expansion array (CEA) channels can separate particles by their size[9]. 10 μm particles are trapped in vortices on the expansion segment, whereas 2 μm particles keep going following the streamline.

2.2 Forces acting on particles

2.2.1 Particle trajectories

Flows involving micron-sized species (particles, cells) are commonly encountered in microfluidic systems. But the interplay of forces acting on the particles can lead to unusual phenomena called inertial focusing. Trajectories of individual particles can be determined by adopting a Lagrangian viewpoint (moving with the particles) and applying Newton's second law of motion.

$$m_p \frac{d^2 \mathbf{x}}{dt^2} = \sum \mathbf{F}_S + \sum \mathbf{F}_B \quad [\text{E2-5}]$$

Here, m_p is the particle mass, \mathbf{v} is the particle velocity, \mathbf{F}_S is the surface force, and \mathbf{F}_B is the body force. If particles can rotate, conservation of angular momentum is applied as follows

$$I \frac{d\boldsymbol{\omega}}{dt} = \sum \mathbf{T} \quad [\text{E2-6}]$$

where, I is the moment of inertia ($0.1m_p D_p^2$ for a sphere, D_p is diameter of particles), $\boldsymbol{\omega}$ is angular velocity and \mathbf{T} is torque.

The particle body force \mathbf{F}_b can be straightforwardly calculated from their associated fields (e.g., for gravity, $\mathbf{F}_b = m_p \mathbf{g}$). But surface forces are more complicated to describe because they involve interactions between the particles and surrounding fluid, as well as the local pressure and shear stress. Consequently, the Navier-Stokes equations must be solved in order to calculate the

total surface force. This calculation would ideally involve integration over the entire surface of the particle but performing these calculations over an ensemble of hundreds or thousands of particles at each time step in a flow simulation would quickly become overwhelming. Consequently, generalized force models have been developed to simplify these calculations that are either derived analytically or estimated in an empirical manner.

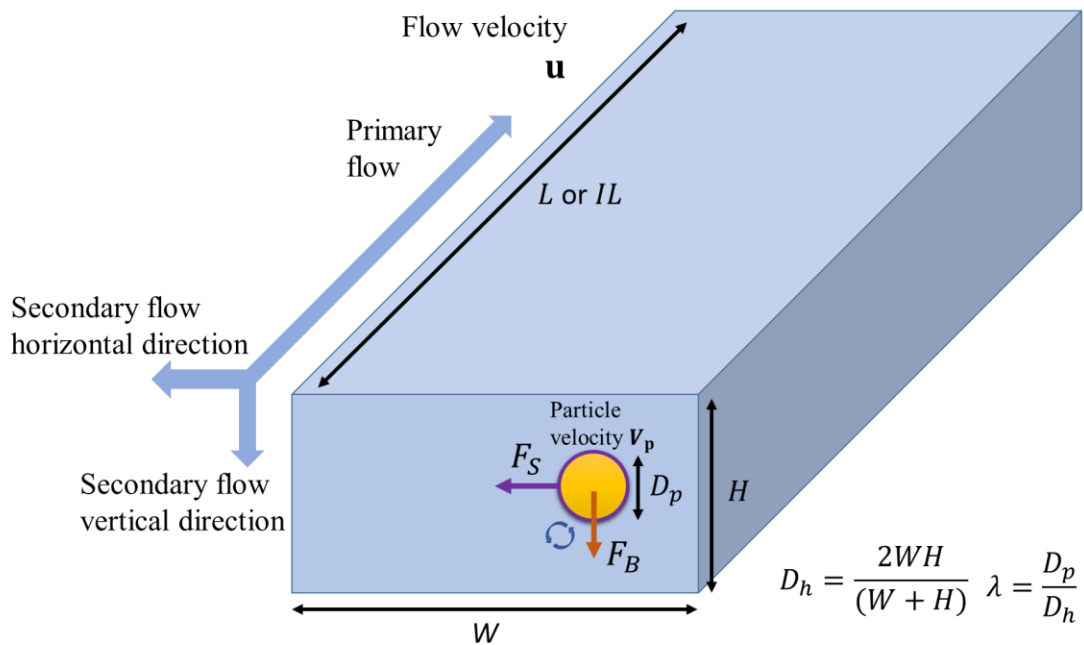


Figure 2-1 Schematic diagram for particles and surrounding flow in microchannel

2.2.2 Fundamental forces: creeping flow regime

Creeping flow, also referred to as Stokes flow, represents a limiting case where $Re_c \ll 1$ and $Re_c/St \ll 1$ such that inertial effects are negligible. Here, St stands for Strouhal number defined as $St = fL/U$, where f is frequency of the observed phenomenon, L is characteristic length and U

is the velocity of the fluid. In the limit as Re_c approaches zero, only the viscous terms in the Navier-Stokes equation are retained, yielding [E2-7] [30]

$$0 = -\tilde{\nabla}\tilde{p} + \tilde{\nabla}^2\tilde{\mathbf{u}} \quad [\text{E2-7}]$$

Tilda means dimensionless variables. Thus, \tilde{p} is defined as $pL/\mu U$, $\tilde{\nabla}$ is $L\nabla$ and $\tilde{\mathbf{u}}$ is \mathbf{u}/U . Here, U and L are characteristic velocity and lengths of the systems.

Since this form of the Navier-Stokes equation is applicable in many microfluidic systems owing to their inherently small length scales and velocities, the creeping flow approximation is a widely used starting point to determine forces on particles.

Stokes [31] considered the motion of a solid sphere in viscous flow using the creeping flow approximation to derive the velocity profile near the particle and integrate the shear stress and pressure over its surface to calculate the force on the particle. This drag force [E2-8], emerging as a consequence of friction between particle and surrounding fluid, is represented as follows

$$\mathbf{F}_d = 3\pi\mu_f D_p \mathbf{U}_s \quad [\text{E2-8}]$$

where \mathbf{U}_s is slip velocity $\mathbf{U}_s = \mathbf{u} - V_p$, \mathbf{u} is the velocity of the continuous phase and V_p is velocity of the particle μ_f is the fluid viscosity, and D_p is the particle diameter. The slip velocity can be interpreted as the relative velocity of flow with respect to particle velocity. This particle-centered viewpoint suggests an alternate definition for the Reynolds number based on the particle size and slip velocity. To avoid confusion with the confined particle Reynolds number that will be mentioned later [E2-16], the Reynolds number here is denoted as freely particle Reynolds number Re_{fp} [E2-9]. Such Reynolds number is employed in circumstances without any obstacles while confined particle Reynolds number is used when the particle is surrounded by the wall.

$$Re_{fp} = \frac{D_p |\mathbf{U}_s|}{\nu} \quad [\text{E2-9}]$$

In this formulation, approximately one-third of the drag force originates from pressure and two-thirds is attributable to shear stress [32]. But all pressure and shear effects are not considered by this formulation because the particle is viewed as moving through an infinite quiescent reservoir of fluid (i.e., pressure becomes zero in the limit as the distance from the particle approaches infinity). Consequently, pressure and shear gradients within the fluid are neglected.

Most microchannel flows of interest are pressure-driven Poiseuille flow, involving a pressure difference between the inlet and outlet of the channel. This gradient in the flow direction gives rise to an additional force because the pressure at the leading and trailing surfaces of the particle is different. This Froude-Krylov force [E2-10] can be calculated by integrating over the surface of the particle and applying Stokes' theorem as follows.

$$\mathbf{F}_p = - \iint_S p \vec{\mathbf{n}} ds = - \frac{m_p}{\rho_p} \nabla p \cdot \nabla p \quad [\text{E2-10}]$$

Here, m_p is the mass of the particle and ρ_p is density of particle. It is the critical term to represent the wall effect when a particle locates near the wall.

Similarly, shear stress gradients exist in Poiseuille flow which are related to velocity gradients near the channel sidewall boundaries. These effects are included as follows [E2-11], where the terms on the right-hand side represent fluid acceleration and buoyancy forces [33].

$$\mathbf{F}_p = \frac{m_p}{\rho_p} (-\nabla p \mathbf{I} + \boldsymbol{\tau}) \cdot (-\nabla p \mathbf{I} + \boldsymbol{\tau}) = m_p \frac{\rho_f}{\rho_p} \left(\frac{D\mathbf{u}_f}{Dt} - \mathbf{g} \right) \quad [\text{E2-11}]$$

With this as a starting point, Basset, Bousinesque, and Oseen [34-36] independently examined the time-dependent force on a sphere in a viscous incompressible fluid. The resulting equation [E2-12] of particle motion is referred to as the BBO equation [33, 37, 38].

$$\begin{aligned}
m_p \frac{d\mathbf{V}}{dt} = & -3\pi\mu D_p \mathbf{V}_{rel} - \frac{m_p}{\rho_p} \cdot \nabla p - \frac{m_f}{2} \frac{d\mathbf{V}_{rel}}{dt} \\
& - \frac{3}{2} D_p^2 \sqrt{\pi\rho_f\mu_f} \int_{-\infty}^t \frac{1}{\sqrt{t-\xi}} \frac{d\mathbf{V}}{dt} \Big|_{t=\xi} d\xi + m_p \Sigma \mathbf{f}_i
\end{aligned} \tag{E2-12}$$

Here, m_p is the mass of the particle, m_f is the displaced-mass (equivalent to $\rho_f \mathcal{V}_p$, \mathcal{V}_p is volume of particle), D_p is the diameter of particle, ρ_p and ρ_f are densities of the particle and fluid, respectively, and μ is the dynamic viscosity. \mathbf{u} and \mathbf{V} are the velocity of fluid and particle, respectively, \mathbf{V}_{rel} is the relative velocity of the particle with respect to the fluid, $\mathbf{V}_{rel} = \mathbf{V} - \mathbf{u}$. The five terms on the right-hand side of the equation represent Stokes drag, pressure gradient forces, inviscid-unsteady (added-mass) forces, viscous-unsteady (Basset history) forces, and the sum of external forces, respectively. The added mass term is important when $\rho_f \gtrsim \rho_p$, as is the case, for example, in spherical air bubbles in water or in ship design.

Tchen [39] proposed extending this framework to consider the motion of a rigid sphere in non-uniform flows, and Maxey and Riley [40] applied the BBO equation to the case of non-uniform creeping flow (the Maxey-Riley equation in [E2-13][41]) where the particles are assumed to be non-rotating rigid spheres and $\text{Re}_{pf} = |\mathbf{V}_{rel}|a\nu^{-1} \ll 1$.

$$\begin{aligned}
m_p \frac{d\mathbf{V}_i}{dt} = & -3\pi D_p \mu \left\{ \mathbf{V}_{rel} - \frac{D_p^2}{24} \nabla^2 \mathbf{u} \right\} + m_f \left(\frac{D\mathbf{u}_i}{Dt} \Big|_{\mathbf{Y}(t)} - \mathbf{f}_{ex,i} \right) \\
& - \frac{1}{2} m_f \frac{d}{dt} \left\{ \mathbf{V}_{rel} - \frac{D_p^2}{40} \nabla^2 \mathbf{u} \right\} \\
& - \frac{3}{2} D_p^2 \rho \sqrt{\pi\nu} \int_{-\infty}^t \frac{d}{d\tau} \left\{ \mathbf{V}_{rel} - \frac{D_p^2}{24} \nabla^2 \mathbf{u} \right\} \frac{d\tau}{\sqrt{(t-\tau)}} + m_p \mathbf{f}_{ex,i}
\end{aligned} \tag{E2-13}$$

Here, $\mathbf{V}_{rel} = \mathbf{V}_i(t) - \mathbf{u}_i[\mathbf{Y}(t), t]$. Note that even though the creeping flow approximation is applied, non-uniform velocity fields do contribute to the surface forces. It is also important to note that this formulation is based on the undisturbed velocity profile at the center of the particle, not at the surface. The terms with Laplacian symbols are corrections introduced to account for velocity

disturbances caused by the presence of the particle, and are called Faxen terms [42]. Although the above formulations expressing particle motion are widely used, they often do not make accurate predictions because of limitations associated with the assumption of creeping flow ($Re \ll 1$). They therefore are not the best tools to analyze particle motion in microfluidic systems.

2.2.3 Beyond creeping flow: lift forces

In 1961, Segré and Silberberg [43-45] reported the unexpected observation that macroscopic spherical particles in dilute suspension under laminar flow through a straight circular pipe assembled or “focused” into a thin annular region at a fixed distance (60% of the pipe radius) from the centerline of the pipe. They observed that this focusing effect became prominent as the channel Reynolds number increased from 2 to 700. There was no way to explain this phenomenon using conventional creeping flow analysis in which the force exerted on a spherical particle is collinear with the flow direction, with no other lift forces. The authors therefore reasoned that inertial effects neglected in creeping flow formulations must play a critical role in governing the observed focusing.

Saffman [46-48] firstly derived an analytical expression for lift forces in simple shear flow by matched asymptotic expansion. This formulation captured the lift force particles experience under small but finite fluid inertia, thereby enabling them to migrate and cross streamlines. This calculation yields the Saffman lift force [E2-14] as follows.

$$\begin{aligned} \mathbf{F}_{LS} &= 6.46R_p\mu Re_G^{0.5} \mathbf{U}_s = 6.46R_p\mu (GR_p^2/\nu)^{0.5} \mathbf{U}_s = 6.46R_p^2\mu\nu^{-0.5} \mathbf{G}^{0.5} \mathbf{U}_s \\ &= 6.46R_p^2\mu\nu^{-0.5} (u - V_p) \text{sign} \left(\frac{d\mathbf{u}}{dy} \right) \left| \frac{d\mathbf{u}}{dy} \right|^{0.5} \end{aligned} \quad [\text{E2-14}]$$

where, R_p is the particle radius, μ is the dynamic viscosity, ν is the kinematic viscosity, G is the magnitude of the velocity gradient, and \mathbf{U}_s is slip velocity, defined as $\mathbf{U}_s = u - V_p$, u is

the instantaneous velocity of the continuous phase and V_p is velocity of the particle. Note that the slip velocity U_s and particle velocity relative to flow V_{rel} have the same magnitude but opposite direction.

The “*driving force*” of Saffman’s formulation is the velocity difference between fluid and particle, the same as in the drag force. Direction of this lift force is determined by the direction of the velocity difference between particle and fluid. When the particle velocity is faster than fluid velocity, referred to as lead case, particles get forces toward the wall. On the other hand, when the particle velocity is slower than fluid velocity, referred to as lag case, this force points to the center of the channel. Notice that Saffman lift force is considered as a shear-induced lift force because its force equation has a shear rate term in it.

But nowadays’ knowledge indicates that the shear-induced lift force is always pointing toward the wall, implying inconsistencies with Saffman lift force. This happens because of Saffman’s assumption of simple shear flow, which has a linear velocity profile, and because effects of the sidewall boundaries are not considered. However, flow in microchannels is typically Poiseuille flow with a parabolic velocity profile and, due to the gradient of shear, the lift force is always pointing toward the wall as seen in Figure 2-2. Notice also that most of the times the velocities of the particle and undisturbed fluid at the center of the particle are identical, yielding zero Saffman lift force. But this doesn’t mean that shear-induced lift force doesn’t exist under such circumstances. If particle size is large enough compared to channel height, each upper and lower hemisphere gets forces of opposing direction. The upper hemisphere (see the inset of [Figure 2-2]) has lag condition where the lift force points to the center of the channel, while the lower hemisphere is subjected to lead condition where the lift force is toward the wall. Because of parabolic velocity profiles, lead condition is always stronger than lag condition, resulting in a force

constantly directed toward the wall. This effect is referred to as shear-gradient-induced lift force and it is considered as one of the dominant shear-induced lift forces.

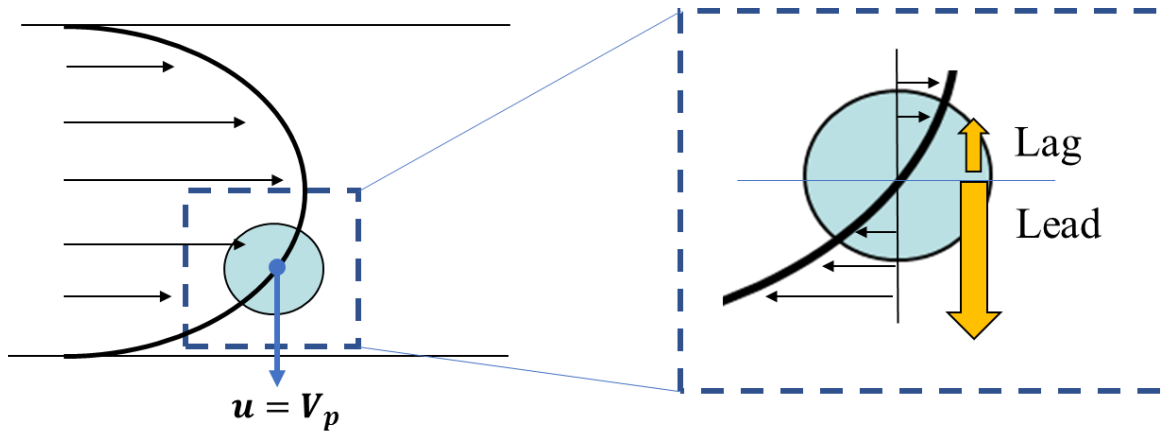


Figure 2-2 Schematic diagram for shear-gradient-induced lift force

It is known that shear-gradient-induced lift force is much larger than Saffman lift force. According to the studies by Ho and Leal [49] (also summarized in the review paper by Martel [50]), shear-gradient-induced lift force is a single order of magnitude greater than the Saffman lift force described above, and three orders of magnitude greater than a rotation-induced lift force. Though its existence is obvious, a quantitative force equation for shear-induced lift is still debatable and ambiguous. It is attributed to the fact that shear-induced force is only observed in small channels where shear rate is extremely large. Large-scale pipes have turbulent condition and flat-like velocity profiles where zero shear rate is observed. Although it is experimentally challenging to directly study shear-induced lift forces in microchannels, there are several related studies in the literature.

Wall-induced lift force is the other important lift force that should be considered. It occurs only when the particle locates near the wall. The proximity of wall and particles induces high pressure between them, generating a net force away from the wall [Figure 2-3].

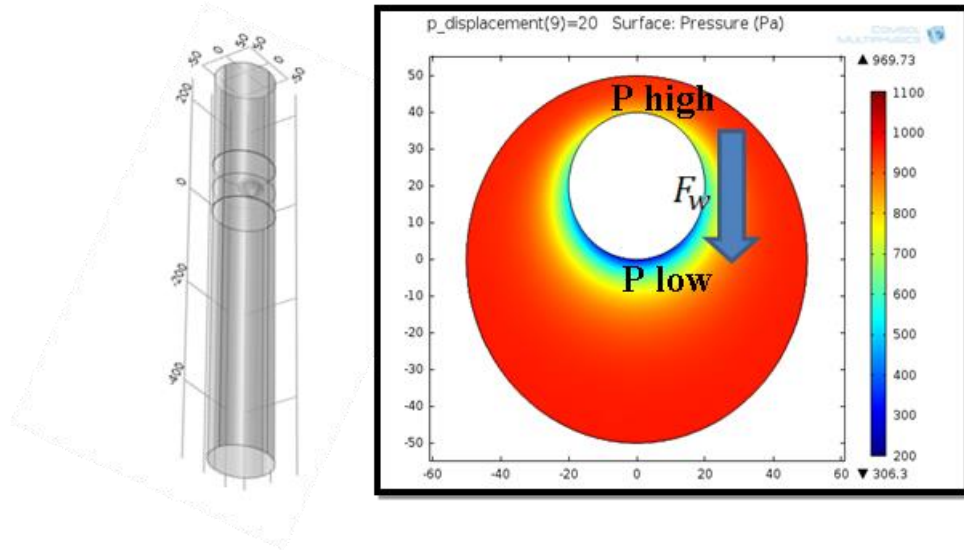


Figure 2-3 Pressure contour in the proximity of wall and particles

Fluid between particle and wall has higher pressure than others do, generating forces towards the center of the cross section. Fluid simulation is conducted by COMSOL.

It is known that shear-gradient-induced lift force is much larger than Saffman lift force. According to the studies by Ho and Leal [49] (also summarized in the review paper by Martel [50]), shear-gradient-induced lift force is a single order of magnitude greater than the Saffman lift force described above, and three orders of magnitude greater than a rotation-induced lift force. Though its existence is obvious, a quantitative force equation for shear-induced lift is still debatable and ambiguous. It is attributed to the fact that shear-induced force is only observed in small channels where shear rate is extremely large. Large-scale pipes have turbulent condition and flat-like velocity profiles where zero shear rate is observed. Although it is experimentally

challenging to directly study shear-induced lift forces in microchannels, there are several related studies in the literature.

Wall-induced lift force is the other important lift force that should be considered. It occurs only when the particle locates near the wall. The proximity of wall and particles induces high pressure between them, generating a net force away from the wall [Figure 2-3].

There are several studies for generalized lift force in microchannels. Ho & Leal [49] derived an equation for the particle lift force in a parabolic Poiseuille velocity profile. It is obtained by transforming the Navier-Stokes and continuity equations in terms of disturbance variables. Schonberg and Hinch [51], and later Hogg [52] developed it to a broader Reynolds number range. Asmolov [53] and Di Carlo [54] suggested new equations too. During their derivations new variables were employed, since the hydraulic diameter of the channel (or representative distance between bounding surfaces, such as the narrow gap between parallel surfaces in a rectangular channel cross section) and the particle diameter can both serve as characteristic length scales, the confinement ratio λ [E2-15] can be defined to obtain a single quantity embedding both the particle and channel length scales [55]. Using this parameter, the transformed Navier-Stokes equation brings out a new dimensionless variable, the particle Reynolds number [E2-16] defined as follows

$$\lambda = D_H/l \quad [\text{E2-15}]$$

$$\text{Re}_p = \text{Re}_c \lambda^2 = \frac{U_m D_p^2}{\nu l} \quad [\text{E2-16}]$$

Here, D_p is the particle diameter, U_m is the undisturbed fluid velocity at the channel centerline (or maximum velocity of the flow), ν is the kinematic viscosity, and l is the characteristic length of the channel, defined as hydraulic diameter, $(4A/P)$ in this study. These two parameters, λ and Re_p , are really critical for determining inertial focusing as discussed later in this section. However, some authors suggest that the narrow gap between parallel surfaces should be

chosen for l because the steeper shear gradient in this direction generates a stronger shear-induced lift force. For example, if the aspect ratio of a rectangular channel's height to width is 2 ($AR = 2$), the lift force a particle experiences across the channel width is four times greater than that along the channel height [8].

Ho and Leal [49] derived a lift force equation comprised of wall-induced lift force and shear-induced lift force [E2-17].

$$\mathbf{F}_L = \lambda^2 \text{Re}[\boldsymbol{\beta}^2 G_1(\mathbf{s}) + \boldsymbol{\beta} \boldsymbol{\gamma} G_2(\mathbf{s})] \quad [\text{E2-17}]$$

where λ is confinement ratio defined by the ratio of particle diameter and pipe hydraulic diameter, $\boldsymbol{\beta}$ is the local shear rate, $\boldsymbol{\gamma}$ is the shear rate gradient, s is the normalized radial location of the particle ranging from 0 to 1, and G_1 and G_2 are the position-dependent integration constants for a first order Bessel function [17].

Asmolov [53] determined the net lift force acting on a particle translating parallel to the walls within a channel for large channel Reynolds number. Matched asymptotic expansion methods were employed to solve the Oseen-like equations governing the disturbance flow, yielding the following expression [E2-18].

$$\mathbf{F}_L = \frac{4C_L \rho D_p^4}{D_h^2} \mathbf{U}_f^2 \quad [\text{E2-18}]$$

They concluded that wall lift effects should be taken into account at distances of the order of $\ell \text{Re}_c^{-1/2}$ from the wall (i.e., this equation is not valid very close to the wall). ℓ is characteristic length of channel. Di Carlo [54] further developed this analysis by employing numerical simulations to estimate the relative contributions of the shear gradient lift and wall induced lift forces in each region. This analysis yielded the following two equations [E2-19] and [E2-20] involving the confinement ratio λ .

$$\mathbf{F}_{SG} = \frac{C_{SG}\rho D_p^3}{D_h} \mathbf{U}_f^2 = C_{SG}\rho D_p^2 \mathbf{U}_f^2 \lambda \quad [\text{E2-19}]$$

$$\mathbf{F}_{WI} = \frac{C_{WI}\rho D_p^6}{D_h^4} \mathbf{U}_f^2 = C_{WI}\rho D_p^2 \mathbf{U}_f^2 \lambda^4 \quad [\text{E2-20}]$$

Liu [14, 56] employed direct numerical simulations in which both particles and water molecules are considered as a particle to figure out the best parameters for combining all forces mentioned above.

Particle rotation also generates a lift force, as described by Rubinow and Keller [57] who considered the lift force about a spinning sphere moving in a viscous fluid at low channel Reynolds number as follows.

$$F_{LR} = (\pi D_p^3/8) \rho \boldsymbol{\Omega} \times \mathbf{U}_s \quad [\text{E2-21}]$$

where, D_p is diameter of particle, ρ is fluid density, \mathbf{U}_s is slip velocity and $\boldsymbol{\Omega}$ is relative rotation given by $\boldsymbol{\Omega} = 0.5\nabla \times \mathbf{u}_f - \boldsymbol{\omega}_p$. A slip-rotation lift force [E2-22] emerges at higher particle Reynolds number, and is described by introducing a lift coefficient, C_{LR} [33]. Equation [E2-23] was obtained by Rubinow and Keller, and later refined by Oesterle and Bui Dinh in Equation [E2-22] based on available literature and experiments for $Re_p < 140$.

$$\mathbf{F}_{LR} = C_{LR} \frac{\pi}{8} \rho_f D_p^2 |\mathbf{U}_s| \frac{\boldsymbol{\Omega} \times \mathbf{U}_s}{|\boldsymbol{\Omega}|} \quad [\text{E2-22}]$$

$$C_{LR} = D_p |\boldsymbol{\Omega}| / U_s = Re_R / Re_p \quad [\text{E2-23}]$$

$$C_{LR} = 0.45 + \left(\frac{Re_R}{Re_{fp}} - 0.45 \right) \exp(-0.05684 Re_R^{0.4} Re_{fp}^{0.3}) \quad [\text{E2-24}]$$

Here, ρ_f is fluid density, D_p is diameter of particle, U_s is slip velocity defined as $U_s = u_f - V_p$ and $\boldsymbol{\Omega}$ is relative rotation given by $\boldsymbol{\Omega} = 0.5\nabla \times \mathbf{u}_f - \boldsymbol{\omega}_p$. $Re_{fp} = D_p U_s \nu^{-1}$ and $Re_R = D_p^2 |\boldsymbol{\Omega}| \nu^{-1}$. This rotationally generated lift force, also called the Magnus effect, can explain

physical phenomena such as the curving of a pitched baseball and the long range of a spinning gold ball.

In summary, the lift force can be divided into contributions associated with (1) shear lift, (2) shear gradient lift, (3) wall lift, and (4) rotation-induced lift. Shear gradient lift and wall lift forces are the most significant contributions, and therefore play the most important role in microfluidic inertial focusing. We also note that lift forces are not observed in macro-scale pipes because gravity forces cannot be neglected and the flow in large pipes is usually turbulent.

2.2.4 Body force

Unlike surface forces, body forces act on the entire volume of an object. They can originate from physical fields (e.g., gravity, electromagnetic), inertial spin, and centrifugal or Coriolis effects. Body forces are typically neglected in microfluidic systems, with the combined effects of gravity[E2-25], centrifugal forces[E2-27], buoyancy [E2-26][E2-28] and added mass [E2-29] being 2 to 3 orders of magnitude smaller than drag and lift forces [18]. Here, \forall is the particle volume.

Body forces can, however, be important in special circumstances such as electrophoresis (electromagnetic force) and centrifugation (centrifugal force). Buoyancy forces associated with gravity and centrifugal effects on a spherical object, can be determined by integrating pressure over the surface of the sphere [58]

$$\mathbf{F}_g = \forall \rho_p \mathbf{g} \quad [\text{E2-25}]$$

$$\mathbf{F}_{g,b} = -\forall \rho_f \mathbf{g} \quad [\text{E2-26}]$$

$$\mathbf{F}_c = m R_0 \boldsymbol{\omega}^2 = \forall \rho_p R_0 \boldsymbol{\omega}^2 \quad [\text{E2-27}]$$

$$\mathbf{F}_{c,b} = -\forall \rho_f R_0 \boldsymbol{\omega}^2 \quad [\text{E2-28}]$$

$$\mathbf{F}_a = \frac{\rho_f \nabla}{2} \left(\frac{D\mathbf{u}}{Dt} - \frac{d\mathbf{V}}{dt} \right) \quad [\text{E2-29}]$$

2.2.5 Other forces

2.2.5.1 Particle shape

Hur [43] suggested that a particle's rotating diameter, a longest diagonal when particles rotates, rather than cross-sectional size, determines its equilibrium position. Particles with a longer rotating radius will focus closer to the center of the channel and preferentially assume a horizontal orientation.

2.2.5.2 Deformability

In another paper, Hur [44] argued that deformable particles experience an additional lift force near the center of a channel compared to rigid particles, potentially enabling deformability to be used as label-free biomarker. A distinguishing feature from other lift forces is that deformability effects are not purely inertial and can therefore exist in creeping flow conditions where inertial effect are neglected. These effects may be important for cell-based studies, as red blood cells, for example, have a disk-like shape and are deformable.

2.2.5.3 Elastic forces from the surrounding medium

These effects are generally neglected because water, the most commonly used solvent in microfluidic systems, is Newtonian. If the solvent has viscoelastic properties and the shear rates are high, elastic forces may exert a non-negligible effect on inertial focusing [59-62]. Whole blood is a non-Newtonian fluid, and therefore may display viscoelastic behavior that impacts inertial focusing under certain conditions.

2.2.6 Forces considered in our computational model.

2.2.6.1 Basic equations

We perform computational fluid dynamics simulations to track particle trajectories in microchannels using STAR-CCM+ V.11.04.010. This software package provides built-in functions to capture the drag force \mathbf{F}_d [E2-30], pressure gradient force \mathbf{F}_p [E2-31], added mass force \mathbf{F}_{am} [E2-32] and gravity body force \mathbf{F}_g [E2-33].

Based upon the characteristics of our system and for computational efficiency, only the drag and pressure gradient forces are employed [18]. The Schiller-Naumann correlation is applied to drag force. It is kinds of empirical correction for broaden range of Freely particle Reynolds number.

$$\mathbf{F}_d = \frac{1}{2} C_d \rho_f A_p |\mathbf{U}_s| \mathbf{U}_s \quad [\text{E2-30}]$$
$$C_d = \frac{24}{\text{Re}_{fp}} (1 + 0.15 \text{Re}_{fp}^{0.687}) \text{ at } \text{Re}_{fp} \leq 10^3$$

$$\mathbf{F}_p = -\frac{\pi}{6} D_p^3 \nabla p_{static} \quad [\text{E2-31}]$$

$$\mathbf{F}_{am} = \frac{\pi}{12} \rho D_p^3 \left(\frac{D\mathbf{u}}{Dt} - \frac{d\mathbf{V}}{dt} \right) \quad [\text{E2-32}]$$

$$\mathbf{F}_g = m_p \mathbf{g} \quad [\text{E2-33}]$$

Here, A_p is the projected frontal area of the particle ($\pi D_p^2/4$ for a sphere), Re_{fp} is the free particle Reynolds number ($R_p |U_s| \nu^{-1}$), ρ_f is the fluid density, U_s is the slip velocity ($U_s = u - V$, where u and V are the velocity of fluid and particle, respectively), and D_p is the diameter of the particle.

2.2.6.2 Lift forces and two-way coupling

Additional forces become important in the non-creeping region where lift forces exist. The shear lift force F_{LS} [E2-34] and spin lift force F_{LR} [E2-35] are included as built-in functions.

STAR-CCM+ employs empirical equations by Sommerfeld to cover a broader range of Reynolds numbers than the theoretical formulations introduced.

$$\mathbf{F}_{LS} = C_{LS} \frac{\rho\pi}{8} D_p^3 (\mathbf{u}_s \times \boldsymbol{\omega}), \quad C_{LS} = \frac{4.1126}{\text{Re}_s^{0.5}} \quad [\text{E2-34}]$$

$$F_{LR} = \frac{\rho\pi}{8} D_p^2 C_{LR} |\mathbf{U}_s| \frac{|\boldsymbol{\Omega} \times \mathbf{U}_s|}{|\boldsymbol{\Omega}|}, \quad C_{LR} = 0.45 + \left(\frac{\text{Re}_R}{\text{Re}_{fp}} - 0.45 \right) e^{-0.5684 \text{Re}_R^{0.4} \text{Re}_{fp}^{0.3}} \quad [\text{E2-35}]$$

Here, $\text{Re}_{fp} = \frac{D_p |\mathbf{U}_s|}{\nu}$, $\text{Re}_R = \frac{D_p^2 |\boldsymbol{\Omega}|}{\nu}$, $\text{Re}_S = \frac{\rho D_p^2 |\boldsymbol{\omega}|}{\mu}$, D_p is the particle diameter, ρ is the fluid density. μ is the dynamic viscosity, ν is the kinematic viscosity, \mathbf{U}_s is the fluid velocity relative to the moving particle, known as slip velocity $\mathbf{U}_s = \mathbf{u}_f - \mathbf{V}_p$, $\boldsymbol{\omega} = \nabla \times \mathbf{u}$ is curl of the fluid velocity and $\boldsymbol{\Omega} = \frac{1}{2} \nabla \times \mathbf{u} - \boldsymbol{\omega}_p$, $\boldsymbol{\omega}_p$ is the angular velocity of the particle.

These equations alone, however, are not sufficient to predict inertial focusing because there is no expression for the wall induced lift force that opposes shear lift. We address this by applying two-way coupling to generate a comparable force to counteract shear-induced lift force. Since the proximity of wall and particles induces high pressure between them, generating a net force away from the wall, two-way coupling allows this extra force to be determined by calculating pressure gradient force around particles at each time step.

We also note that the above empirical equations do not consider shear-gradient-induced lift force, which might be significantly larger than Saffman lift force. However, although shear-gradient-induced lift force is not considered in this simulation, we point out that operation conditions we investigated are in the Dean drag force dominant region and avoid the region of complete inertial focusing where shear-gradient-induced lift force might be important. Also, separation efficiency would not be affected by whether Saffman lift force or shear-gradient-induced lift force is considered in a region of quasi-inertial focusing. The reason for this is that separation efficiency in our design, which will be described later, is related to how many times

particles face with a narrow bridge and cross it in a curved segment. If a particle is forced to be away from the narrow bridge in anyway, separation efficiency would be limited. Both Saffman lift force and shear-gradient-induced lift force are expected to prevent particles from getting close to the narrow bridge, resulting in no difference between them in terms of separation efficiency. The weaker Saffman lift force might take more time and length to complete the vertical migration of particles where secondary flow direction is switched back than the stronger shear-gradient-induced lift force does, but the final effect is expected to be the same. If necessary, an expression for shear-gradient-induced lift force can be considered through a user-defined function.

2.2.6.3 Contacting forces and DEM mode

When a particle contacts another particle or a wall boundary, it experiences a repulsive force directed away from the object. Discrete element methods (DEM) are employed to capture these effects, which may become significant in narrow sized zones of the proposed microchannel filters. Simple rebound models only track the center of the particle, yielding unrealistic results such as the ability of large particles to pass through narrow spaces smaller than the particle size. DEM overcomes this limitation by considering the particle size, preventing particles from passing through narrow spaces.

2.2.6.4 Final Differential Equations

The conservation of momentum for the particles comprises a summation of all forces. Particle trajectories can therefore be calculated by solving the equation below.

$$m_p \frac{dV}{dt} = \mathbf{F}_S + \mathbf{F}_B + \mathbf{F}_c = \left(\mathbf{F}_d + \mathbf{F}_p + \sum \mathbf{F}_L \right) + \mathbf{F}_B + \mathbf{F}_c \quad [\text{E2-36}]$$

Here, \mathbf{F}_S is surface force, \mathbf{F}_B is body force, \mathbf{F}_C is contact force, \mathbf{F}_d is drag force, \mathbf{F}_P pressure gradient force and \mathbf{F}_L is lift forces

Vorticity is employed to determine the conservation of angular momentum for a particle.

The drag torque is expressed as follows.

$$\mathbf{T} = C_R \frac{\rho}{2} \left(\frac{D_p}{2} \right)^5 |\boldsymbol{\Omega}| \boldsymbol{\Omega}, \quad C_R = \frac{64\pi}{\text{Re}_R} \text{ at } \text{Re}_R < 32 \quad [\text{E2-37}]$$

From which the conservation equation for angular momentum becomes

$$I \frac{d\boldsymbol{\omega}}{dt} = \mathbf{T} \quad [\text{E2-38}]$$

where, I is the particle's moment of inertia ($0.1m_p D_p^2$ for a sphere).

2.3 Microfiltration

One of the conventional ways to separate particles/cells from solution is using a physical filter. Among a variety of physical filters that can be employed, membranes are the most popular filter utilized [63][Figure 2-4 left]. Particles larger size than pore size of the membrane is trapped and retained on the membrane, whereas smaller species can pass through it. Weir-type filtration has also been reported in the literature, working in similar way [64][Figure 2-4 Filtration methods middle]. The bridge height (between ceiling and dam) selects particles based on their size. These filtration architectures have the advantage of high separation efficiency, as definitely large particles/cells are not able to pass through the smaller sized holes/gaps. However, they have many disadvantages. First, they yield low throughput. Because they operate as a batch system, deposited particles/cells should be collected in every run. Without it, fouling layer hinders migration of the particles and solution, resulting in lower throughput. Also, high pressure drop occurs due to small size pore/gap, thus requiring high energy consumption in the separation process. Furthermore, it

might damage fragile membranes or gaps, which would be a critical problem for separation if it happens. Clogging problems also cannot be ignored.

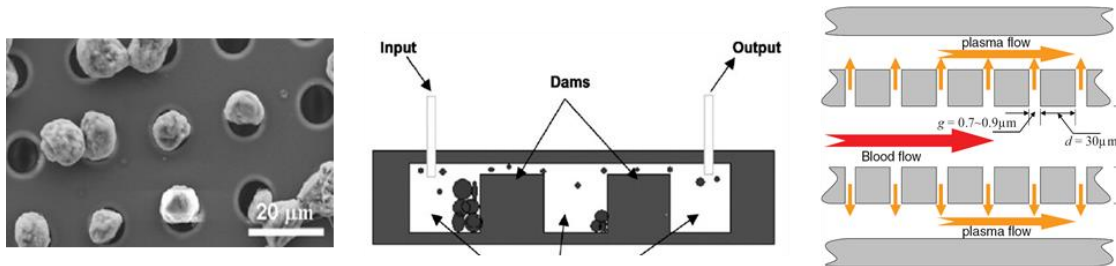


Figure 2-4 Filtration methods

Reprinted from Ref.[63] Zheng, Ref.[64] Chen and Ref.[65] Kang with permission, respectively. Membrane filtration (left), weir-filtration (middle) and cross flow filtration (right).

To avoid this problem, one of proposed solution is filtration architectures with cross flow configuration [65][Figure 2-4 right]. In this approach, secondary flow is generated in the channel and employed as driving force of filtration. Direction of main flow direction and direction of filtration is perpendicular to each other, reducing pressure drop. In addition, because continuous separation can be implemented in cross flow filtration, throughput could be improved. Clogging problems could be avoided, too. Large particles have bigger inertia than small particles, so large particles are less affected by secondary force and have a lower chance to face with the filter. Also, solvent is transferred from the lane to the secondary one(s), so the former lane is automatically enriched. It would be a good method to separate and enrich circulating tumor cells. Previous study[10] in this group noticed that strong secondary flow is generated where two different height rectangular lanes are connected each other through narrow gap. The separation device to be investigated in this study is a kind of cross flow filtrating device employing a narrow gap and

pressure difference induced by height difference. Curved segment where Dean vortices is generated is also added at the configuration to achieve higher separation [Figure 2-5][Figure 2-6].

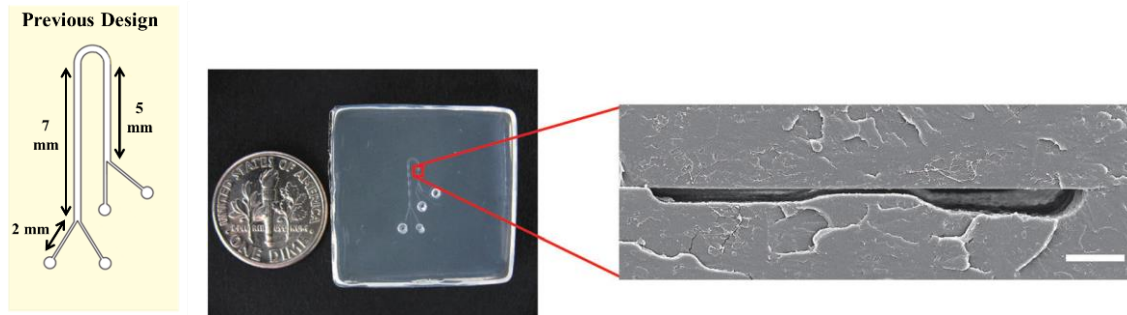


Figure 2-5 Assembled filtration device at previous work

Reprinted from Ref.[10] Huang with permission. Left, length of each part in the microchannel. It has supplying line of 2 mm, inlet of 7 mm and outlet of 5 mm. Middle, top-view photograph of the previous filtration device made of poly lactic acid and enzyme proteinase K. Right, SEM images of cross section of the microchannel at filtration part. White bar is 50 μm .

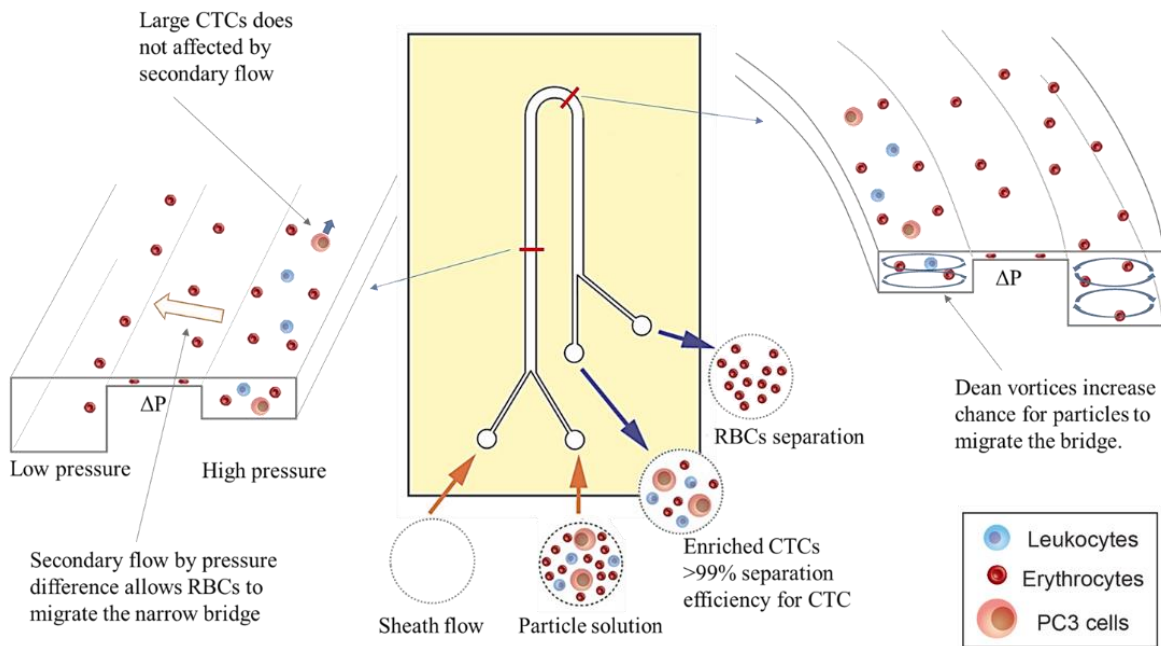


Figure 2-6 Schematic diagram of separation mechanism

Reprinted from Ref.[10] Huang with permission.

2.4 Inertial focusing

2.4.1 Dominant forces in scale of micro-channels

Inertial focusing occurs as a consequence of a balance among forces (e.g., lift, drag, body forces) acting along the secondary direction perpendicular to the main flow. In a straight channel, spherical particles become focused based on the balance between shear gradient and wall lift forces. Zhou and Papautsky [66] explain inertial focusing based on a two-step process consisting of fast migration dominated by shear gradient and wall lift forces, followed by a slower process dominated by rotational lift forces [Figure 2-7 (d)]. Cherukat and McLaughlin [67] argued that rotation becomes important where shear is large and parabolic velocity profiles in the microchannels satisfy large shear near wall. Chun and Ladd [68] conducted time-dependent experiments and simulations using the lattice-Boltzmann method, demonstrating that randomly distributed particles migrate close to the walls but do not stick there due to the wall lift force, after which they form chains and ultimately become focused at equilibrium positions. Clime's computational simulation [69] employs secondary velocity profiles in the channel and lift velocity, representing similar process, too.

The position where a particle is focused is depends on the channel's cross-sectional shape. In circular tubing, the net force on the particles becomes zero at a distance 0.6 of the channel radius, resulting in the formation of a thin annular ring. However, multiple equilibrium positions are generated in channels with square or rectangular cross-sections. These focusing locations can consist of 4 nodes at the center of each side of a square channel, or 2 nodes at the center of the longer edge in a rectangular channel [Figure 2-7]. In the case that the rectangular channel has extreme aspect ratio (AR) is, weak lines are generated along the longer side of the channel [Figure 2-8]. It seems that the expected second focusing step is not well conducted due to flat-like velocity

profiles in extreme AR channels [6]. Kim [13] explored inertial focusing in non-rectangular cross-section microchannel by both experiment and simulation, where forces were evaluated by integration over the particle surface [Figure 2-9]. A channel with a half-circle cross-section profile displays two focusing points with more particles concentrated along the curved side. A channel with a wide isosceles triangle cross-section displays three focusing points, with two of them biased toward largest interior angle. Conversely, narrow isosceles or equilateral triangle cross-sections display inertial focusing near the centerline.

The non-dimensional parameters λ and Re_p provide a basis to identify conditions favorable for inertial focusing. Experimental results by Bhagat [8] indicate that inertial focusing in rectangular channels is observed when, $\lambda = D_p/l \geq 0.07$ and $Re_p > 0.05$. D_p is particle diameter and l is characteristic lengths of the channel: Either hydraulic diameter or length of the side of a cross-section. If curvature or Dean flow effects are included (explained in detail in the next section), the non-dimensional parameters Re_c , Re_p , R_f and De identify the inertial focusing regime. For example, a survey of 59 different studies identified values of $Re_c = 112 \pm 76.5$, $Re_p = 3.59 \pm 7.86$, and $De = 24.11 \pm 26.8$ associated with the inertial focusing regime [70].

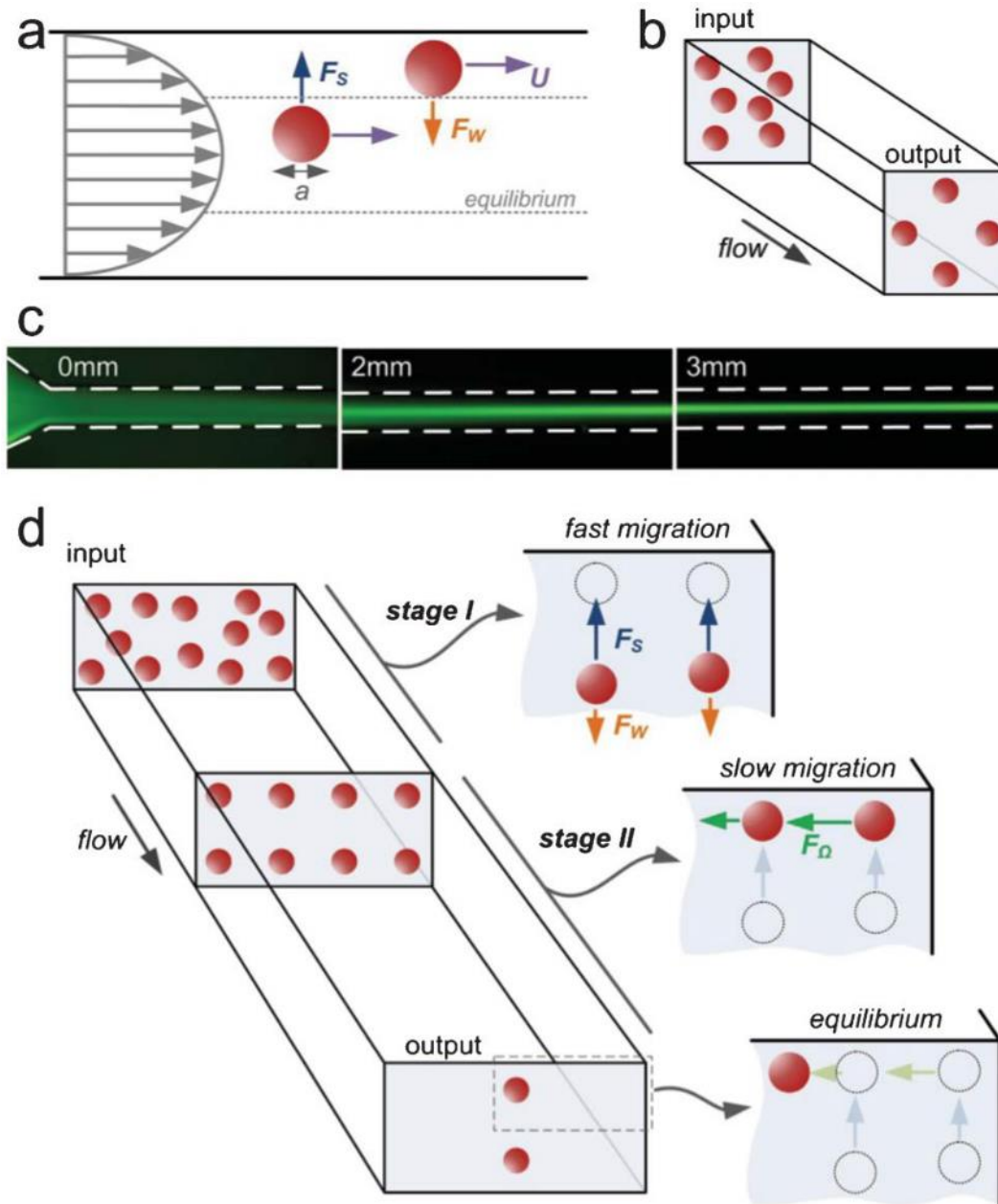


Figure 2-7 Focusing of particles in the straight channel

Reprinted from Ref. [66] Zhou with permission. (a) A particle is balanced and focused by shear-induced lift force and wall-induced lift force. (b) Inertial focusing at square channel. (c) Fluorescent images of 20 μm particles in a cross section 100 μm wide and 27 μm tall at $\text{Re} = 30$. (d) Schematic diagram for two-step inertial focusing in high aspect ratio channel.

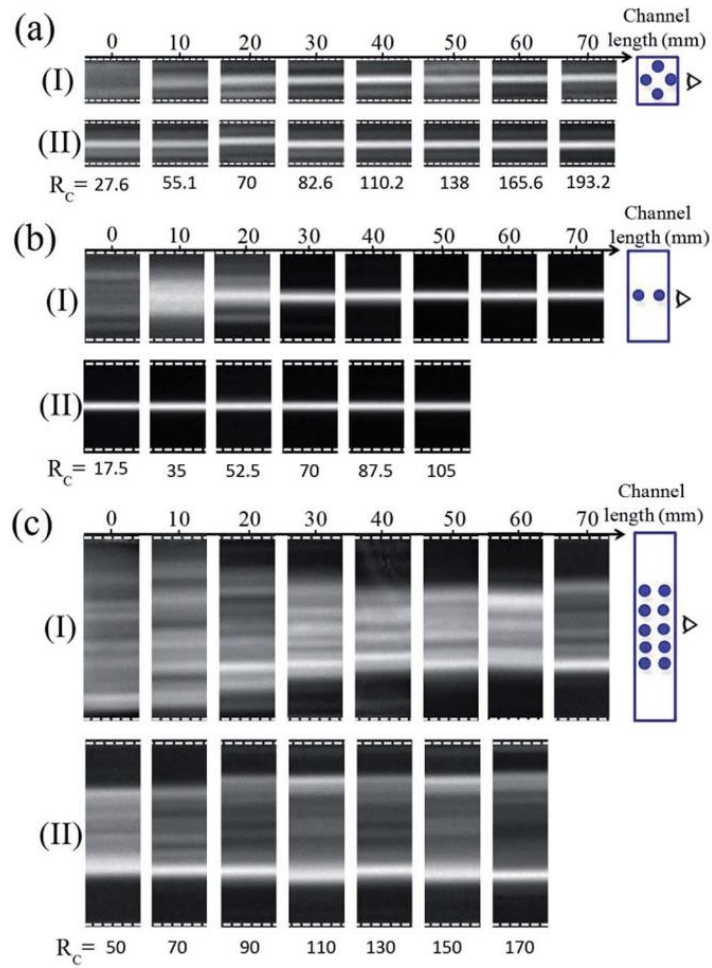


Figure 2-8 Inertial focusing in rectangular straight channels of different aspect ratios

Reprinted from Ref. [6] Zhang with permission. (a) $50 \mu\text{m} \times 42 \mu\text{m}$, (b) $100 \mu\text{m} \times 42 \mu\text{m}$ and (c) $200 \mu\text{m} \times 42 \mu\text{m}$. (I) Shows inertial focusing at Re_c 7 in terms of locations. (II) Demonstrates inertial focusing as a function of Reynolds number. No inertial focusing at (c) might be due to flat-like velocity profiles.

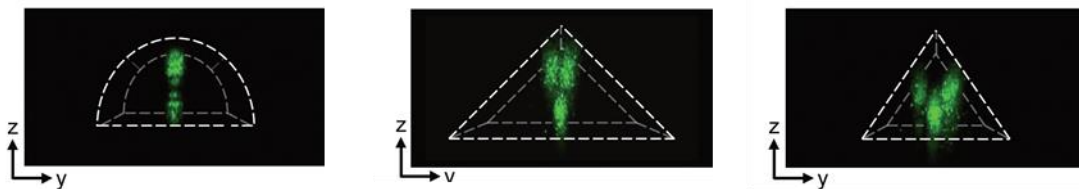


Figure 2-9 Inertial focusing in non-rectangular channel

Reprinted from Ref. [13] Kim.

2.4.2 The impact of Dean vortices on inertial focusing

Dean vortices generated in curved channels also act perpendicular to the primary flow, parallel to other lift forces. Consequently, secondary drag forces generated by the secondary Dean flow combine with other lift forces to govern inertial focusing in curved channels [18, 71]. The dominant forces for inertial focusing are the drag force from the secondary flow and the lift force from the primary flow, yielding the two following contributions whose balance determines the equilibrium focusing locations: (1) shear gradient lift force and (2) drag force by secondary flow induced by either Dean vortices or pressure difference in the lane [Figure 2-10].

So, Gossett [72] firstly proposed a new dimensionless value defined as the ratio of shear induced lift force to secondary Dean drag force, R_f [E2-39]. He evaluates secondary Dean drag force by Stokes law and secondary dean velocity, which is proportional to $De^2\mu/D_h\rho$ [73]. Shear-gradient-induced lift force is chosen as $f'_L\rho U_m^2 D_p^3 D_H^{-1}$ [54], instead of $f_L\rho U_m^2 D_p^4 D_H^{-2}$ [53]. Clime also proposed a similar ratio [E2-40], defined as the ratio of two parameters in the particle velocity equation: lateral velocity [51] and Dean vortex flow velocity derived analytically [21]. The only different between Gossett and Clime's parameters is what they choose as the equation of shear-induced lift force. Both ratio can be interpreted as a function of confinement ratio λ and curvature ratio Δ .

$$R_f = \frac{(2R_p)^2(2R_c)}{D_H^3} = \lambda^2\delta^{-1} \quad [\text{E2-39}]$$

$$\Delta = \frac{R_p^3 R_c}{R_A^4} = \lambda^3\delta^{-1} \quad [\text{E2-40}]$$

$$N \cong \frac{36}{\text{Re}_c} \quad [\text{E2-41}]$$

Here, R_p is radius of particle, R_c is radius of curvature of channel, R_A is radius of cross section and D_H is hydraulic diameter.

These suggested new parameters, R_f and Δ , help us estimate inertial focusing behavior. For instance, if R_f is small (such as 0.01), drag force is dominant and particles are entrenched in the vortex. In the case that R_f is large (such as 1) inertial force is dominant and particles will be focused at a location identical to the one expected in in straight channel according to the explanation by Di Carlo. Between these two extreme cases (intermediate case), twin inertial focusing is generated at the inner-side of the channel [72, 74]. Di Carlo said that this intermediate ranges where twin inertial focusing show up starts at $R_f \sim 0.04$ [74]. Meanwhile, Clime [69] demonstrated, using both experiments and simulations, that a critical value of 0.148 for Δ can distinguish three regimes for the behavior of a particle in a coiled circular channel: if $\Delta < 0.148$, particles form circulating twin annuli; if $\Delta \approx 0.148$, particles are rotating near the inner wall; and if $\Delta > 0.148$, particles are focused in an inner equilibrium point following the two-step mechanism observed in straight channels. He also suggested the equation to determine the approximated channel length needed for inertial focusing [Figure 2-11].

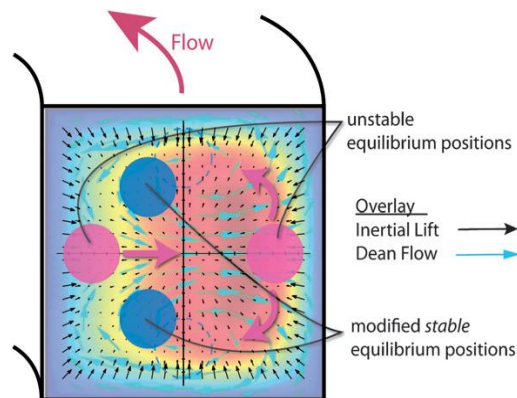
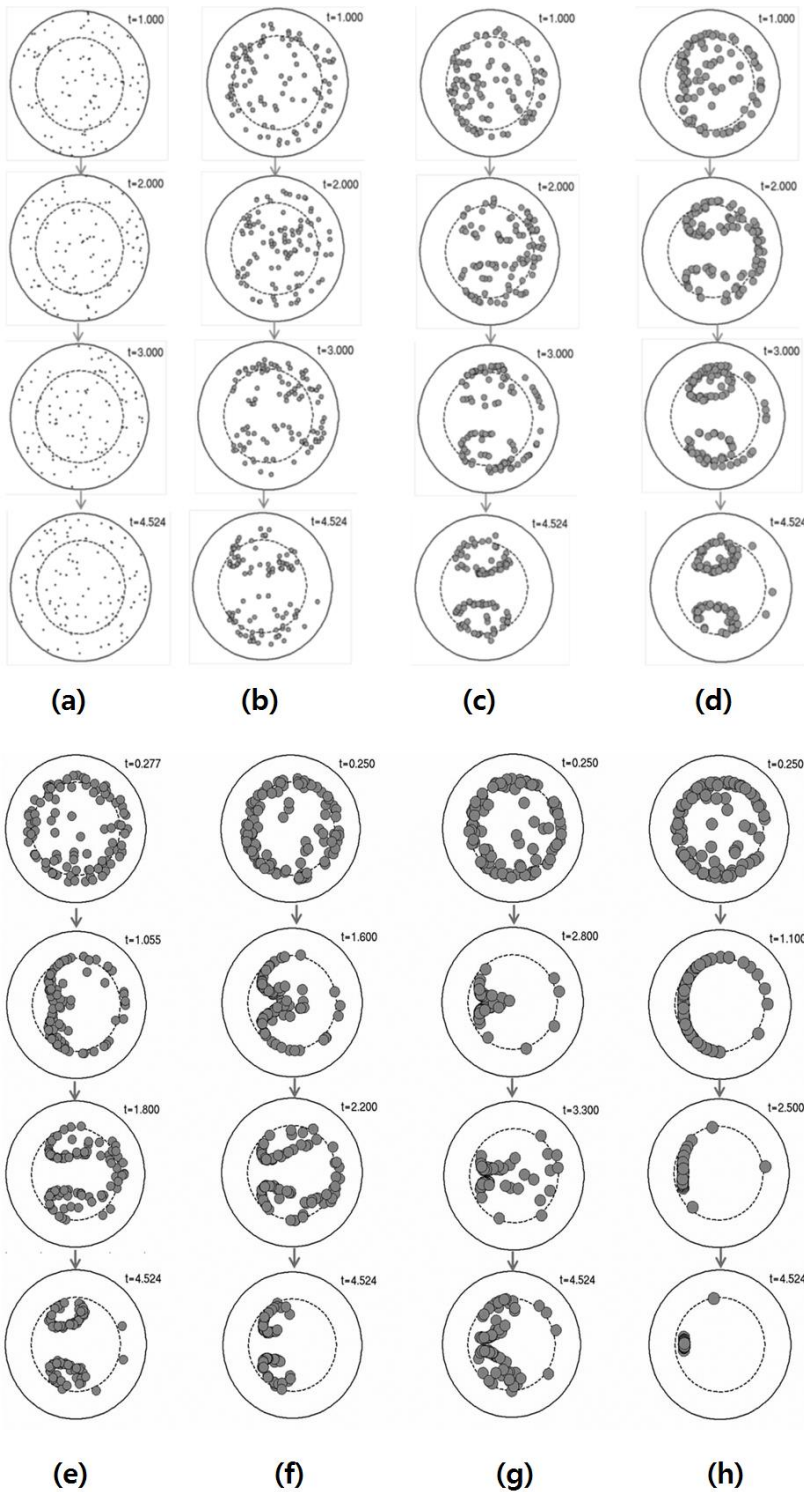


Figure 2-10 Schematic diagram for new equilibrium positions in curved channel explained by Di Carlo

Reprinted from Ref. [74] Di Carlo with permission. Pink circles are the focusing location for the strong inertial force case. Blue dots represent inertial focusing at the intermediate inertial force case of twin focusing. In secondary drag dominant case, in other words weak inertial force case, particle is continuously rotating along vortex and it doesn't experience focusing behavior.



- (a) $R_f = 0.12, \Delta = 0.0024,$
- (b) $R_f = 0.27, \Delta = 0.0081,$
- (c) $R_f = 0.48, \Delta = 0.0192,$
- (d) $R_f = 0.75, \Delta = 0.0375,$
- (e) $R_f = 1.08, \Delta = 0.0648,$
- (f) $R_f = 1.47, \Delta = 0.1029,$
- (g) $R_f = 1.73, \Delta = 0.1317$
- and
- (h) $R_f = 1.90, \Delta = 0.1536$

corresponding to particle diameter of 2, 3, 4, 5, 6, 7, 7.6 and 8 μm , respectively. 100 μm cross-section diameter and $Re=16$. Radius of curvature is 1.5 mm. axis of channel locates left on the picture. Series of pictures show the time evolution in seconds

Case (b) particles are rotating in entire half cross sections, same as streamlines of vortices

Case (f) particles are rotating but not same as streamlines of vortices. It looks focused near inner wall.

Case (h) also demonstrates two steps of inertial focusing observed in straight channel. Particles are focused near wall.

Figure 2-11 Inertial focusing for difference ratio value Δ
 Reprinted from Ref. [69] Clime.

However, the explanation of inertial focusing as the balance of shear-induced lift force and secondary Dean drag force is not a universal one. There are many experimental results that cannot be explained in such way. Di Carlo [75] conducted experiments in symmetric and asymmetric serpentine curvilinear channels and got a variety of results: one streak focusing, two streak horizontal focusing, multiple streak focusing, and no focusing. [Figure 2-12] Keinan's both experiment and computational simulation results demonstrate two streak horizontal focusing [17] [Figure 2-16]. Some of focusing even takes place far from the inner wall [16]. Guan [18] experimentally demonstrated twin inertial focusing in a spiral rectangular channel, with the inertial focusing location dramatically moving away from the inner wall as flow rate increases [Figure 2-13 left]. An even more intriguing focusing behavior was observed in curved channels with trapezoidal cross-section [Figure 2-13 right]. Similarly, Martel [71] investigated particle focusing in spiral channels in terms of particle size, channel Reynolds number, and curvature ratio. He demonstrated complex particle behavior including migration to/from the inner wall and transition from twin to single point focusing. Some of the results in Martel's work present multiple horizontal streaks for the inertial force dominant region, while multiple vertical streaks were observed in the intermediate region [71][Figure 2-15][Figure 2-14]. Such examples of complex focusing behavior might not be explained as the simple interplay between lift force and Dean flow. These eccentric behavior is usually observed in high R_f value or much coiled. More explanation needs.

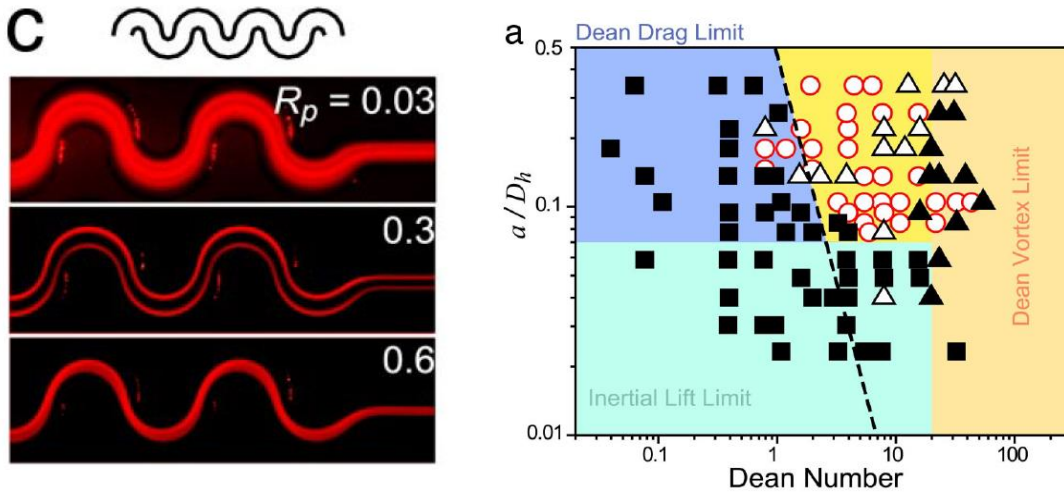


Figure 2-12 Inertial focusing in serpentine curvilinear channel

Reprinted from Ref.[75] Di Carlo. Left, a variety of inertial focusing behavior in a serpentine channel (9 μm particles, 50 μm square channel). Right, results for focusing as a function of Dean number and confinement ratio λ . Open circles mean single streak and open triangles mean for double horizontal streaks. Filled squares and triangles means no focusing or more than four streaks

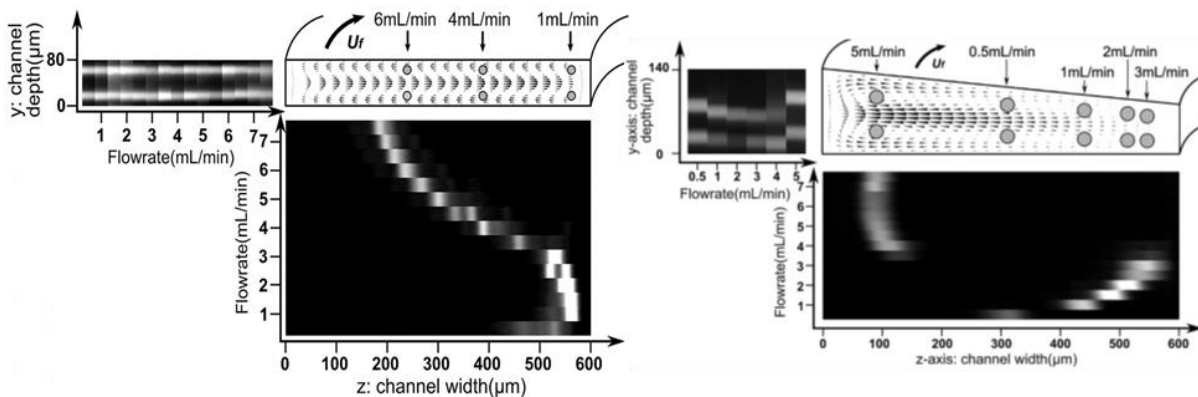


Figure 2-13 Experimental verification of inertial focusing in spiral channel

Reprinted from Ref.[18] Guan. (Left) Rectangular channel. Vertical twin inertial focusing is observed inner at the wall of the channel at low flow rate, which can be explained as the balance of shear-induced force and secondary drag force. However, the inertial focusing location changes and moves away from the inner wall as flow rate increases, which needs more explanation. (Right) Trapezoidal channel. Twin inertial focusing is generated, too. However, sudden jump of position of inertial focusing is observed as flow-rate is increased.

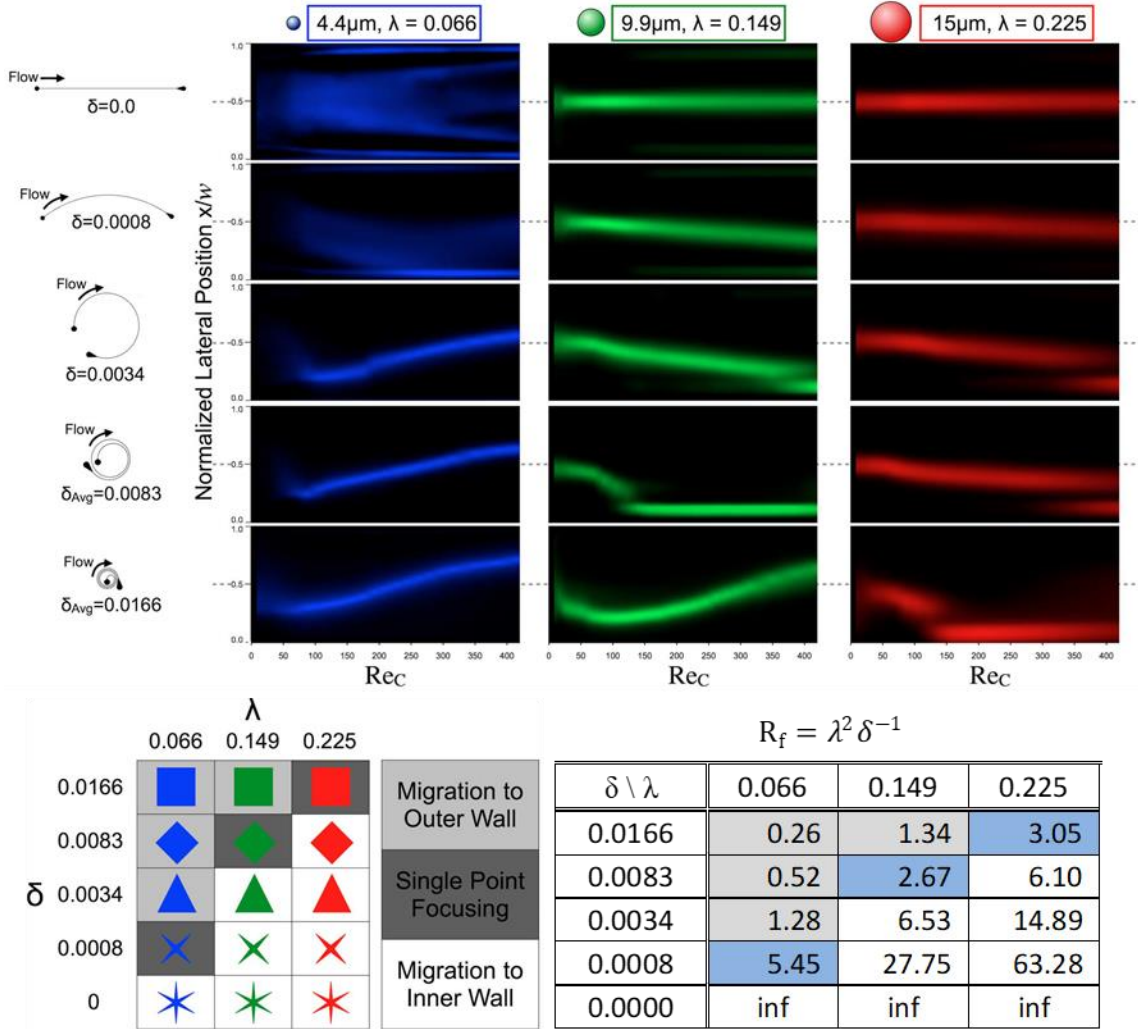


Figure 2-14 Relationship between R_f and focusing tendency

Reprinted from Ref.[71] Martel. Location of inertial focusing varies in terms of Reynolds number and its tendency is determined by R_f . A device with $R_f = \lambda^2 \delta^{-1} > 4$ will cause focusing behavior towards the inner wall of the curved channel while a device with $R_f = \lambda^2 \delta^{-1} < 4$ will cause focusing behavior towards the outer wall of the curved channel. $R_f \sim 4$ demonstrates single lateral point focusing, independent of Reynolds number.

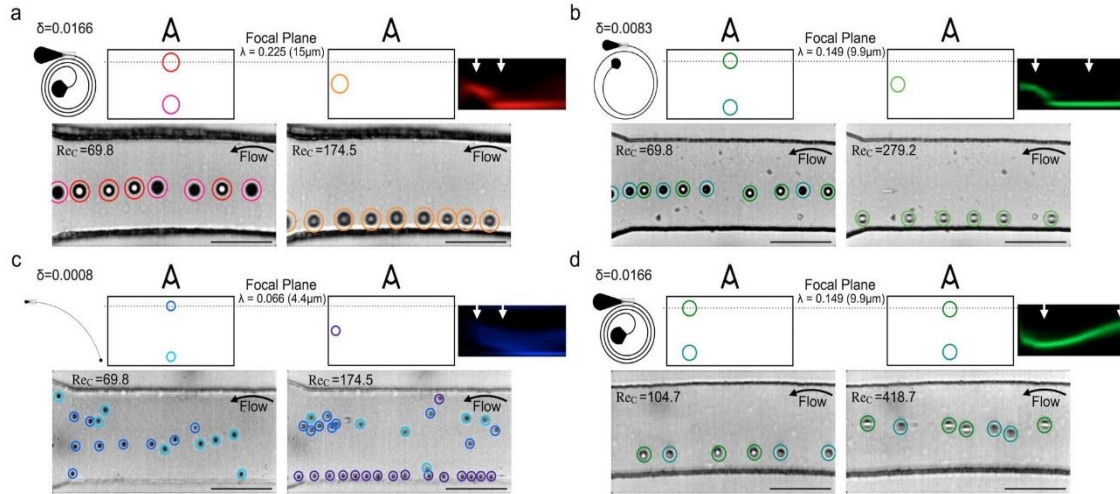


Figure 2-15 Inertial focusing in spiral channel by Martel

Reprinted from Ref.[71] Martel. Two-streak vertical inertial focusing get reduced to one streak near the inner wall as channel Reynolds number is increased (see a, b and c). However, twin vertical focusing just moves outward from the inner to the outer wall for certain Reynolds number cases (see d). Horizontal multiple focusing is also observed in specific cases (see c). R_f values are 3.05, 2.67, 5.45 and 1.34 in a, b, c and d, respectively. Here, $Re_c = \rho U_{max} D_h \mu^{-1} = 1.5 \rho U_{avg} D_h \mu^{-1}$

2.4.3 New concepts to explain inertial focusing in curved channel.

2.4.3.1 Non-parabolic velocity profile

Keinan [17] experimentally demonstrated presence of multiple horizontal streaks in the inertial force dominant region with, R_f of 2.33 [Figure 2-16]. He suggests a new explanation for this phenomenon against the conventional theory in which focusing is the balance of wall-induced force, shear-induced lift force and Dean drag force. He argues that focusing at high Reynolds numbers results from opposing shear-induced forces in a curved channel. Actually, velocity profiles in curved channels are not parabolic, rather a combination of convex-concave curves [Figure 2-16] and [Figure 2-17]. Focusing occurs at convex-concave inflection point and it could be multiple. His simulations based on general force equation by Ho and Leal [49][E2-17], are well matched to both his experimental results and computational calculation, with shear-induced lift force being the dominant one [17].

The maxima of the velocity are traversing as flow rate is changing: if flow rate is low, the maximum is near the inner wall and it goes outwards as flow rate is increased [Figure 2-18]. It could be a good explanation for the dependence of position of inertial focusing on flow-rate. Also, this could be a good explanation for inertial focusing in trapezoidal channels and its dependence on flow rate [18][Figure 2-13 right] [4][Figure 2-17].

Note that velocity profiles in straight channels could also be of non-parabolic shape. Flat-like velocity profiles are observed along longer side of rectangular channels with extreme aspect ratio [6][Figure 2-8 (c)]. It might be the reason why particles are not focused in two points in rectangular channel of extreme aspect ratio.

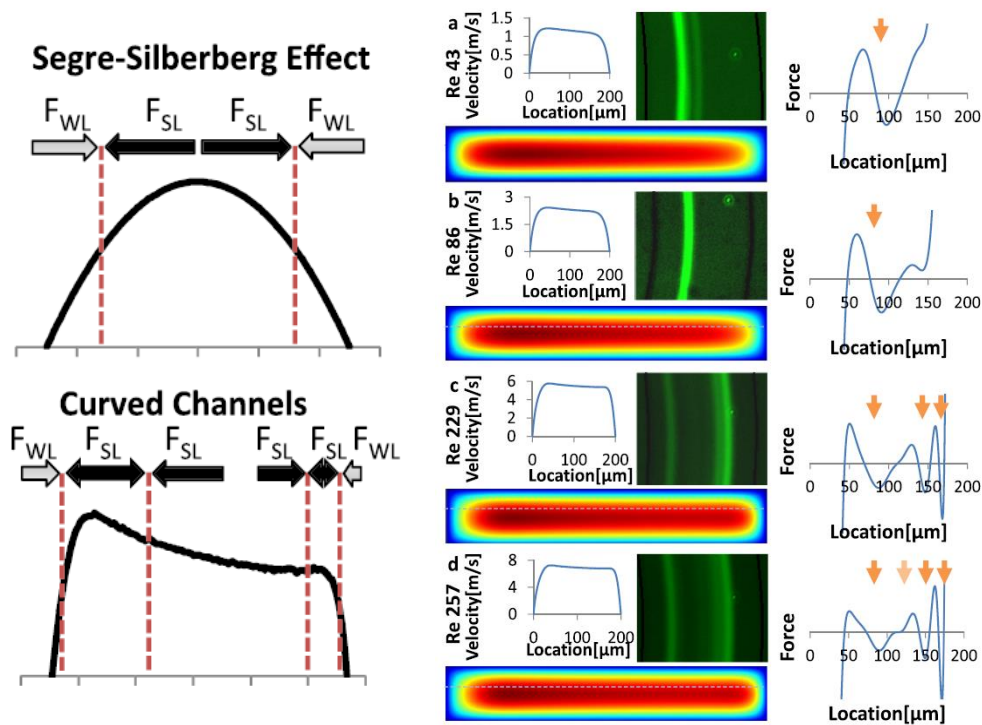


Figure 2-16 Non-parabolic velocity profiles and inertial focusing in curved channel

Reprinted from Ref.[17] Keinan with permission. The location of inertial focusing estimated by theoretical force balance is well fitted to experimental results. Channel geometry is $33 \mu\text{m}$ height and $200 \mu\text{m}$ wide, with a radius of curvature of $900 \mu\text{m}$; $15.5 \mu\text{m}$ particle diameter and R_f is 2.33.

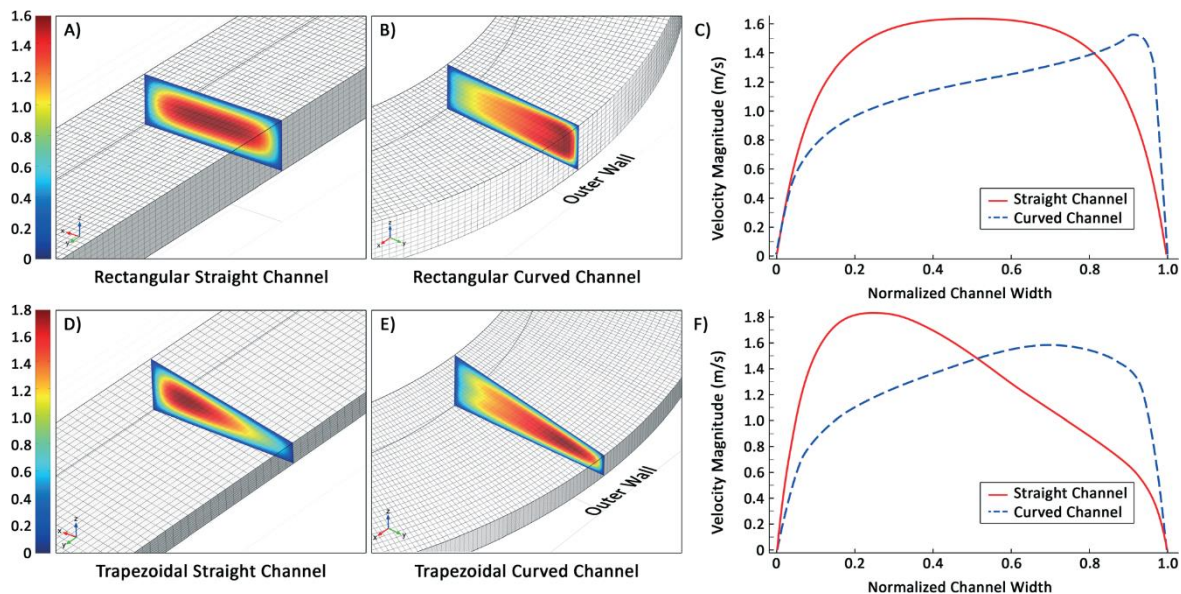


Figure 2-17 Velocity profiles in trapezoidal channels.

Reprinted from Ref.[4] Rafeie with permission. Axial velocity contour graphs(left) and velocity profiles at the middle of cross-section (0 is inner wall and 1 is outer wall) (right). In the curved channels shown, velocity profiles are not parabolic, and the velocity maximum is located near the wall.

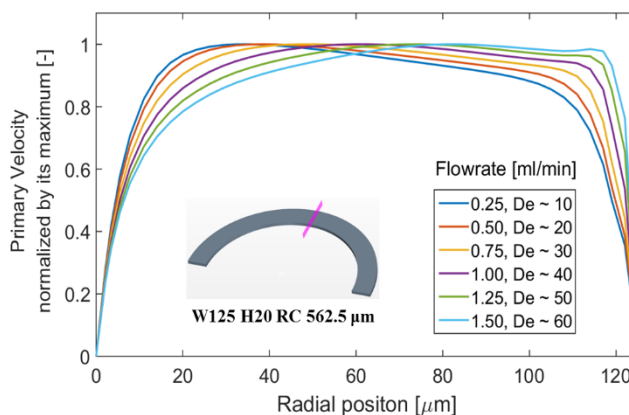


Figure 2-18 Normalized primary velocity profiles in curved channel in a variety of flow-rate

Computational result by STAR-CCM+. The maximum is near the inner wall in low flow-rate and it go outwards as flow-rate go increased. Radial position 0 mean inner side of channel which is nearest to axis of curvature. Inset represents the curved channel used in the simulations and the position where velocity profiles are obtained. Its geometric parameters is identical to inner lane of channel used in this paper. Radius of curvature is 562.5 μm and width and height of cross section are 125 and 20, respectively.

2.4.3.2 Multiple vortices

If the Dean number is high, multiple vortices (more than two) are generated in a curved channel [16, 76][Figure 2-19]. Nivedita [16] demonstrates particle focusing in terms of Dean number experimentally and explains it as if particles are entrenched in secondary vortices that makes look like particle focusing. She also suggested a critical Dean number, determining the number of vortices in curved channels, as a function of the aspect ratio of the rectangular channel [Figure 2-20][Figure 2-21].

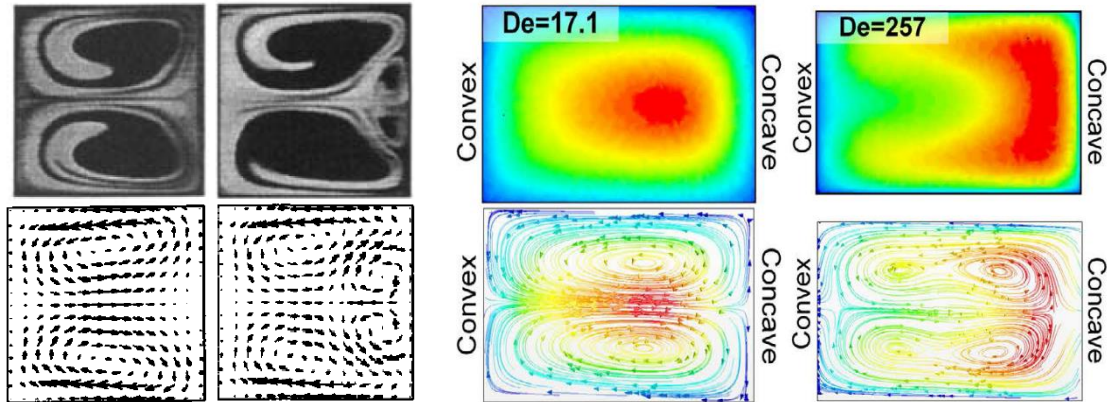


Figure 2-19 Multiple vortices

Reprinted from Ref[76] Bara with permission. Left, flow visualization in experiment and secondary flow by numerical simulation with Dean numbers of 125 and 137, respectively. Reprinted from Ref.[16] Nivedita. Right, velocity contour and streamline by computer simulation. As the Dean number increases, the number of vortices increased from two to four.

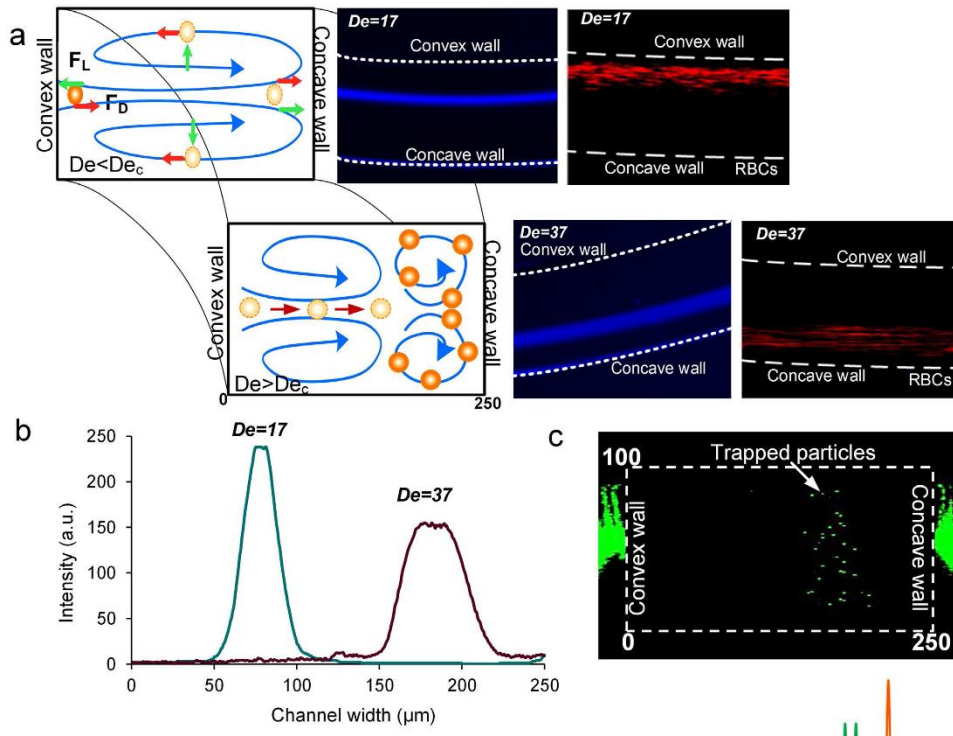


Figure 2-20 Particle focusing in multiple vortices

Reprinted from Ref.[16] Nivedita. (a) Schematic of the process of particle entrapment and corresponding experimental results using particle and RBC, respectively. (b, c) Intensity graph and confocal image for particle experiments. Geometries of channel employed as follow. Radius of curvature (R_c) is 3120-4120 μm , Hydraulic diameter (D_h) is 142 μm (250 μm x 100 μm) and Diameter of particle (D_p) is 10 μm . R_f value is 0.218-0.287. Dean number is from 37 to 17

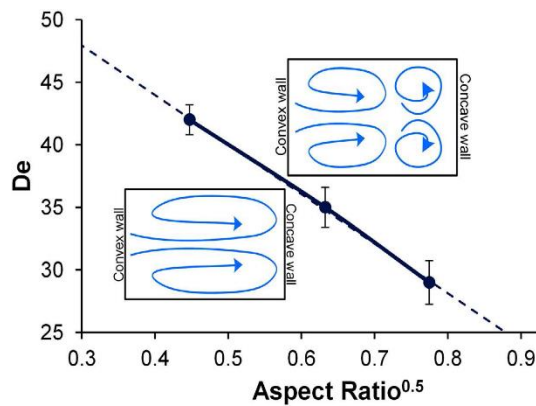


Figure 2-21 Plot of the critical Dean number as a function of the aspect ratio AR

Reprinted from Ref.[16] Nivedita. Critical Dean number, which determine the number of vortices, is inversely proportional to aspect ratio, AR . $De_c \propto AR^{-0.5}$ (the graph miss minus sign on exponent term)

Ha [29] also demonstrated similar results using both experiments and simulations, in which particles are trapped between vortices when multiple vortices are present. His simulation is conducted by both dye concentration profiles [Figure 2-22] and particle tracking with Saffman lift force [Figure 2-23]. Both cases provide similar results, although they do not consider shear-gradient-induced lift force. It would be evidence for secondary drag force to be dominant in multiple vortices case.

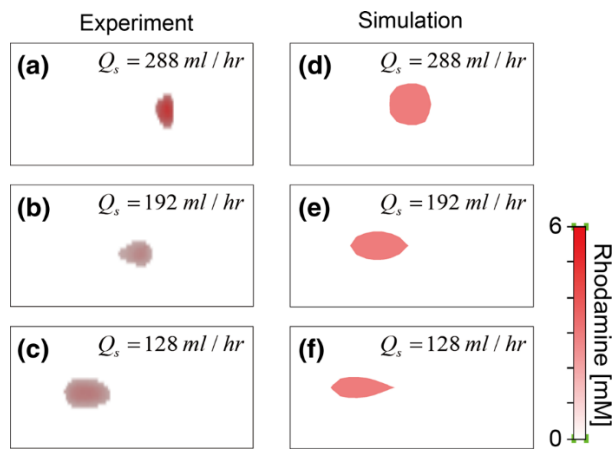


Figure 2-22 Experiment and simulation of dye entrapment by vortices in curved channel

Reprinted from Ref.[29] Ha with permission. Right-hand side is inner wall. Flow rate is 4.8, 3.2 and 2.13 ml/min, respectively. Dean number decreased from 356 to 237, and 158, respectively

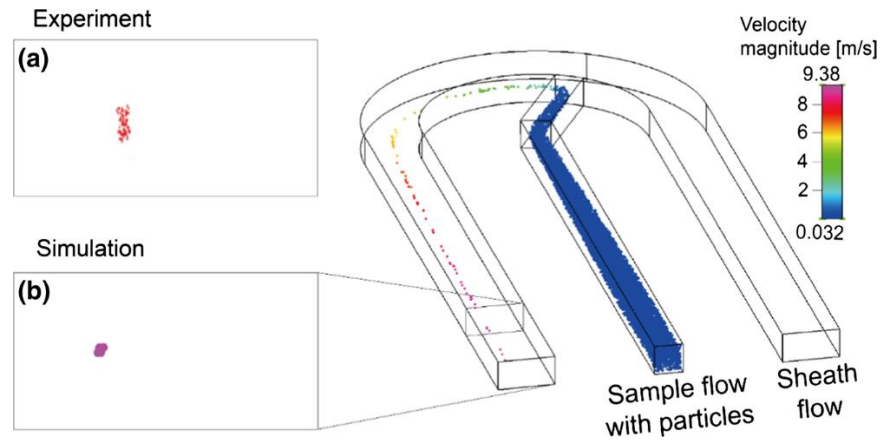


Figure 2-23 Experiment and simulation by particle entrapment by vortices in curved channel.

Reprinted from Ref.[29] Ha with permission. Particle diameter is $3.2 \mu\text{m}$, Hydraulic diameter is $133.3 \mu\text{m}$ and radius of curvature is $500 \mu\text{m}$. R_f is 0.0043

2.4.3.3 Vertical shear-induced lift force.

One of the common misconceptions in the fields of microfluidics in curvilinear channels is that shear-induced lift force by primary flow is only perpendicular to the channel axis. Sometimes, vertical shear-induced lift force might play a critical role in inertial focusing. By considering forces in the vertical direction, particle trajectories that look like inertial focusing are produced in the computational simulation, referred as to quasi-inertial focusing. Balance of horizontal force is not important in this case. Even only using Saffman lift force, considered much smaller than shear-induced lift force [50] (see Section 2.2.3), is able to produce quasi-inertial focusing in computational simulations [Figure 2-24]. See Section 3.4.6 for a detailed description of the mechanism involved. Similar phenomena are observed in simulations by Clime [69], see [Figure 2-11].

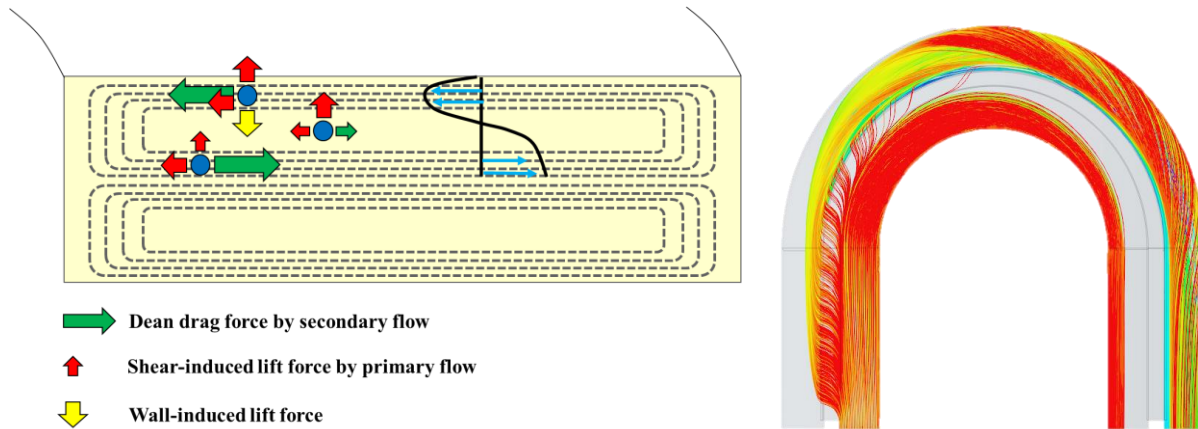


Figure 2-24 Quasi-inertial focusing in curved channel, vertical shear-induced lift force plays an important role


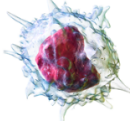
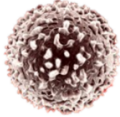
Left, Schematic diagram for quasi-inertial focusing. Dashed lines represent the streamline for secondary flow. Blue circles are the particles. Shear-induced lift force allow particles to migrate vertically and to cross streamline, switching the direction of horizontal migration. It produces quasi-inertial focusing. Right, particle simulation shows particles being focused in the inner wall of the inner lane at the outlet part. 3.5 μm particles and 1.5 ml/min flow rate at each lane. R_f is 0.33 and 0.08 for the inner and outer lanes, respectively.

2.5 Characteristics of the particles

Red blood cells (RBCs) are one the most common particles in blood, whereas CTCs are our target cells to be enriched. Understanding characteristics and properties of these cells is important for the design of separation devices based on inertial focusing. Human blood contains 5 million red blood cells per microliter. A typical human red blood cell has a biconcave disk-shape with diameter of 6.2 – 8.2 μm and height of 2 – 2.5 μm in its thick part and 0.8 – 1 μm in its thin part [77]. If we assume that these cells are spherical, a sphere with the same volume would have a radius of ~ 2.3 – 2.9 μm . In contrast, circulating tumor cells are found in frequencies on the order of 1 – 10 per milliliter in blood [78]. PC-3, a widely studied type of CTC has a diameter of 20 μm . Not only their size, but their deformability is also different, with RBCs over 100 times more deformable than CTCs [79]. Considering these size, shape, and deformability differences, we

hypothesize that small, flat and deformable RBCs will easily pass through the narrow spaces in our filtration device, while spherical rigid CTC will be retained and enriched.

Table 2-1 Characteristics of cells in the blood.

	Red blood cell (RBC)	White blood cell (WBC)	Circulating tumor cell (CTC)
Picture			
Shape	Biconcave Disk-like	Sphere	Sphere
Size	Diameter of 6.2-8.2 μm Height of 2-2.5 μm	Neutrophil 10-12 μm Lymphocyte 7-15 μm	>15 μm
Concentration	5×10^9 cells / ml	4×10^6-1.1×10^7 cells /ml	1-10 cells / ml
Deformability	1 (Healthy RBC)	20-60	100

3. PARTICLE SIMULATION

3.1 Channel design and particles for simulation

The design of the microchannel suggested by Huang [10] for size-based particle separation is studied by 3D computational simulations in this paper. The functional part of the device is comprised of three consecutive segments forming a U-like geometry: a straight segment where inlets are located at the beginning, a curved segment, and another straight segment with outlets at the end Figure 3-1. Along these segments, there are two parallel lanes connected by a bridge, which facilitates the transfer of particles smaller than the height of the bridge. The direction of particle transport is determined by the pressure difference between lanes: from high pressure lane to low pressure lane. This pressure difference between lanes can be attributed to a number of factors (e.g., cross sectional size and shape of each lane, flow-rate, and curvature of bending of the lanes) that will be investigated in later sections. Thus, to operate the device, particle solution is injected into inlet 1 (inner lane) and sheath flow into inlet 2 (outer lane). Small particles or cells such as RBCs can pass through the bridge and get to the outer lane to be later collected at outlet 2. However, large particles such as CTCs stay in the inner lane and are enriched because they cannot pass through the narrow bridge, so they can be collected at outlet 1. By doing so, particles are separated based on their size.

As mentioned above, the cells relevant for our simulations are RBCs and CTCs. RBCs are assumed to be rigid spheres with diameters of 2-3.5 μm , considering computational efficiency and minimum size of RBCs to pass through the narrow height of the bridge. Diameter of CTCs is known as 15-20 μm and these values are considered for channel design. Thus, the height of the

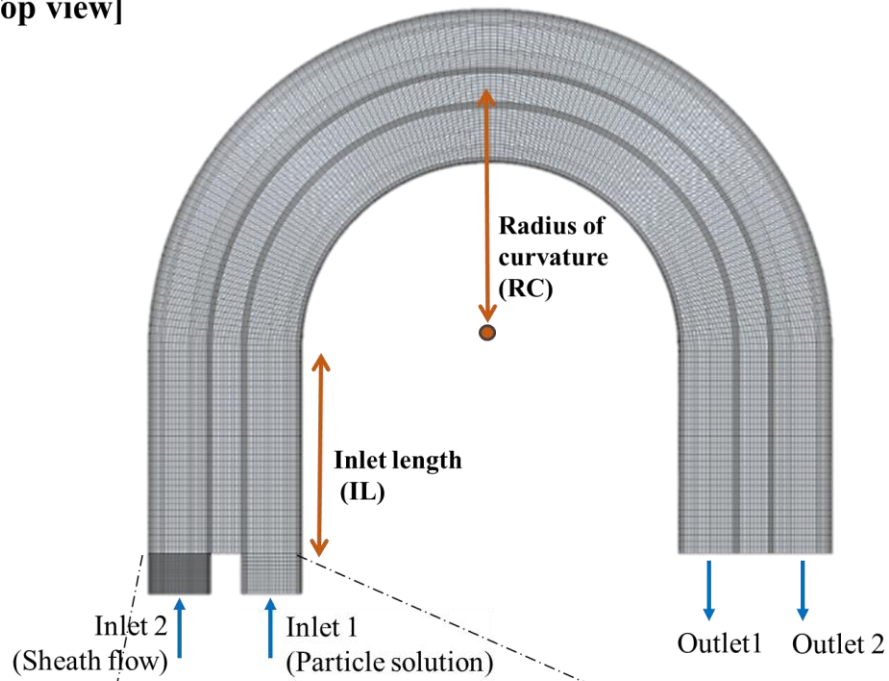
bridge is selected as 7 μm , a value between the sizes of the two kinds of cells to be separated. Notice that particle simulation for CTCs is actually not conducted because it is obvious that CTCs cannot pass the narrow bridge. Only simulations for particles modeled as RBCs are conducted here.

3.2 Separation efficiency: performance indicator

The ability of the microfluidic device to sort particles based on their size will be measured using the concept of separation efficiency (SE), which is defined as the ratio between the number of target cells collected and the number of target cells in the original sample [80]. The concept of SE can be applied in this study as the ratio of the number of particles coming out through the outer outlet (outlet 2) to the number of total particles injected into the channel (inlet 1), as seen in equation [E3-1]. High SE means that small particles pass through the narrow bridge well and the channel is good for separating RBCs from CTCs in blood. Also, because CTCs are expected to remain in the lane where they are originally injected and RBCs and blood plasma are migrating through the bridge, high enrichment of CTCs can be achieved. Therefore, SE for RBCs is evaluated and employed in our simulations as a performance indicator for the microfluidic device.

$$\text{Separation efficiency [SE]} = \frac{\text{particle rate at outlet 1}}{\text{particle rate at inlet 2}} \quad [\text{E3-1}]$$

[Top view]



[Cross section view]

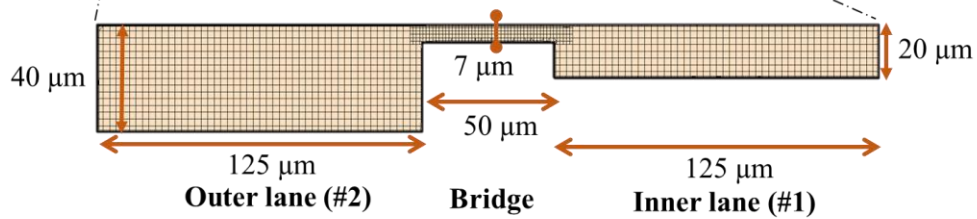


Figure 3-1 Microchannel modeled in simulation

3.3 Simulation methods

A commercial computational fluid dynamics (CFD) software, Star-CCM+ ver. 11.040.10 is employed to perform simulations of the particle separation process. These simulations are comprised of two interconnected parts: fluid simulation and particle simulation. The goal of fluid simulation is to solve velocity and pressure profiles in the channel. Unsteady incompressible

laminar Navier-Stokes equations are selected as fluid model, with all fluid properties specified as those of water at 25 C°.

Particles trajectories, which is the goal of particle simulation, are calculated by Lagrangian specification. Particles are spherical and rigid, with their density specified as 1100 kg/m³, mimicking the density of ordinary cells, and Poisson's ratio and Young's modulus specified as 0.45 and 0.517 MPa, respectively. The kinds of forces to be applied to particles in the simulation are selected as described below. Drag force and pressure gradient force are applied using built-in functions. However, Star-CCM+ does not have built-in functions for shear-induced lift force and wall-induced lift force. Thus, as second-best option, shear-induced lift force is substituted by Saffman lift force, justified in that design parameters considered in this study are in the secondary Dean drag force dominant region. Shear-induced lift force cannot be replaced by Saffman lift force in the inertial force dominant region where inertial focusing is generated by direct offsetting of lift forces in the horizontal direction. Saffman lift force, however, could work in the secondary Dean drag force dominant region to emulate the effect of the shear-induced lift force and allow particles to cross the streamline to switch the direction of particle motion. Although the magnitude of the Saffman lift force is about one order of magnitude smaller than the most significant shear-gradient-induced lift force, it could reproduce a similar tendency. Shear-induced lift force could be added later as a user-defined function if necessary. Also, instead of wall-induced lift force, two-way coupling and pressure gradient force are employed. This would be a good approximation because the pressure change induced by the proximity of a particle to a wall is the main source of wall-induced force. Finally, the Hertz-Mindlin contact model, one of the interaction models incorporated into DEM, is applied to consider physical filtration by the narrow channel while accounting for particle-particle and particle-wall interactions.

3.4 What parameters are important for particle separation?

Separation efficiency in our microfluidic device depends on a number of factors as discussed in the following. As a first step, let's assume that there isn't a bridge between the two lanes, so it would be two microchannels under laminar flow conditions. In this case, the pressure drop along the primary direction, $|\Delta p|_{primary}$, can be easily estimated by the Hagen-Poiseuille equation [E3-2].

$$Q = \frac{\pi}{128} \frac{|\Delta p|_{primary} D_H^4}{L \mu_f} \quad [E3-2]$$

$$|\Delta p|_{secondary} = \left| |\Delta p|_{primary,1} - |\Delta p|_{primary,2} \right| \quad [E3-3]$$

where, Q is flow-rate, Δp is pressure drop and subscript primary with pressure drop, $|\Delta p|_{primary}$, refers to pressure drop between channel ends. Subscript secondary with pressure drop, $|\Delta p|_{secondary}$, is defined as difference of primary pressure drop between two parallel lanes [E3-3].

This equation also lets us realize that the pressure difference depends on the geometry of the channels $f(D_H, L)$ and flow rate Q . So, inlet length and the shape of each channel (that is, channel cross-section) are geometric parameters to be investigated, along with the effect of flow rate, which, if it is high enough, is able to induce vortices in straight segments and particle focusing at the end of the channel. Other geometry-related parameters to be investigated include injection angle at the beginning of the straight channels and radius of curvature of the curved segment of the channel. Injection angle for particle solution and sheath flow might be critical to particle separation because of secondary flows induced by tilted injection could either accelerate or decelerate particle migration. Dean flow and vortices in the curved segment is the other way to generate secondary flow in this device; the larger the radius is, the smaller the induced Dean flow is.

Finally, particle-related parameters such as their size and concentration are also investigated. Particle size, in particular, is a critical parameter because there are a lot of size-depending forces

exerted on a particle such as: secondary drag force, proportional to particle radius; shear-gradient lift force, proportional to cubic radius; and wall-induced lift force, proportional to radius to the sixth power. The net force acting on a particle makes the particle migrate and could result in inertial focusing in the channel, thus affecting separation efficiency.

In summary, seven parameters and their effects in particle separation will be investigated in this paper: inlet length (IL), injection angle (AG), shape of cross sections, and radius of curvature (RC) as geometric parameters, and inlet flow-rate (FR), particle concentration, and particle diameter (PD) as operational parameters.

3.4.1 Inlet length

Simulations of 40 cases with different inlet lengths, inlet flow-rate, and particle sizes are conducted, and their separation efficiency is summarized in [Figure 3-2]. This result indicates that separation efficiency is very sensitive to inlet lengths for flow rates ≥ 1 ml/min, reaching maximum values at inlet lengths of 2000 μm for particle diameters of 2 and 3 μm . At lower flow rates, however, inlet length appears to have little effect on separation. A key to explain this phenomenon is found in the fluid behavior at the inlet. Water at identical flow rates is injected at the entrance of both lanes. Given that the inner lane, where particles are injected, has a smaller cross section, the inner lane then has a higher pressure than the outer lane. This creates a secondary flow from the inner lane to the outer lane [Figure 3-3 (a)]. As fluid is transferred from the inner lane to the outer lane, pressure becomes identical and the secondary flow is diminished. Because the main reason that particles pass through the bridge is secondary drag force in the straight segment, particles do not migrate anymore after the point where pressure becomes the same on both channels [Figure 3-3 (b)]. If inlet lengths are too long, reverse pressure and reverse flow occurs and migrated

particles go back to the inner lane. That is the reason why a long straight channel does not perform as well as the channel with optimum length does [Figure 3-3 (c)]. Our simulation results show that there is an optimal inlet length for particle separation. When the inlet length is the same as the length at which the pressure difference becomes zero, separation efficiency is maximized.

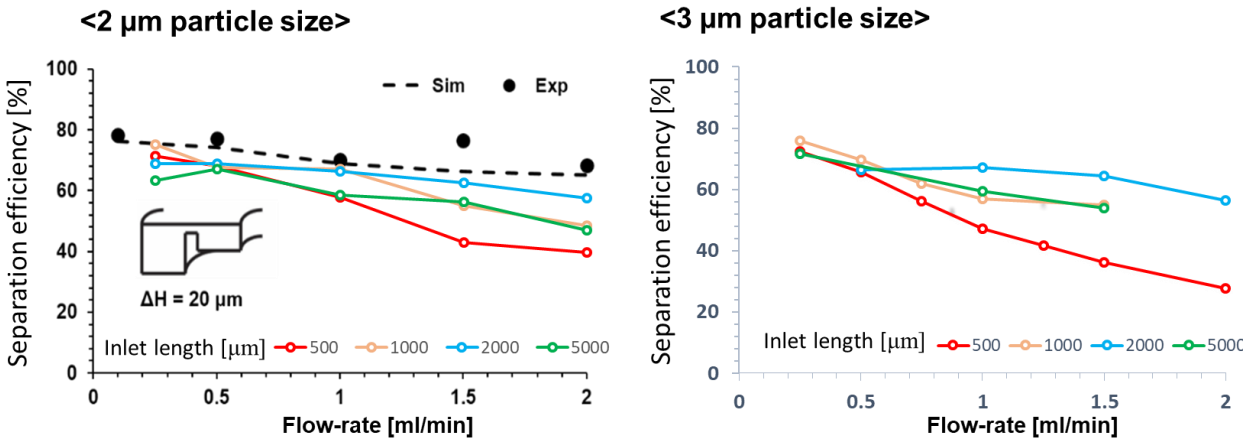


Figure 3-2 Separation efficiency in terms of flow rate for different inlet lengths and particle sizes

(i) Inlet length: for a given flow rate, maximum separation efficiency is observed for 2000 μm inlet length, especially at high flow rates. (ii) Flow-rate: there is a tendency for separation efficiency to decrease as flow-rate increases, irrespective of inlet length. (iii) Particle size: the bigger the particle is, the lower the separation efficiency is; although this doesn't seem evident from these figures, a later discussion, see Figure 3-13, clearly shows such behavior. Black dots and dashed line correspond to previous experiments and simulations, respectively, done by Priye [81]. Notice that Priye's simulation consider no shear-induced lift force, or even Saffman lift force.

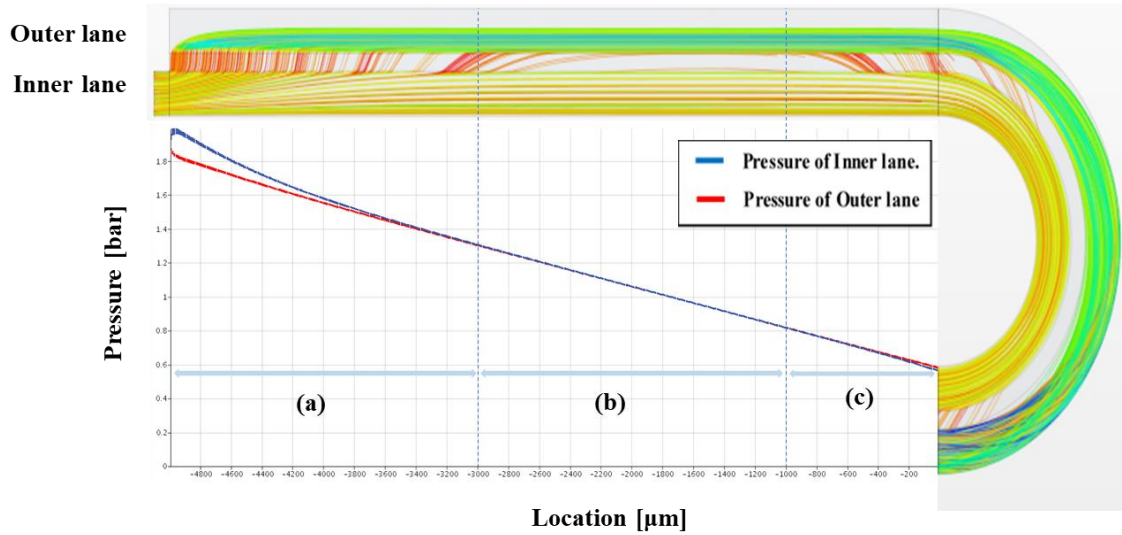


Figure 3-3 Relationship between pressure difference and particle migration

Top view of particle simulation with inlet length of 5000 μm and the corresponding pressure graph for the straight channel. Particles are injected into the inner lane at the entrance, left-hand side of the picture. Its movie clip is attached as appendix S1. (a) At the beginning of the channel, the inner lane has higher pressure than the outer lane. So, fluid and particle migrate from the inner lane to the outer lane. (b) Pressure of the lanes becomes identical and migration does not occur. (c) If the inlet length is too long, reverse flow occurs and particles already transferred to outer lane get back into the inner lane. Each line on the channels means the trajectory of particles. Color of the lines represents the location of the particle in terms of height: red means near the top of the channel while blue means near its bottom.

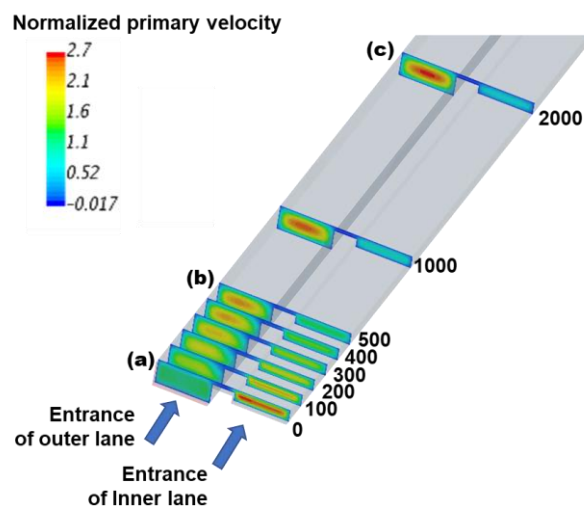


Figure 3-4 Simulation results for primary velocity at inlet length

Contour graphs in each cross-section represent primary velocity normalized by inlet velocity at the outer lane. Primary flow means the flow parallel to the channel. Numbers next to the channel mean distance from the entrance in micrometers.

The pressure difference between lanes not only generates the secondary flow, but it also changes the pattern of primary flow as we move through the channel. At the beginning of the channel, the inner lane has higher velocity than the outer lane, which makes sense because the inner lane has small cross-section and the same flow-rate [Figure 3-4 (a)]. As fluid is transferred through secondary flow, however, primary velocity in the outer lane turns out to be higher than that in the inner lane, resulting in a switch in primary velocity as we move through the channel [Figure 3-4 (b)]. So, even though flow-rate was identical at the entrance, the ratio of inner to outer lane flow-rate at the end of the channel becomes 1:6 [Figure 3-4 (c)]. Thus, the concentration of cells that are not transferred across the bridge such as CTCs is tremendously increased in the inner lane at the end of the channel; this enrichment of CTCs makes it easier to conduct CTC enumeration and analysis for cancer diagnosis.

Also, an interesting phenomenon is observed with the pressure drop between lanes. No matter how long the inlet length is and what the flow-rate is, the pressure difference becomes zero at almost identical locations inside the channel, $\sim 2000 \mu\text{m}$ from the entrance, if the rest of the channel geometry remains the same. The factors that determine the length for diminishing pressure difference are not yet known.

3.4.2 Flow rate

At a first glance, high flow rate at the inlet should result in high separation efficiency. This, however, is not true. The results in [Figure 3-5] demonstrate that separation efficiency decreases as the flow-rate increases. This might be explained using the concept of pressure gradient ratio, the P-value suggested by Priye [81] and later discussed here in Section 3.6, which is directly proportional to separation efficiency. The P-value is also inversely proportional to primary

pressure drop, estimated by Hagen-Poiseuille equation [E3-2], which is proportional to flow-rate. Summarizing, an increment of flow-rate results in a decline of P values [Figure 3-5], followed by lower separation efficiency. Also, vortices are induced even in the straight channel at high flow rate, as shown in [Figure 3-6].

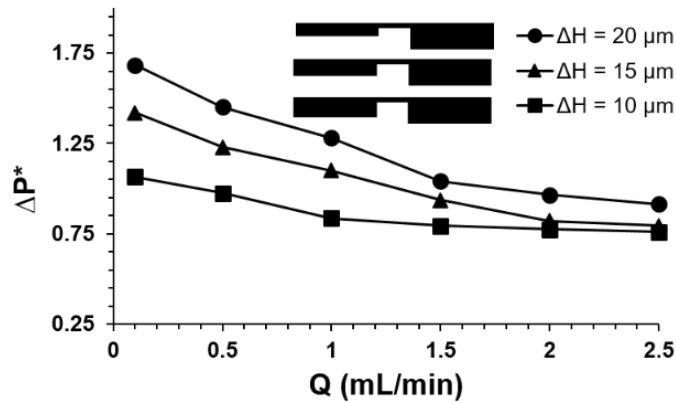


Figure 3-5 The P value as a function of flow-rate

Reprinted from Priye [81].

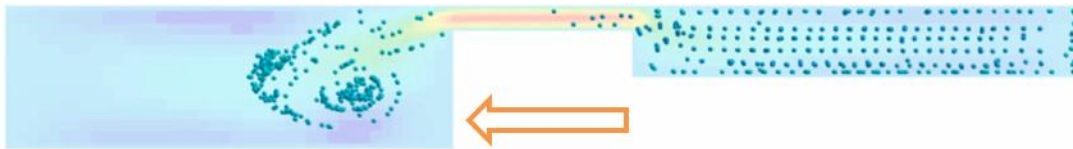


Figure 3-6 Cross section of channel at the beginning of the straight channel

Cross-section view at the beginning of the channel. Secondary flow direction is from right (inner lane) to left (outer lane). Particle migration due to pressure difference is observed, and a high flow-rate of 1.5 ml/min generates a vortex even in a straight channel. Color represents secondary velocity: red indicates outward flow (to the left) and blue inward flow (to the right).

3.4.3 Shape of cross section

One of the easiest ways to generate pressure difference across the parallel lanes is using different cross-sectional shapes for each lane. To generate a secondary flow from the inner to the outer lane, in a case with equal flow-rates in both lanes, the outer lane has to have larger cross-sectional area (height*width in a rectangular channel) than the inner one does. According to previous research by Priye [81][Figure 3-7], height differences between the two rectangular lanes are significant factors for particle separation. The larger the height difference is, the more particle migration occurs. Widening the cross section is not helpful to yield high separation efficiency. The aspect ratio of each lane is also a parameter to be investigated. If the height is longer than the width, neither vortices nor particle migration occur properly in the curved part of the channel.

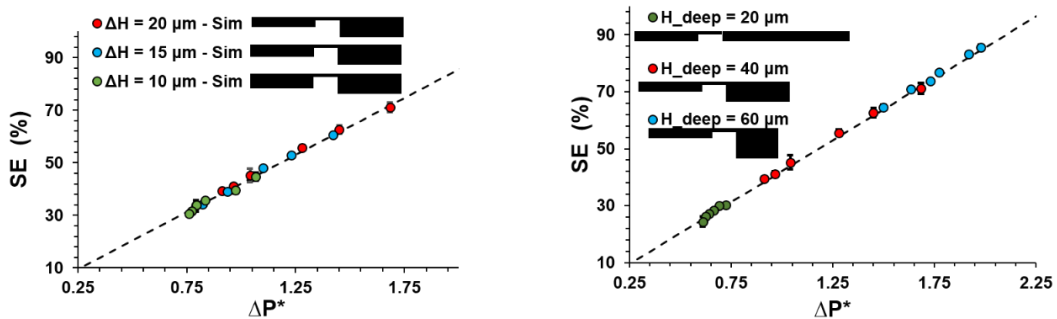


Figure 3-7 Graph for separation efficiency in terms of P value

Results from Priye [81]. Particles are injected in the left lane (first lane, where particles are injected) and then transferred to the right lane (second lane, where small particles are transferred to and separated) through the bridge. Separation efficiencies are evaluated in (a) geometries of different height and the same width, and (b) geometries of different aspect ratio with the same cross-sectional area for the first lane. Separation efficiency is sensitive to the height of the second channel and, more importantly, it is directly proportional to P value defined later in equation. The definition of P value is pressure gradient ratio and explained in Section. Dimensionless pressure for device design 3.4.7

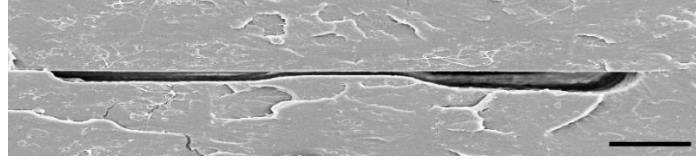


Figure 3-8 SEM image of actual cross section of the channel

This channel was fabricated by Huang employing enzymatic sculpting technology, whereas physical etching is employed to fabricate the devices produced by Design 1 Solutions in this study. Reprinted from ref.[10] with permission.

Until now, the cross section of each lane in the device has been assumed to be rectangular in shape. However, as it can be seen from the SEM image in [Figure 3-8], a more accurate model would be a trapezoidal cross section. Thus, channels with trapezoidal cross section are also investigated. The Figure 3-9 below illustrates separation efficiency for four cases: flow-rates of 0.5 and 1.5 ml/min for rectangular and trapezoidal cross-sections. The graph demonstrates that the trapezoidal channel has higher separation efficiency than the rectangular channel does, even though the area of the cross section in the rectangular channel is bigger than the one in the trapezoidal channel [Figure 3-9 (b-d)]. It would be better to match cross sectional areas for a more accurate comparison in future works. Despite this fact, these results are worthwhile to give us insight about how the shape of the channel is also a significant factor to be investigated for separation efficiency.

Guan [18] also studied channels with trapezoidal shape, reporting that there is a sudden switch of inertial focusing at certain thresholds of flow-rates, which is not observed in ordinary rectangular channels. Reference [4] explains this as abrupt changes of velocity profiles in trapezoidal channels. See Section 2.4.3.1 for additional explanation and details.

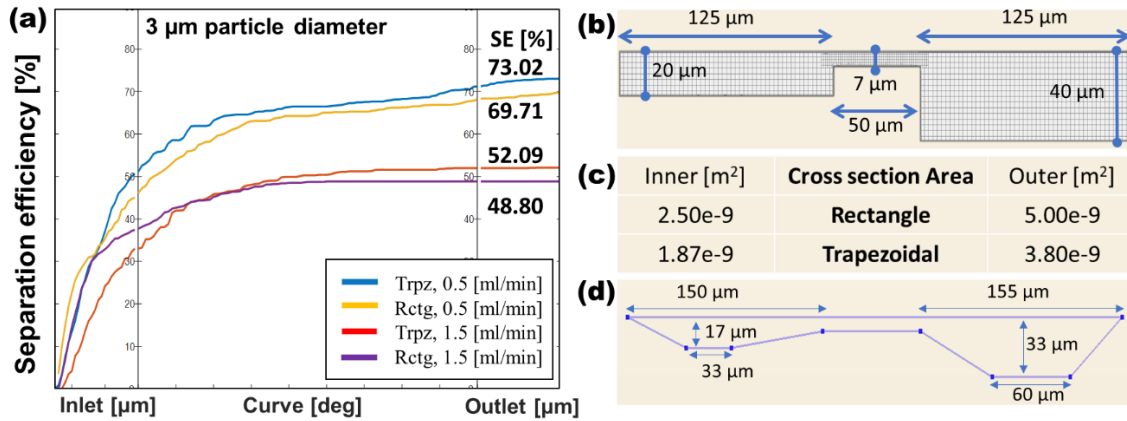


Figure 3-9 Separation efficiency graph in terms of position for channels with rectangular and trapezoidal cross sections

The graph for accumulated particle separation efficiency as a function of position inside the channel. Three separate segments represent the configuration of the device with a straight channel (left, where inlets are located at the beginning), curved channel (middle), and the other straight channel (right, where outlets are located at the end). The numbers written on the graph represent the final separation efficiency of each case. (b) Cross-section view of a rectangular bi-curvilinear model used in this study. (c) Area comparison between the two channel shapes in (b) and (d). (d) Cross-section view of a trapezoidal bi-curvilinear model, with identical dimensions to the channel in Figure 3-8

3.4.4 Injection angle

Secondary flow is a significant factor for particle migration in the microchannel. Tilted injection of fluids into the device is another way to generate secondary flow, in addition to using two parallel channels connected by a bridge as previously described. Injection channels are segments adjacent to the device that provide a pathway to deliver particle solution and sheath flow into the parallel channels. The injection angle is defined as the acute angle between the straight segment and injection channels. Thus, we studied how the inherent secondary flow resulting from tilted injection could affect particle migration and separation efficiency as a function of injection angle. Results reported in [Figure 3-10] were totally opposite to the expectation: separation efficiency is attenuated when the flows are injected at an angle both at high and low flow rates.

Reduction of particle separation efficiency was severe at high flow rates, irrespective of straight or tilted injection. However, the existence of tilted injection, irrespective of the angle, appears highly detrimental to particle separation efficiency.

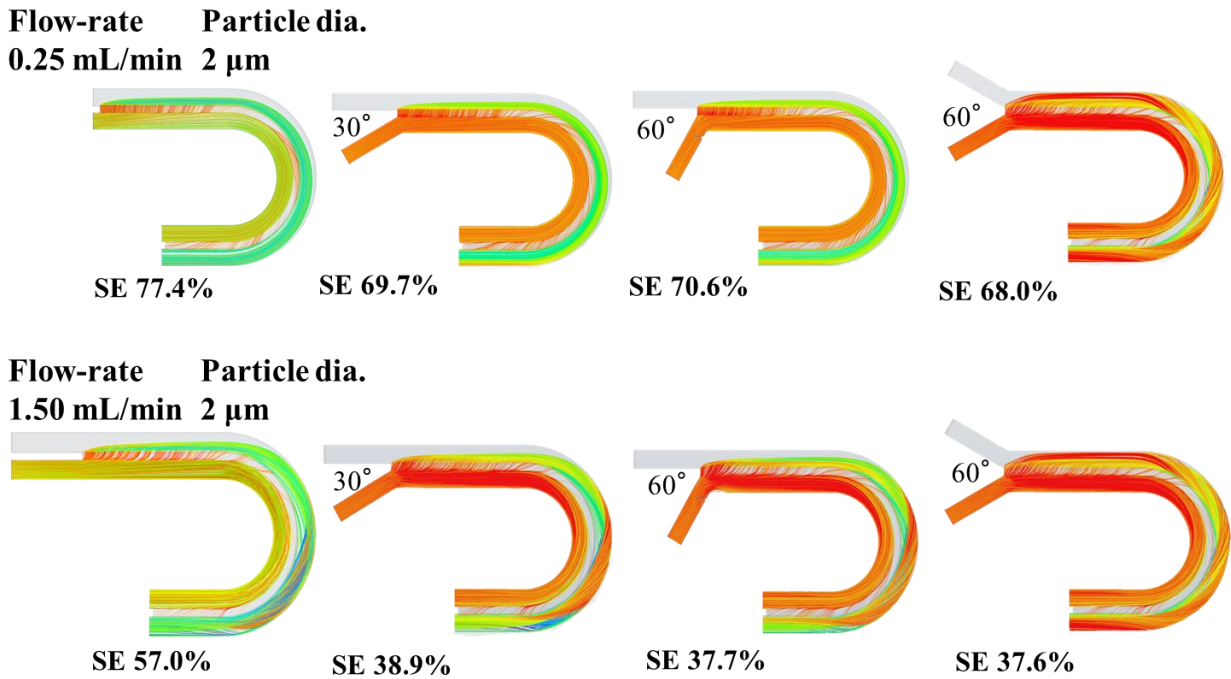


Figure 3-10 Separation efficiency for different injection angles

Injection angle is defined as the acute angle between the straight segment and the injection lane. Particles and sheath flow are injected into the device through injection lanes. Each colored line represents particle trajectories and their height. Red is near the top and blue is near the bottom.

3.4.5 Concentration of solutions

Particle concentration at the inlet could also impact separation efficiency and it was briefly investigated here. First, we look at previously reported RBC concentrations in experiments and simulations, as this is the most numerous blood cell type that can be transferred across the bridge.

The concentration of RBCs in human whole blood is typically 4×10^9 - 8×10^9 cells/ml, and previous simulation by Aashish[81] used a concentration of 1.68×10^4 - 1.68×10^6 cells/ml. Also, on the simulation conducted in this paper, 2 particles were injected into the inner channel every micro-second (2×10^6 particles/s), which, if flow-rate is assumed as 1 ml/min, corresponds to a concentration of 1.2×10^8 particles/ml. Thus, for testing the effect of particle concentration, two simplified simulations with different concentrations are conducted using a particle size of 2 μm and flow-rate of 1.5 ml/min. The first simulation with 8×10^7 particles/ml has 44.75% separation efficiency and a second one with 6.67×10^3 particles/ml has 48.83% efficiency. These results indicate that the diluted solution achieves higher separation efficiency.

However, notice that diluted solutions can be considered as Newtonian fluids but highly concentrated solutions such as blood are no longer Newtonian, and new models for viscosity such as the power-law model should be applied. All simulation model employed in this study is assumed as Newtonian behavior (constant dynamic viscosity). Also, if particles are too close, they start to interact with each other[82], so extra forces induced by each particle should be considered. Therefore, further study is needed to get a better and more realistic understanding of the effect of particle concentration in separation efficiency, especially at high particle concentrations.

3.4.6 Particle diameter

Size is one of the inherent characteristics of particles/cells. Many passive cell sorting systems rely on it, including this study. Working as a filtration architecture, the device in this study separates and sorts particles based on their size. Small particles (or RBCs) can easily pass through narrow bridges and migrate to the second lane of the channel, where sheath flow is supplied. However, large particles (or stiffer CTCs) cannot traverse the narrow channel and are retained in

the first lane where the particles are initially injected. This can be reproduced by simulations easily and the result is trivial [Figure 3-11 left]. However, this is not the only reason as to why and how this device is able to separate particles based on their size: large particles get lots of lift force compared to small particles. This phenomenon is clearly observed in the curved segment of the device and it affects particle migration and separation.

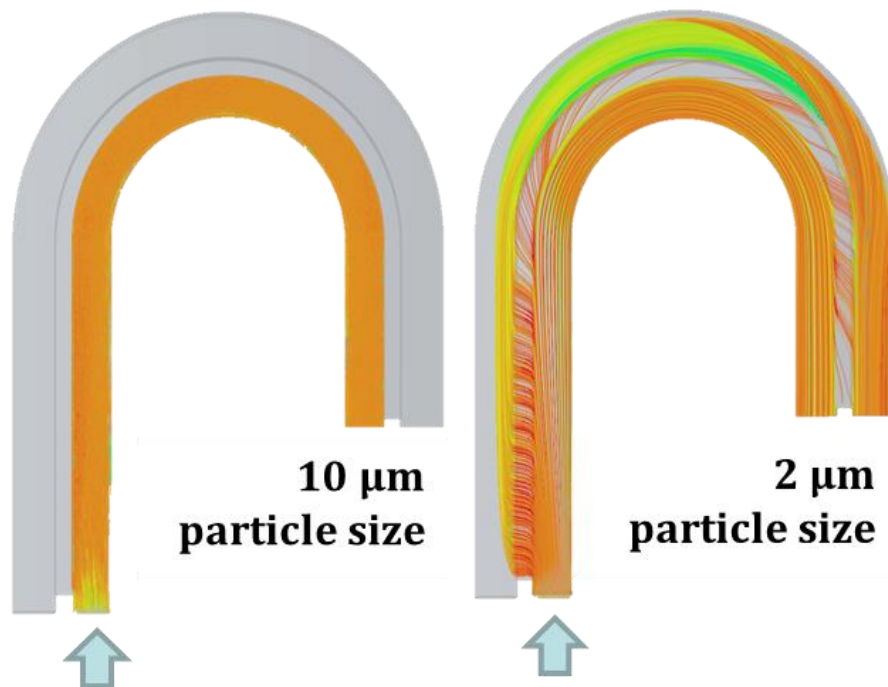


Figure 3-11 Filtration architecture : particle separation based on their size

The big particles are retained in the inner lane while small particles come out from both lanes at the outlet.

If particles are big, inertial focusing is observed in the inner lane of the curved segment. Notice that inertial focusing has been explained in terms of a force balance: a particle reaches an

equilibrium position and does not move in a certain secondary direction because the net force balance becomes zero in such direction [50]. However, our simulations might rebut this explanation: particles are actually moving and their net force does not become zero in the secondary direction. In what we called pseudo-inertial focusing, particles are actually rotating around a specific point and their circulation is so small that it looks like they have stopped moving in a secondary direction. Similar simulation results [Figure 2-11 (f)] have been published by Clime [69]. The mechanism for pseudo-inertial focusing is as follows [Figure 3-12 right lane]: (1) particles start at the mid plane of the inner lane near wall A and Dean flows from both the upper and lower halves of the cross section make the particles move from near wall A to the center of the channel. Secondary drag force toward wall B is the main force in this step. (2) Inertial lift force is not negligible compared to secondary drag force. Thus, particles cross the streamlines and move upwards in the upper half and downwards in the lower half. (3) As the particles go up (or down), their direction of motion is switched by the secondary Dean flow and now particles move toward wall A. (4) Particles go back to the starting point and the cycle repeats. If the loop described by the particles is large, it might look like a band under a microscope in an experiment. Also, it might look like inertial focusing if the loop described by the particles is small and closer to wall A. If the particle is small and it does not have enough inertial force, on the other hand, lift force would not be exerted on the particle. Then, these particles float following Dean vortices induced in the curved segment, as seen in [Figure 3-12 left lane].

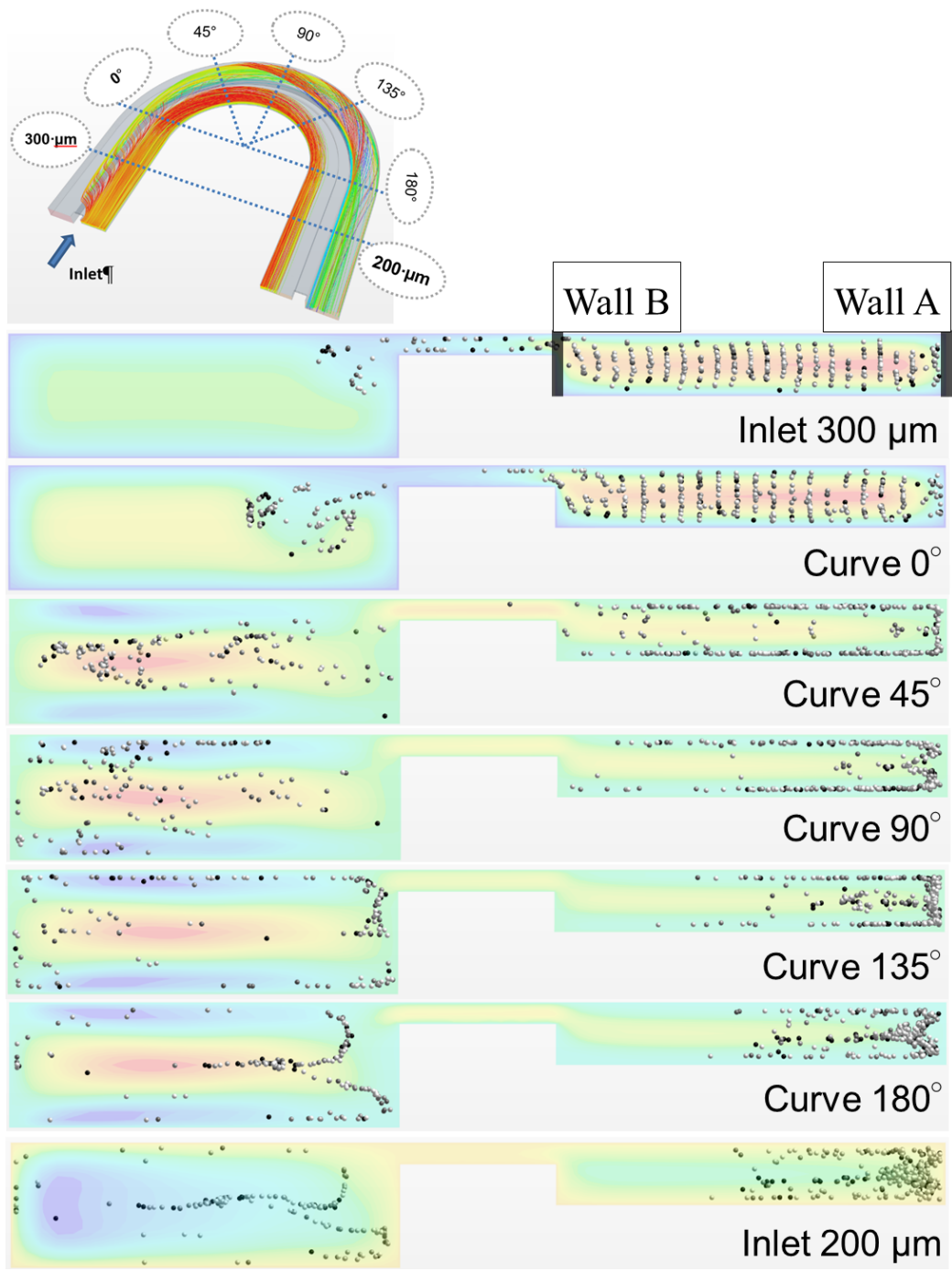


Figure 3-12 Mechanism for pseudo-inertial focusing

Cross section views along the curved segment of the channel as shown in the inset on top. Points represent accumulated particles passing the cross section and color-contour means outward (red, to the left) and inward (blue, to the right) radial velocity. Particles are focused in the inner lane away from the bridge while particles in outer lane are rotating in the entire channel. Its movie clip is attached as appendix S2. Compare it to movie clip appendix S3, rotating dominant case.

Then, why inertial focusing is observed only in the inner lane? This is related to their height. It can be explained by the R_f value, implying the ratio of shear-induced lift force to Dean drag force. Assuming that this channel is comprised of two separate rectangular channels, the R_f value is easily evaluated by [E2-39] using values of 3.5 μm for particle diameter, 582.5 μm and 717.5 μm for inner and outer lane's radius of curvature, respectively and hydraulic diameters of 34.5 for the inner lane and 60.6 for the outer lane. This yields R_f values of 0.3475 for the inner lane and 0.0790 for the outer lane. Both cases are in the Dean drag dominant region in which particles are rotating along vortices. The vertical lift force in the outer lane is too small and can be ignored, while the vertical lift force in the inner lane is relative large to be ignored. Simulation results by Clime [69] also demonstrate similar tendency in terms of R_f for behavior of particles in curved channels. Particles are entrenched in vortices and rotating in the entire channel at low R_f [Figure 2-11 (b)], while particles have their own rotating loop near the inner wall, smaller than a vortex in the channel, in moderate R_f [Figure 2-11 (f)].

Actually, this pseudo-inertial focusing attenuates separation efficiency by isolating small particles from the bridge and forfeiting their chances to cross it. It can be seen on [Figure 3-12] that particles are away from the bridge until the end of the channel. As particle size is increased, separation efficiency is decreased as seen in [Figure 3-13]. This tendency seems to be related to isolation of small particles. However, if this inertial focusing could be applied to large particles, such as CTCs, separation and enrichment of CTCs would be done more efficiently. Detailed design for such a device will be mentioned in the future work section.

Flow rate can also affect this pseudo-inertial focusing. Inertial focusing occurred at high flow rates because a higher flow rate generates stiffer shear in the fluid, resulting in higher lift force. The time for a particle to circulate in a vortex is different based on its size. So, if particles

of different sizes are injected at same position in a spiral channel, particles locate at different positions according to their size as they continue to rotate. Khoo's device [83] employ this mechanism for separating CTCs from RBCs.

[Figure 3-14] illustrates the place where particle migration occurs for different particle sizes. In the straight channel, the main driving force is secondary drag flow by pressure difference, so separation efficiency is essentially independent of particle size. However, as particles go into the curved segment, separation efficiency is different depending on their size. Inertial focusing is observed for particles $\geq 3.0 \mu\text{m}$, producing lower separation efficiencies. This is because inertial focusing near the inner wall limits the chance for particles to migrate.

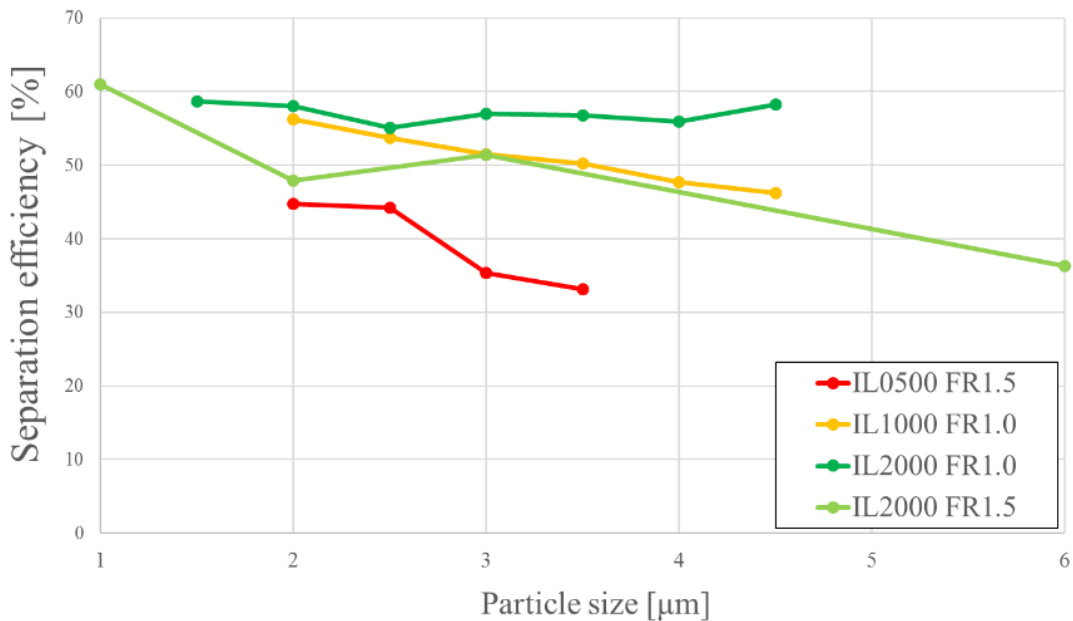


Figure 3-13 Separation efficiency in terms of particle size

There is tendency that separation efficiency is lower in the case of large particle than one of small particle. IL is inlet length, dimension of μm and FR is is flow-rate, dimension of ml/min

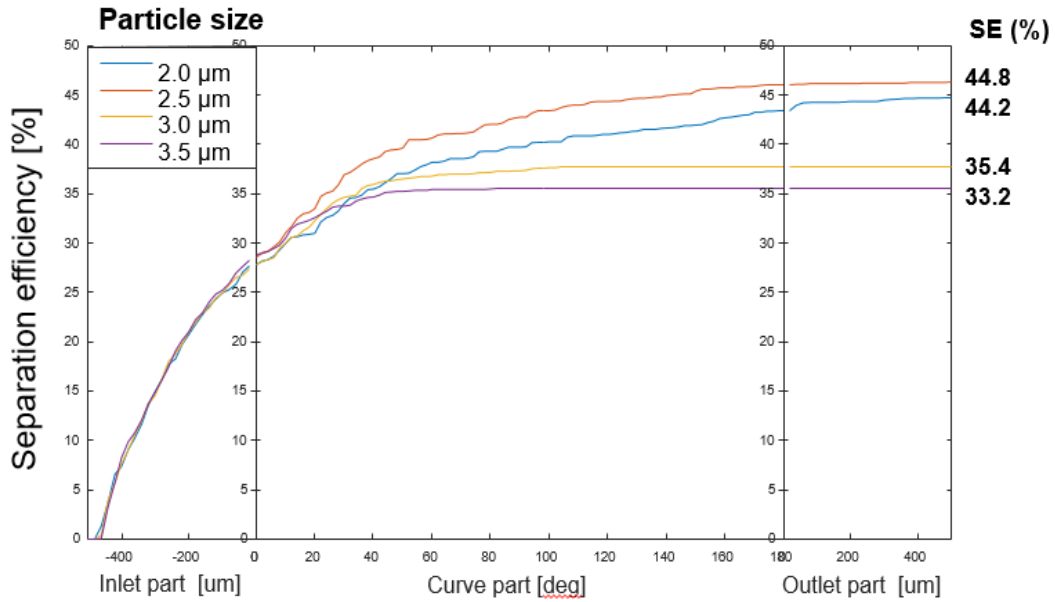


Figure 3-14 Separation efficient in terms of location for different particle sizes

The first segment of the graph refers to separation in the straight channel, where separation efficiency is independent of particle size because separation is done by filtration with hydrodynamic forces. Whereas, the second segment of the graph means that the curved part shows high dependence of particle size for separation efficiency.

3.4.7 Dimensionless pressure for device design

Priye [81] suggests a nondimensionalized pressure value defined in equation [E3-4].

$$\Delta P^* = \frac{\Delta P_{barrier}}{W} / \frac{\Delta P_{channel}}{IL} \sim \frac{\partial P}{\partial x} / \frac{\partial P}{\partial y} \quad [E3-4]$$

The pressure difference of the channel, $\Delta P_{channel}$, is the one between the beginning and the end of the straight inlet segment of length IL . The pressure difference of the barrier, $\Delta P_{barrier}$, is the difference of the pressure average between the straight lanes, and W is the length of the bridge. Thus, ΔP^* can be interpreted as a ratio of secondary pressure gradient to primary pressure gradient. Priye's simulation results demonstrate that separation efficiency is highly proportional to this newly defined pressure value (or simply "P value"). His simulation was conducted with different

shapes of channel cross sections and flow rate, as seen in [Figure 3-5] and [Figure 3-7]. The relationship between separation efficiency and P value for cases in the current study is presented in [Figure 3-15]. The linear tendency observed in [Figure 3-15 left] is obtained even though our results include simulations conducted with different inlet lengths and flow rate. If the regression is conducted only for selected data for 2 μm particle except long inlet length channel [Figure 3-15 right], R square is improved from 0.7 to 0.93. It means P value is a good indicator of separation efficiency for variant inlet length up to 2000 μm . P value, however, does not reflect the effect for inertial focusing of 3 μm particle and reverse flow of 5000 μm inlet length.

To consider the size of the particle, an additional term should be multiplied to P value. The best fitted term was an inverse of the square root of particle diameter divided by a characteristic length. Radius of curvature is one of the main candidates for this characteristic length, although further studies will be required. Figure 3-16 shows that separation efficiency as a function of a modified P value, defined in equation [E3-5], is well fitted to a line.

$$\Delta P^* = \frac{\Delta P_{barrier}}{W} / \frac{\Delta P_{channel}}{IL} / \sqrt{\frac{PD}{RC}} \quad [E3-5]$$

Here, PD stands for particle diameter and RC does for radius of curvature. This modified P value can be employed for finding optimized geometry parameters and operating conditions. Though it is not an exact value, these empirical relations could be a good guideline because particle simulation takes much more computational power than flow simulation. By employing P value estimation, proper conditions could be estimated briefly and it can save computational power. Furthermore, by figuring out the relationship between P value and geometric factors of the microchannel, an optimized design could be estimated without the need for simulations.

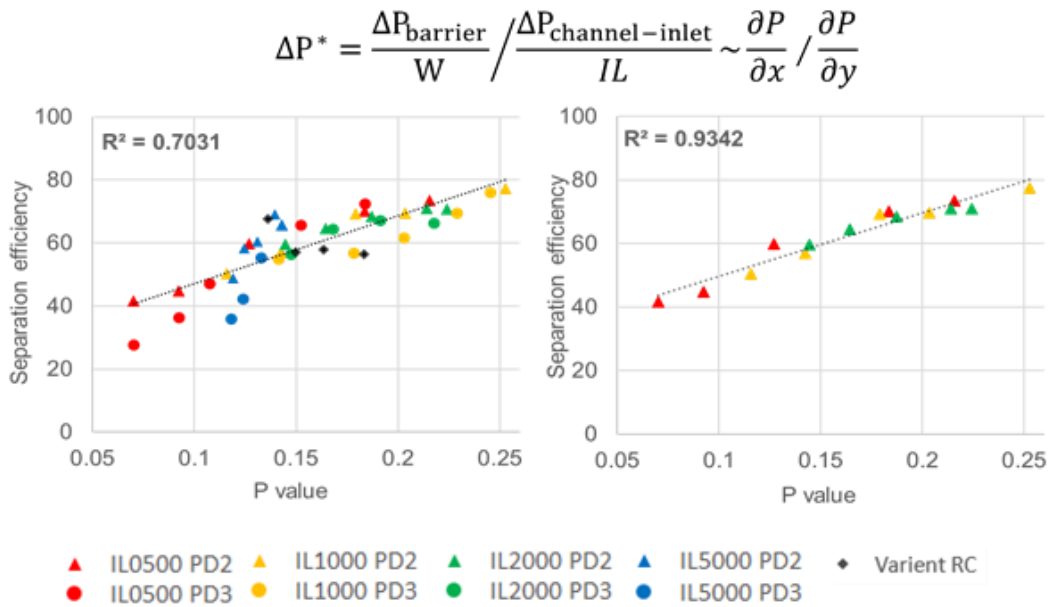


Figure 3-15 Separation efficiency as a function of normalized pressure defined by Priye for various simulation cases in this study

The graph (left) is for all data and one (right) is for selected results that has no inertial focusing and reverse flow.

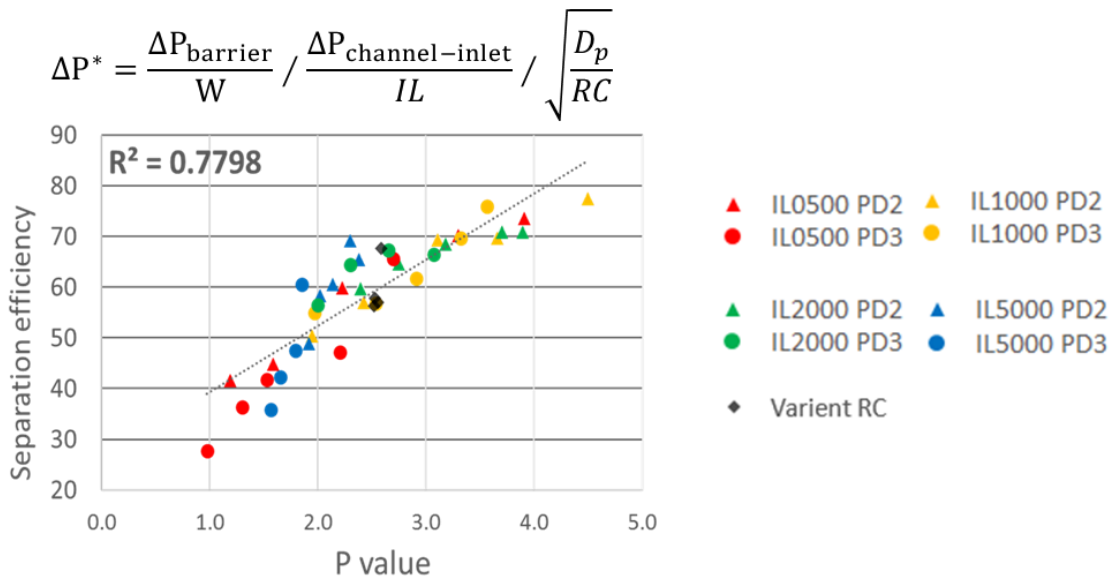


Figure 3-16 Separation efficiency as a function of a modified normalized pressure defined by equation [E3-5] for various simulation cases in this study

3.5 Conclusion

CFD/DEM simulations with thousands of particles were conducted using STAR-CCM+, allowing us to investigate the effect of a geometric and operational parameter such as inlet length, inlet flow rate, the shape of cross-section, injection angle, the concentration of the solution, and particle diameter quantitatively. Separation efficiency, the ratio of the number particles cross filter to the total number of particle injected, are evaluated through particle simulation. Performance of the microfluidic device could be assessed in terms of separation efficiency.

These simulations present lots of results against our conceptual expectation and enable us to understand the mechanism of particle separation in the microfluidic device exactly. A phenomenon that the amount of flow rate at outer lanes overtakes one of inner lane reminds us of the fact that particle separation results from medium transfer between curvilinear parallel lanes due to the pressure difference. Tilted injection and a curved segment on filtration part introduced to enhance separation efficiency are actually preventing particles from crossing the filter, attenuating its separation efficiency. Dean vortices are generated in the curved segment of the microfiltration device, taking particles away from the filtration bridge. Inertial focusing is also observed on a curved segment and concept of quasi-inertial focusing is introduced to explain this phenomenon. It is the reason that size of the particle and its corresponding inertia affects separation efficiency only at the curved segment. High throughput does not guarantee its separation performance because high flow rate yields low separation efficiency.

The simulation demonstrates that pressure drop/difference on the microfluidic device is directly related to separation efficiency, meaning that pressure difference between two parallel lanes is one of the main factors for particles to be separated. The effect of pressure is not fully comprehended, and future study should be continued. Since computational cost needed to conduct

3D CFD/DEM simulation is quite large, however, new simulation model, which require less computational power, is mandatory. In Chapter 4, a new simulation model to estimate pressure drop and flow distribution economically is suggested and verified by 3D CFD/DEM simulation. Also, experiments are conducted to support the computational result, and its results are compared with one of simulation in Chapter 5. Future 3D CFD/DEM simulation required is suggested in Chapter 6.

4. PRESSURE MODELING AND SIMULATION

4.1 Hagen-Poiseuille equation

Actuation of liquid flow is implemented by external syringe pump in this system. Not enough force may result in pump stalled. Also, as mentioned earlier in section 3.4.7, pressure difference between two curvilinear lanes is the key for particles to cross the bridge, resulting in particle separation. Thus, understanding of pressure distribution generated in the microchannel is essential to interpret the system.

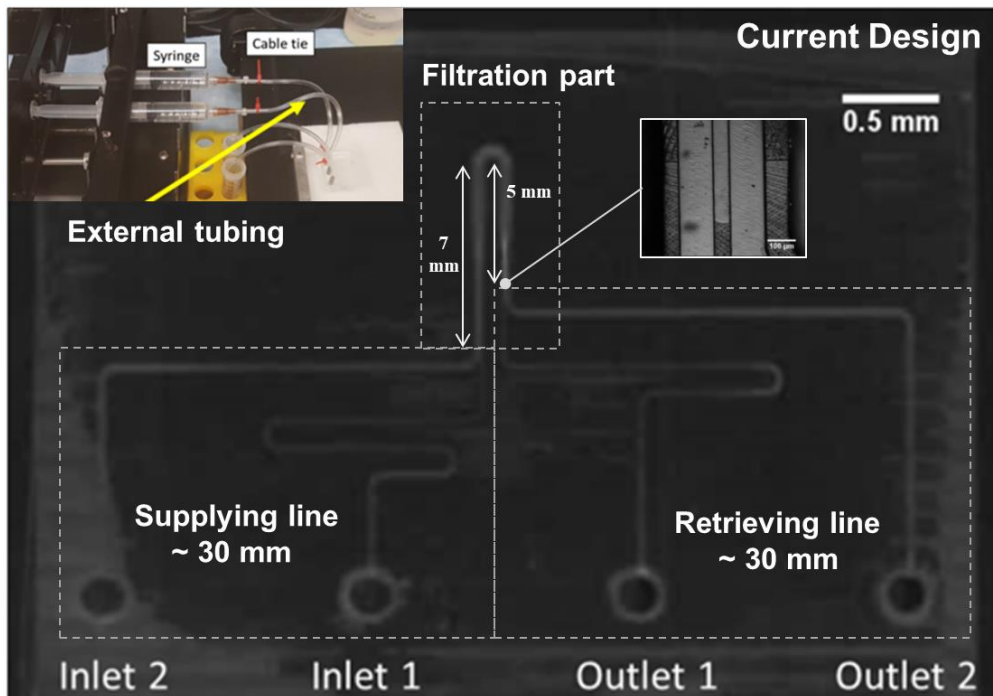


Figure 4-1 Configuration of current microchannel design

Image is taken by photocopy machine. Bright part is fluid path in the microchannel. Inset right-hand side is microscopic image for filtration part.

To estimate pressure distribution in the system, system should be divided. The flow system we have is comprised of three parts: (1) circular exterior tubing (OD 3 mm, ID 1.8 mm) from syringe to the microfluidic device, (2) rectangular internal supplying/retrieving lines connecting external tubing and filtration part, and (3) filtration part in microchannel where inner lane and outer lane is connected by the narrow bridge [Figure 4-1].

Fluid in this microfluidic scale is under laminar condition and satisfy continuum hypothesis. Assuming diluted particle solution are incompressible and has constant viscosity with respect to shear rate, referred as to Newtonian fluid, velocity profile and pressure distribution can be calculated analytically. Hagen-Poiseuille equation, representing relation between pressure drop required and flow-rate, can be achieved by integrating velocity profile over the cross section.

Exterior tubing has circular cross section. Pressure has linear decrement along the tubing. Total pressure drop can be easily calculated by Hagen-Poiseuille equation [E4-1]. [Figure 4-2] presents properties in circular external tubing. μ is dynamic viscosity, at 20 C° water has 0.001 [Pa*s]; L is the exterior tubing length, 40 cm of tubing is employed at each of the two inlets and outlets; Q is flow-rate, 0.1 ml/min is assumed, equivalent to 1.667×10^{-9} [m³/sec]; R is radius of tubing of 0.9 mm. So, the pressure-drop at tubing between syringe and microchannel becomes 2.58 [Pa], negligible amount compared to other value. Pressure drops at exterior tubing don't play a important role in the system

$$\Delta P = \frac{8\mu L Q}{\pi R^4} \quad [E4-1]$$

Internal supplying/retrieving lines has rectangular cross section. Pressure drop for rectangular channel can be evaluated by the equation below [E4-2] (Bahrami, et. al. *Proceeding of ICCM* (2005): p75109). Considering aspect ratio coefficient is not sensitive to aspect ratio (0.4217 to 1), height of channel is most sensitive (to the power of 3) factor in the system. Particle separation

in this system results from this feature of a rectangular microchannel. Pressure drop are dramatically changed by height. Assuming length of entrance-side supplying lines is 30 mm, width of channel is 125 μm , viscosity is 0.001 [Pa*s] and flow-rate is 0.1 [ml/min], pressure drops at supplying line for each height of 20, 30 and 40 μm channel yields 6.67, 2.09 and 0.94 bar [Figure 4-3]. Please note its high amount and huge difference. Pressure drop at retrieving line can be calculated similarly but flow-rate at retrieving line would be changed since transport of fluid exists between each lane at filtration part. Estimation of pressure and flow distribution in the filtration part should be proceeded. It can be done by either 3D computational simulation or circuit analogy model.

$$\Delta P = \frac{12\mu L Q}{WH^3 f(H/W)}, \quad f(H/W) = \left[1 - \sum_{n=1, \text{odd}}^{\infty} \frac{192}{\pi^5} \frac{H}{W} \frac{1}{n^5} \tanh\left(\frac{n\pi W}{2H}\right) \right] \quad [\text{E4-2}]$$

One of accurate method to estimate pressure drop and its distribution is conduct 3D computational fluid dynamics simulation. According to 3D computational fluid dynamics simulation conducted by STAR-CCM+ with specified geometry in [Figure 4-4], pressure drop along the channel and cross the channel becomes 0.61 and 0.08 bar, respectively at flow-rate 0.25 of ml/min [Figure 4-4, up] and does for 1.28 and 0.1 bar at flow-rate of 0.5 ml/min [Figure 4-4, down]. Also, we could get flow distribution in filtration part from computational simulation, essential for estimating pressure drop at retrieving line.

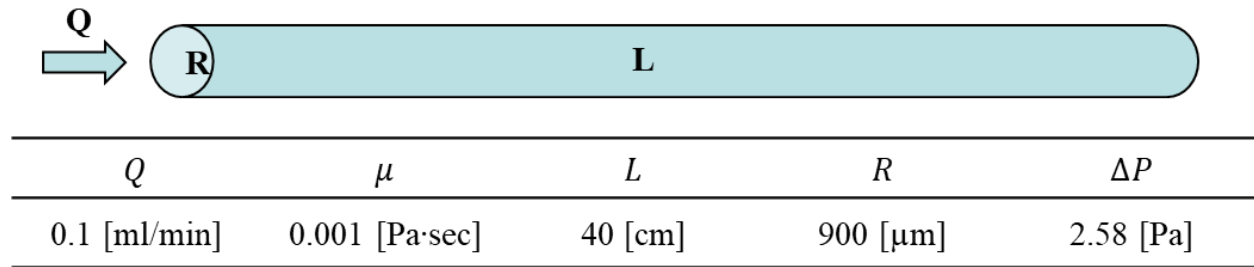


Figure 4-2 Schematic diagram for circular external tubing and pressure drop calculation

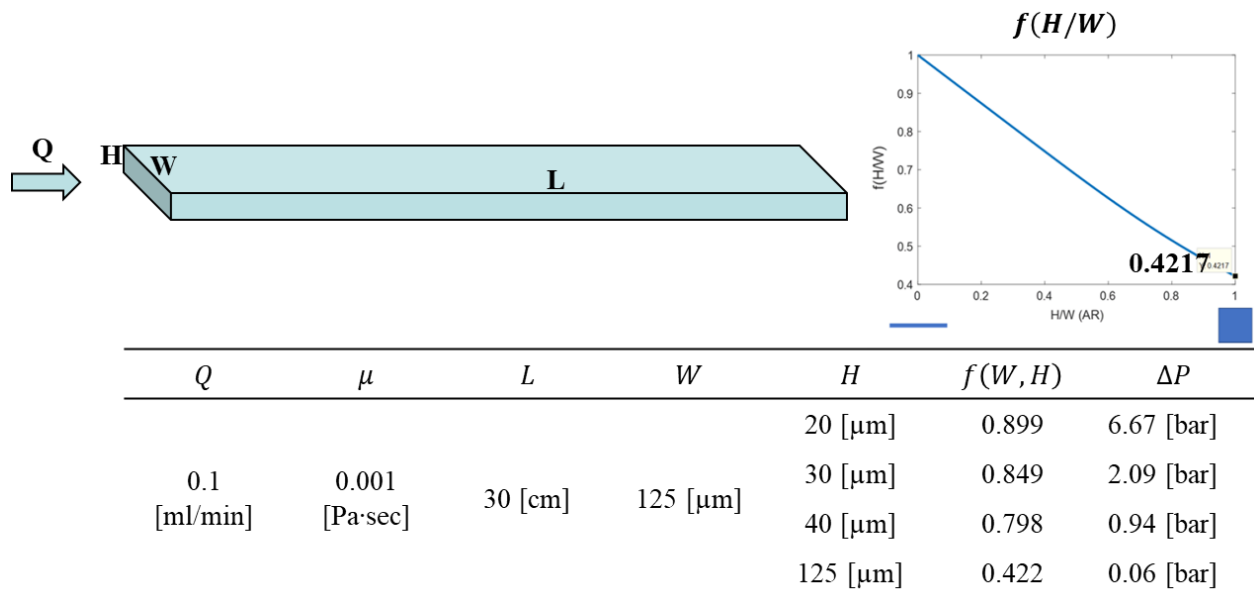


Figure 4-3 Schematic diagram for rectangular internal tubing and pressure calculation for different height

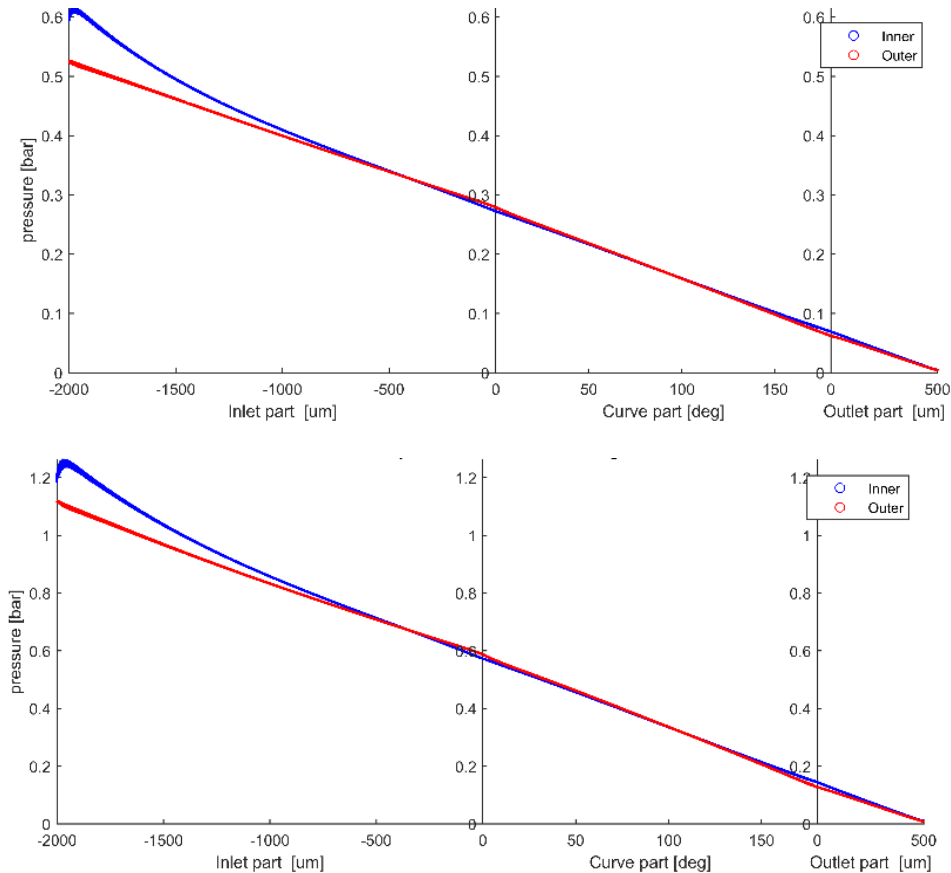


Figure 4-4 Pressure drop in the micro-filtration part, computed by STAR-CCM+

Geometries specified are inlet length of 2000 μm radius of curvature of 500 μm , outlet length of 500 μm , inner lane height of 20 μm , outer lane height of 40 μm . Upper one is the case at flow-rate of 0.25 ml/min and Lower one is the case at flow-rate of 0.5 ml/min.

4.2 Electric circuit analogy model for estimating pressure distribution

We can estimate quite accurate pressure distribution in the microchannel by 3D computational simulation. However, it takes at least an hour to build new dimension simulation file and run it, not adequate for finding optimized channel dimension. So, new simplified model to estimate pressure is necessary. Idea is derived from common explanation method for electric current, figuratively described as flow of water. This circuit model is started from reversing this idea. fluid flow in microchannel can be interpreted as a circuit model and flow-rate can be

described as electric current. Four strands of supplying/retrieving lines become resistance. Current can be interchanged at filtration part. Resistance of filtration part determine amount of current [Figure 4-5].

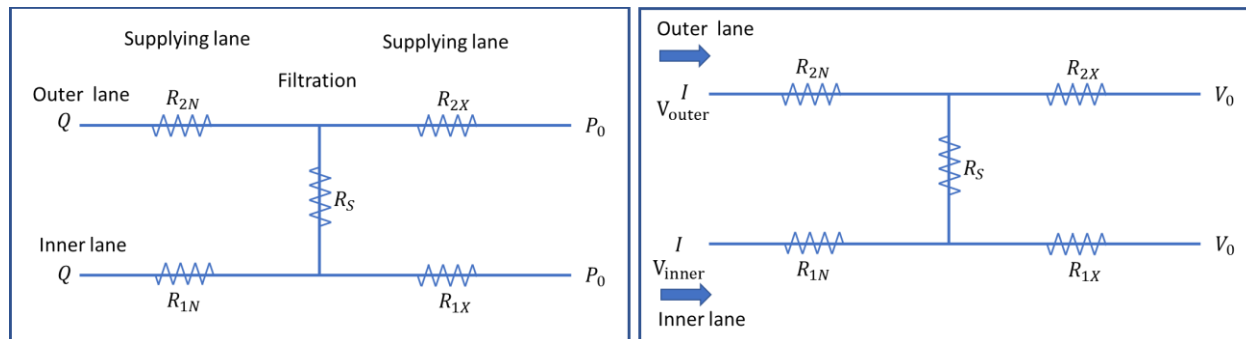


Figure 4-5 Simplest circuit model for microchannel design we have

Flow-rate Q , Pressure P and each part of microchannel (R') are corresponding to current (I), voltage (V) and resistance (R), respectively.

Since base voltages and current is given value, if we know resistant value, peak voltages can be calculated. Equation for resistance [E4-4] can be derived from comparison between Equation for Ohm's Law [E4-3] and Hagen-Poiseuille equation [E4-2]. Then, peak voltage, meaning required pressure at syringe pump could be evaluated. One of our goals is to increase flow-rate through the bridge, resulting in higher enrichment. If the pressure difference between inner and outer lanes is zero at the end of the bridge, pressure drop along supplying lane from end of the bridge to the tubing will be the same. Then, the flow-rate ratio is reversely related to resistance ratio for the same pressure drop. In our case, the only difference is the height of the lane, sensitive term to resistance of the channel, red colored term in the equation. So, resistance ratio of inner lane

($H = 20$, $f(20/125) = 0.9$) to outer lane ($H = 40$, $f(40/125) = 0.8$) will be 7.1:1. It is highly reversely related to flow-rate ratio of ~1:6.8 from both experiment and simulation

$$\Delta V = [R] I \quad [E4-3]$$

$$\Delta P = \left[\frac{12\mu L}{WH^3 f(H/W)} \right] Q \quad [E4-2]$$

$$R = \frac{12\mu L}{WH^3 f(H/W)} \quad [E4-4]$$

where, V is voltage, R is resistance, I is current, P is pressure, μ is dynamic viscosity, L is length of unit resistance segment. Direction toward flowing direction is considered as L. For example, L of bridge should be distance between inner and outer lane because flow in bridge part are from one lane to the other lane. W is width of unit resistance segment and H is height of unit resistance segment. directions of W and H are determined as perpendicular to L direction and value of W should be larger than one of H.

This simplest circuit model brings out result within a second and it will help us to estimate required pressure drop at syringe pump. However, it cannot reflect complex shape of the channel like our U-shape filtration part. So, more improved model should be established by dividing target part into several elements. [Figure 4-6] demonstrates sliced U-type filtration part. Each section has different geometric value and this fine difference of each section generates characteristics of the channel. For example. inner and outer lane of curved section has different radius of curvature and corresponding length, making different resistance and reverse flow at beginning and end of the curved section.

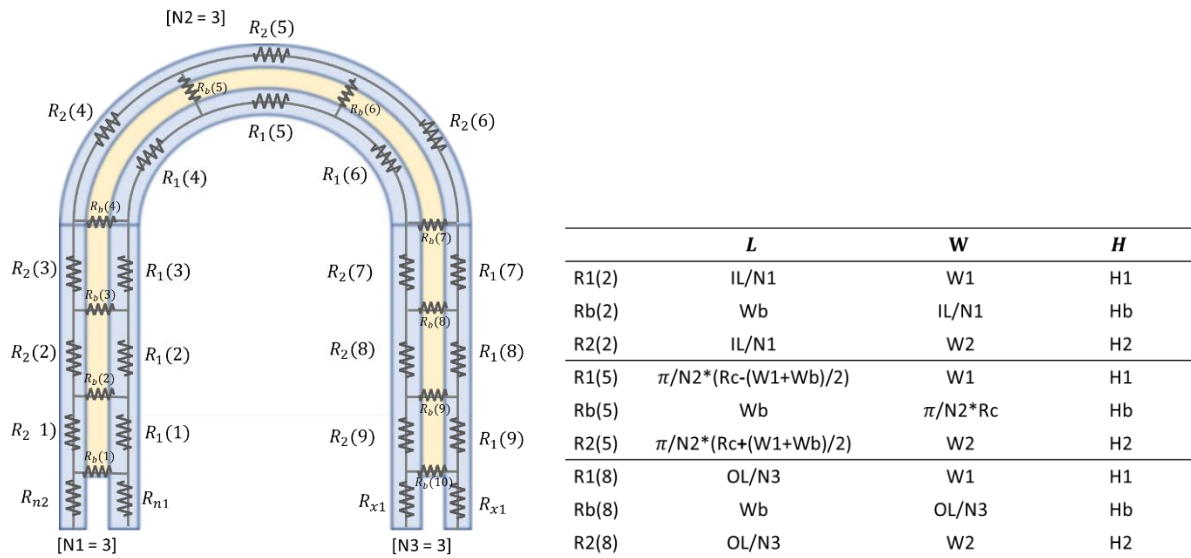


Figure 4-6 Improved circuit model for U-type channel

Sliced section for U-type filtration part (Left) and geometric value for each section and corresponding resistance value (right).

To validate this circuit model, pressure distribution is calculated by circuit model and compared to result from STAR-CCM+ simulation [Figure 4-7 and Figure 4-8]. Outer lane pressure profile is almost similar between two simulation models. Furthermore, circuit theory can represent not only reverse pressure itself, but its location and amount are similar compared to simulation result by STAR-CCM+. However, pressure value estimated by circuit model diverged at the beginning of filtration part while pressure value calculated by STAR-CCM+ tend to converge to inner lane pressure. Considering its small calculation time (within 1 seconds), circuit model is worthwhile to do.

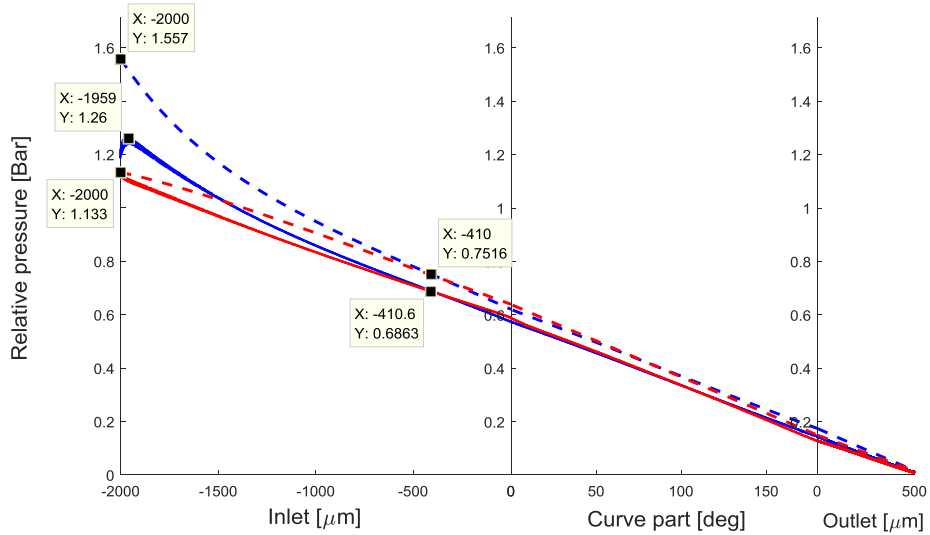


Figure 4-7 Pressure distribution comparison 1

Model for the channel with 2000 μm inlet length, flow-rate of 0.5 ml/min, radius of curvature of 500 μm . Solid line is data from STAR-CCM+ simulation and dashed line is a result from circuit theory. Blue refers pressure distribution for inner lane and Red does for outer lane. Circuit model: pressure drop along channel is 1.557 bar and across channel is 0.424 bar. Length up to point pressure converged is 1590 μm and width of channel is 300 μm . Then, P value yields 1.44. STAR-CCM+ 3D model: pressure drop along channel is 1.26 bar and across channel is 0.133 bar. Length up to point pressure converged is near 1590 μm and width of channel is 300 μm .

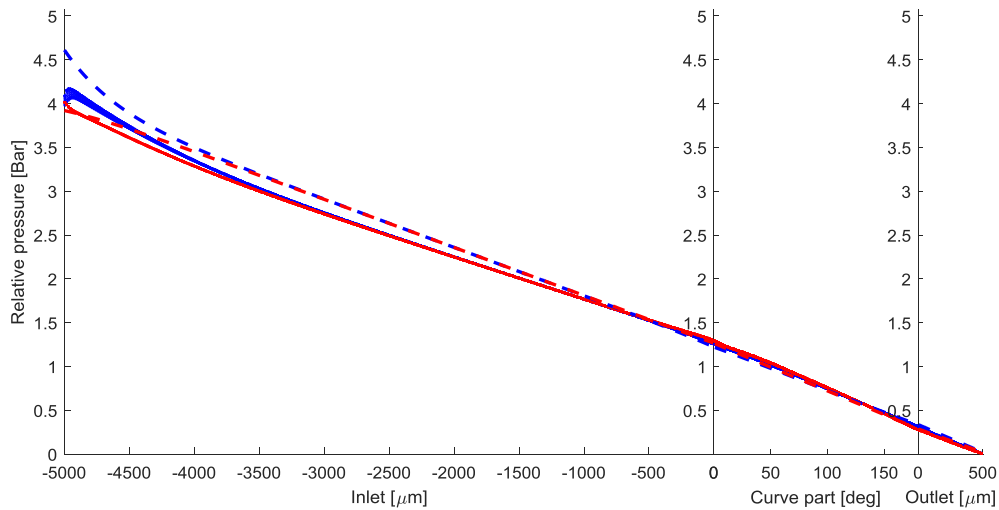


Figure 4-8 Pressure distribution comparison 2

Model for the channel with 5000 μm inlet length, flow-rate of 1.0 ml/min, radius of curvature of 500 μm . Solid line is data from STAR-CCM+ simulation and dashed line is a result from circuit theory. Blue refers pressure distribution for inner lane and Red does for outer lane.

4.3 Conclusion

Using circuit analogy model developed and verified at previous section, current pressure distribution is investigated. [Figure 4-9] presents pressure distribution at current microchannel under given condition, showing its design has problems. The microchannel inside is comprised of supplying line, retrieving line and filtration line [Figure 4-1]. Geometric parameter of filtration part is not changed a lot compared to previous research [Figure 2-5][10] but it has huge different at supplying/retrieving lines. Previous design has supplying/retrieving with mm-scale length while current design does with cm-scale length. It consumes extra pressure on the microchannel and increase chance for microchannel to be broken by high pressure. Assuming flow-rate at 0.5 ml/min, circuit theory method estimates 46.67 bar and 17.68 bar for fluid to run flow at each inner and outer lane of current design channel, respectively [Figure 4-9]. Pressure drop generated by inner and outer supplying/retrieving lines accounts for 89 and 73 % of total pressure drop occurred at inner lines, respectively. Though there is no exact report or experiment that bonding method used here can endure high pressure not to be broken, it is too high-pressure intuitively. However, maximum pressure loaded on the previous channel was around 20 bars at flow-rate of 1.0 ml/min [Figure 4-10] and pressure consumed by supplying/retrieving lines account for only 30 % of total pressure drops. It means that a lot of pressure is wasted not to improve separation efficiency.

Besides excessive pressure-drop on supplying lines, there is the other problem. Pressure drop is not well distributed along the microchannel. Maximum pressure 0.35 bar difference between inner and outer lane along the channel and they are converged rapidly around 1500 μm from the entrance, meaning there is no particle and flow transfer during remaining 10000 μm . Even worse, more than 3 bars are wasted even during filtration part. Considering limitation of bonding strength

(~7 bar), it cannot be neglected. New design should be suggested to reduce pressure requirement and to distribute it well. It will be explained in the section 6.2.

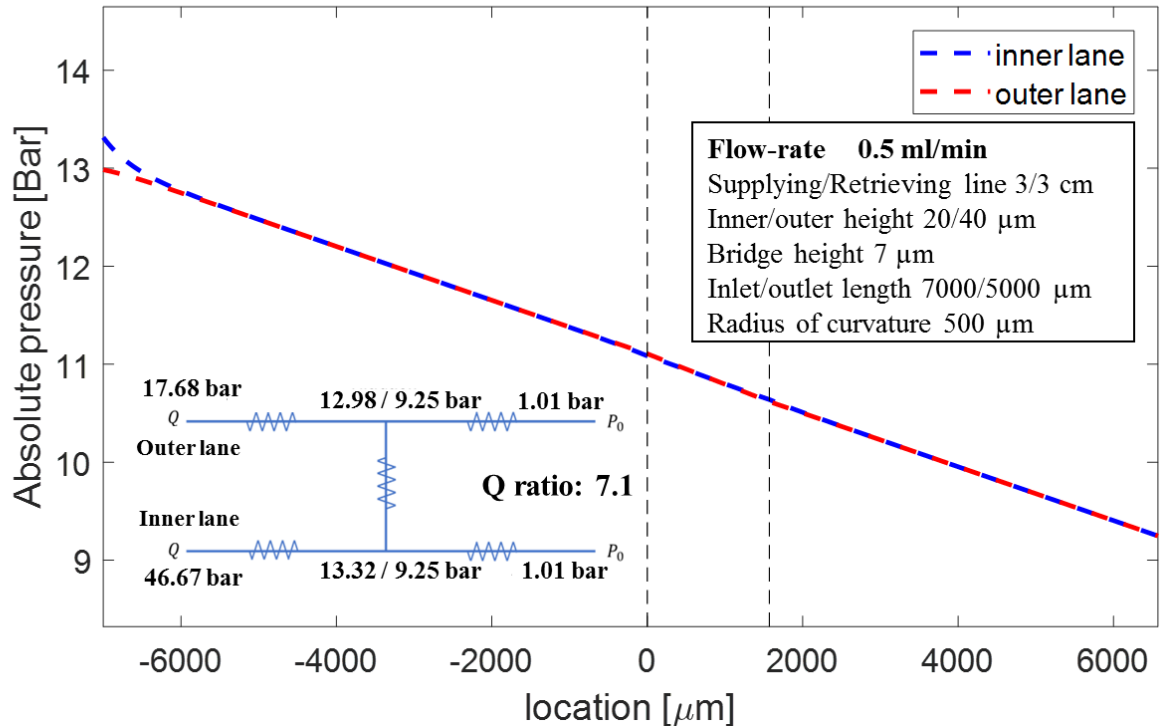


Figure 4-9 Pressure distribution at filtration part for current device and system

Flow-rate at 0.5 ml/min. 0 at location is beginning of the curved segment on U-type filtration part. Maximum pressure difference is 0.35 bar at the beginning of the filtration part. Converged at 2025 μm from the beginning of the filtration part. Width of channel is 300 μm . Pressure drop along the channel is 4.084 bar.

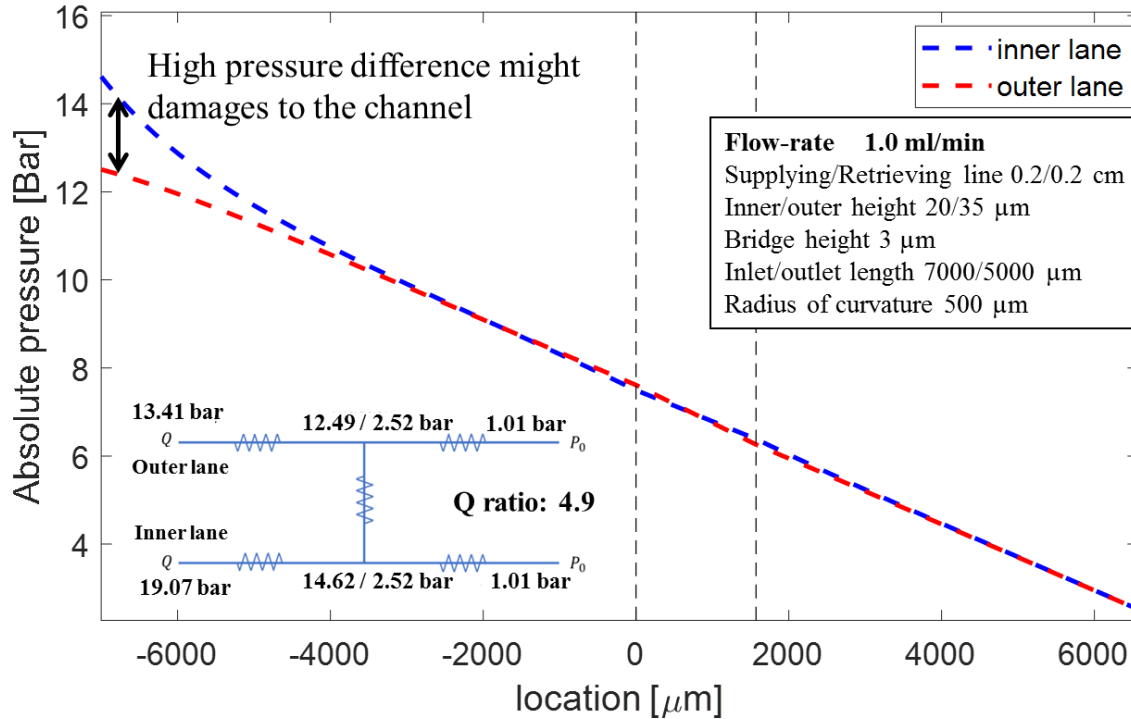


Figure 4-10 Pressure distribution at filtration part for previous device and system

Flow-rate at 1.0 ml/min. 0 at location is beginning of the curved segment on U-type filtration part.

By using circuit analogy models, we can estimate minimum pressure required for fluid to flow. If pressure is not supplied enough, pump will be stalled automatically even though channel is not closed-off. Operation curve can be prepared by circuit analogy model before conducting experiment and give a guidance for an experiment. [Figure 4-11] represent minimum pressure requirement in terms of flow-rate injected into the microchannel. Maximum pressure supplied to the microchannel is determined by combination of force generated by syringe pump and cross-section of syringe. If double syringe is installed at one syringe pump, its area of cross section will be double, yielding decrement of maximum pressure supplement. Each dashed line shows maximum pressure supply at each combination. According to the operation curve, maximum

possible flow-rate with plastic 10 ml syringe would be 0.1 ml/min, which was quite low flow-rate as we expect. It can be solved by substituting syringe with smaller area of cross-section.

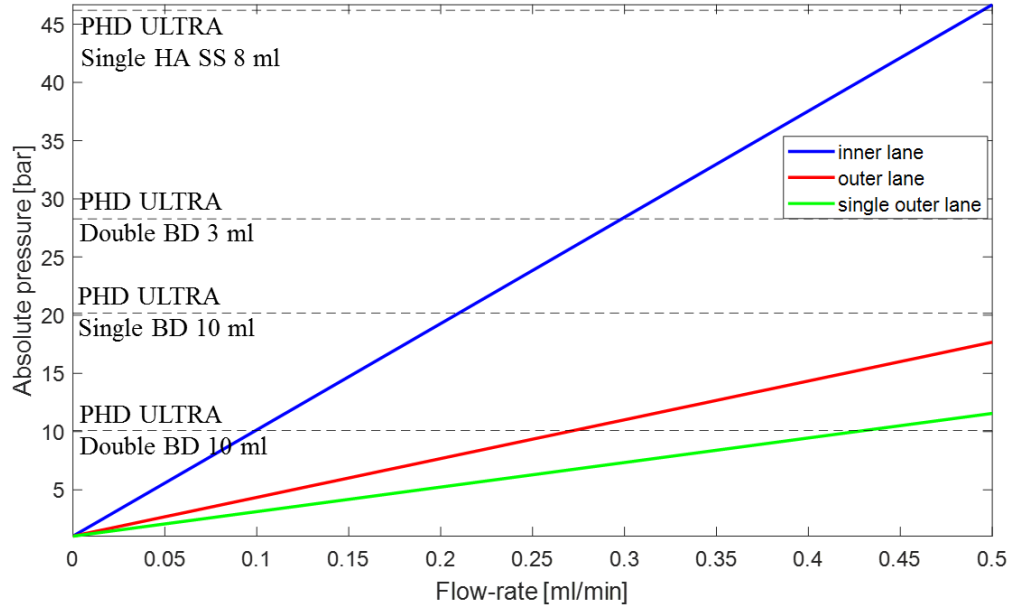


Figure 4-11 Operation curve for this system in terms of flow-rate

Blue line is minimum pressure requirement of inner lanes at specific flow-rate while Red line is minimum pressure requirement of outer lanes. Green lines are one for the case that inner lane is totally closed-off and thus only outer lane is employed. Its geometric parameters follow current design, seen at Table 6-2.

5. EXPERIMENT

5.1 Fabrication of the channel

Fabrication of microfluidic device was conducted by Design 1 Solutions, LLC [Figure 5-1]. Channel body and cover are made of thermoplastic, cyclo-olefin polymer (COP). Fluid pattern is physically micro-milled on channel body and the cover plate is combined on the body. Specification of the milling machine employed is not disclosed from the company. All geometrical dimension of fluid pattern they have are similar as mentioned in simulation. Internal structure of channel has supplying lines part and filtration part. Supplying lines part are connecting inlet/outlet to filtration part. Filtration part is comprised of two parallel U-type lanes connected by narrow bridge. It has 7 mm straight segment, 500 μm radius curve segment and 5 mm straight segment. Inner lane and related supplying line has 125 μm width and 30 μm height and outer lane and related supplying line has 125 μm width and 40 μm height. (Prototype channel has 20 μm height in their inner lane). According to given information average, minimum and maximum bridge height measured before bonding is 4.36, 2.8 and 7 μm , respectively. Bridge of height is not controlled well due to resolution problem of drill. Width of bridge is 50 μm . 15Ga blunt needle are installed to all inlets and outlets. Various kind of bonding methods: dry adhesive, dry adhesive tape, UV adhesive and solvent bonding. Pressure to push during bonding process varies each channel and light are exposed to the channel by lamp or UV light. Also, some of channel, usually employing UV adhesive, has silicon gasket inside of the channel and extra groove for gasket. Besides bonding methods, other settings are tried to keep constant. Several prototype channels were placed ordered first, then, additional 3 batch and 51 new channels (A batch 18 [Table 5-2], B batch 15 [

Table 5-3], C batch 19 [Table 5-4]) are placed ordered again. See [Table 5-2 - Table 5-4] for detail information of each channel. Information for prototype channel was not offered from the company.

Table 5-1 Summaries of microchannel fabrication for previous and current one

	Material	Patterning	Bonding	Price & Time
Previous	PLA Poly(lactic acid)	proteinase K / BSA etching	Heating (80 C° for 20 min)	< 24 hour < 10 \$
Current	COP (COC) Cyclic olefin (co)polymer	Micro-milling	Dry adhesive UV adhesive Solvent bonding	> 1 month ~ \$ 300

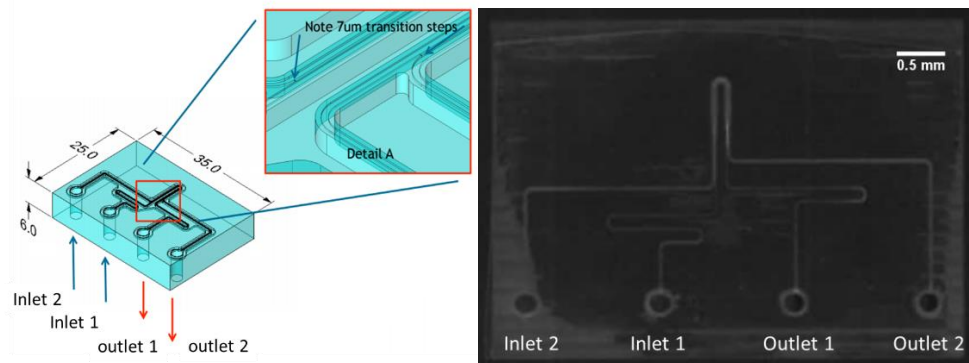


Figure 5-1 Channel for experiment by Design 1 Solution, LLC; lengths are given in millimeters

Left, Schematic diagram for the channel. Right, Image of overall fluid path pattern obtained by planner scanner. White line on the image represent micro-milled fluid path (lane) inside of the channel.

Table 5-2 Information for A batch channel

Dry adhesive, solvent bonding and UV adhesive is employed for bonding methods. Intensity and wave length of light exposed to the channel is not disclosed. A13 is lost, only water injection test was conducted. So, image investigation is not conducted for A13.

Names	Bonding methods	Product name	Pre-gap [μm]	Gasket	Light	Pressure [psi]	Time
A1	Dry	ARD-93319	4.0	NA		Pressure	60
A2	Solvent	Isopropyl alcohol	3.8	NA	Lamp		90+90+90
A3	Solvent	Isopropyl alcohol	3.6	NA	Lamp		90+90+90
A4	Dry	ARD-93319	3.8	NA		Pressure	
A5	Dry	ARD-93319	4.1	NA		Pressure	
A6	Dry	ARD-93319	3.2	NA		Pressure	
A7	Dry	ARD-93319	3.6	NA		Pressure	
A8	Solvent	Isopropyl alcohol	3.9	NA	Lamp		90+90+90
A9	Dry	ARD-93319	4.2	NA		Pressure	
A10	Solvent	Isopropyl alcohol	5.6	NA	Lamp		90+90+90
A11	Solvent	Isopropyl alcohol	2.9	NA	Lamp		90+90+90
A12	Solvent	Isopropyl alcohol	2.9	NA	Lamp		90+90+90
A13	UV	DMX	5.5	Yes	Lamp		40
A14	UV	L-THK	5.5	NO	LED		40
A15	UV	L-THN	5.1	Yes	LED		40
A16	UV	DMX	4.5	Yes	LED+Lamp		20+20
A17	UV	DMX	5.7	No	Lamp		40
A18	UV	L-THN	3.9	No	LED		40

Table 5-3 Information for B batch channel

Intensity and wave length of light exposed to the channel is not disclosed. There is no information for temperature control.

Names	Bonding methods	Product name	Pre-gap [μm]	Gasket	Light Curing time [sec]	Pressure [psi]	Time
B1	Solvent	Isopropyl alcohol	3.5	No	UV lamp	10	90+90
B2	Solvent	Isopropyl alcohol	4.6	No	UV lamp	10	90+60
B3	Solvent	Isopropyl alcohol	3.7	No	UV lamp	10	90+30
B4	Solvent	Isopropyl alcohol	4.4	No	UV lamp	15	90+90
B5	Solvent	Isopropyl alcohol	5.9	No	UV lamp	15	90+60
B6	Solvent	Isopropyl alcohol	3.3	No	UV lamp	15	90+30
B7	Solvent	Isopropyl alcohol	5.3	No	UV lamp	20	90
B8	Solvent	Isopropyl alcohol	3.6	No	UV lamp	20	60
B9	Solvent	Isopropyl alcohol	4.2	No	UV lamp	15	90
B10	Solvent	Isopropyl alcohol	3.6	No	UV lamp	15	90
B11	Solvent	Isopropyl alcohol	4.4	No	UV lamp	15	90+30
B12	Solvent	Isopropyl alcohol	5.3	No	UV lamp	15	60+30
B13	Solvent	Isopropyl alcohol	3.1	No	UV lamp	15	60+60
B14	Solvent	Isopropyl alcohol	4.1	No	UV lamp	15	60
B15	Adhesive tape	(PP film) 3M 9795r	3.8	No		10	60

Table 5-4 Information for C batch channel

Company did not send us C11 and C12 channel.

Names	Bonding methods	Product name	Pre-gap [μm]	Gasket	Light	Pressure [psi]	Time
C1	Solvent	Ethynol	6.5	Clear	Lamp	10	90+90+90
C2	UV	Si5056	5.3	Clear	Lamp	10	60+20
C3	Solvent	Ethynol	3.9	Red	Lamp	10	90+90+90
C4	UV	Si5056	6.0	Red	Lamp	10	60+20
C5	Solvent	Ethynol	3.0	Red	Lamp	10	90+90+90
C6	Solvent	Ethynol	5.6	Red	Lamp	10	90+90+90
C7	Solvent	Ethynol	4.9	Clear	Lamp	10	90+90+90
C8	Solvent	Ethynol	5.1	Clear	Lamp	10	90+90+90
C9	UV	Si5056	4.5	Clear	Lamp	10	60+20
C10	UV	Si5056	6.5	Red	Lamp	10	60+20
C13	UV	Si5056	4.0	Red	Lamp	10	60+20
C14	UV	Si5056	3.9	Red	Lamp	10	90+20
C15	Solvent	Ethynol	4.9	Red	Lamp	5	90+90+90
C16	Solvent	Ethynol	3.3	Clear	Lamp	5	90+90+90
C17	Solvent	Ethynol	4.0	Clear	Lamp	5	60+60
C18	Solvent	Ethynol	2.8	Red	Lamp	5	60+60
C19	Solvent	Ethynol	7.0	Red	Lamp	5	90
C20	Solvent	Ethynol	3.2	Red	Lamp	5	90
C21	Solvent	Ethynol	4.2	Red	Lamp	5	90

5.2 Particle separation test

5.2.1 Configuration of particle separation test

Two plastic syringes of 10 ml (BD) are connected to inner and outer inlet of microchannel by plastic tubing (OD 1/8'' ID 1/16'' ND-100-65). 15Ga blunt needle with Luer lock is employed to connect syringe to the microchannel. Cable tie or metal clamp fasten tubing with installed 15Ga blunt needle to prevent water leakage at tubing-needle connection. Inner lane syringe is filled with diluted 2 μm and 10 μm fluorescent particles solution (Fluoresbrite® YG Carboxylate Microspheres) and outer lane syringe does with DI water as sheath flow. Two syringes are pushed by syringe pump (50 lbf max, PHD 2200, Harvard Apparatus) at same flow-rate. Outlet flow is collected at tube [Figure 5-2].

Original intend for this test is for measuring fluid volume collected at each outlet as a result of water injection and their concentration. Then, it can be compared with computational simulation. Most of test set, however, are representing problems before collecting water. Pump is unintentionally stalled, solution was leaking at tubing, edge between channel body and cover.

For testing prototype-batch and A-batch channels, we could get only a few reasonable data, which can be compared with simulation result. So, next two section is focused on how to evaluate concentration of solution collected at each outlet. And, then, defects observed during the test are investigated.

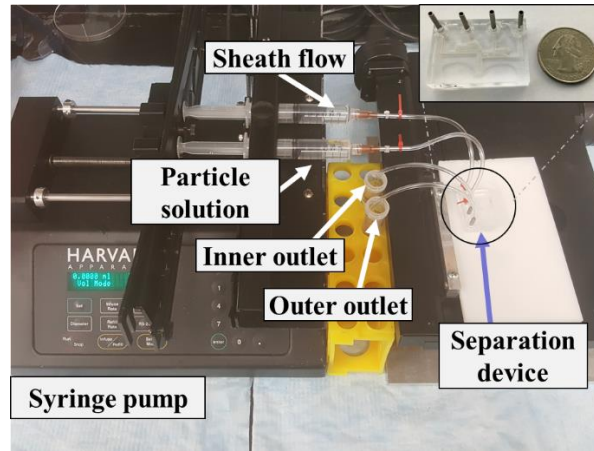


Figure 5-2 Configuration of particle separation test

Particle solution and sheath flow are injected into the microchannel through inner and outer entrance by syringe pump. Cable tie is employed to fasten tubing to metal tips of both syringe and the microchannel

5.2.2 Counting number of particles in the sample

Particle separation was successfully conducted using one of prototype channel. TC20™ Automated Cell Counter, BIORAD is employed to take a picture of solution [Figure 5-3]. Thus, images taken with the cell counter are then analyzed using *ImageJ* to count small particles on them. A threshold of 110 out of 256 in intensity units is specified to produce a binary image [Figure 5-5 upper left]. The built-in function, ‘*analyze particle*’, is employed to count particles. Each particle size has a different average area measured in pixel square (pix^2). Notice that some particles are actually aggregates and look like a bigger particle, red dots in [Figure 5-5 lower left], so the areas identified as possible particles should be scaled based on their size and circularity [Figure 5-5, Right]. Reference particles of 2, 3, 6, 10, 20 μm were employed to figure out the correlation obtained in [Figure 5-4].

After these analysis, the number of particles at inner-outlet and outer-outlet for [Figure 5-5 lower right] yields 23480 and 7805. Notices that is a kinds of concentration quantity which mean how many particles exist in specific volume. The result acquired at computational simulation,

however, was particle-rate base which mean how many particles are gathered at specific time. So, the unit should be converted to compare experimental result to simulation results.

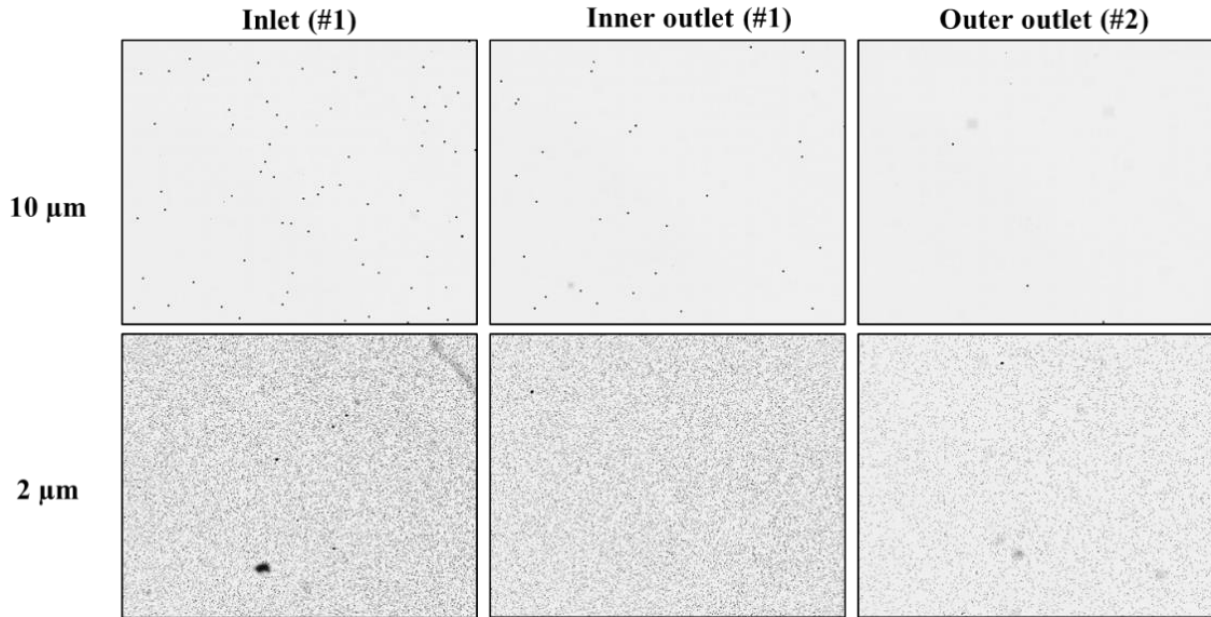


Figure 5-3 Picture by particle counting machine.

The device with height difference of 20 μm between lanes is employed (H2O). Upper picture represents particles separation for 10 μm particle diameter while lower pictures shows particle separation for particle diameter of 2 μm. Inlet flowrate is 0.5 ml/min in both case.

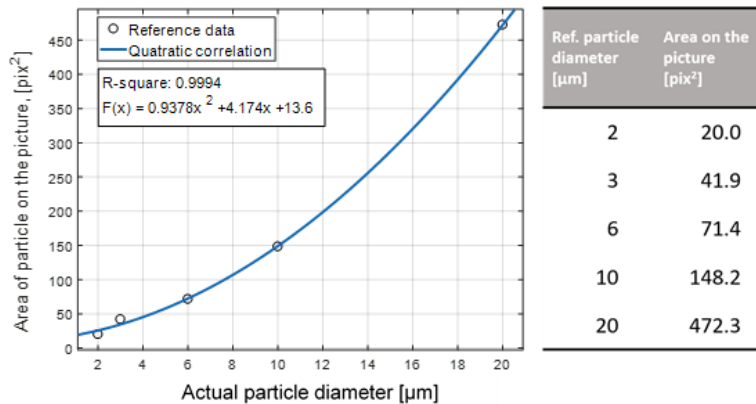


Figure 5-4 Correlation between actual particle size and area on the picture

Reference data (right) and its correlation (left).

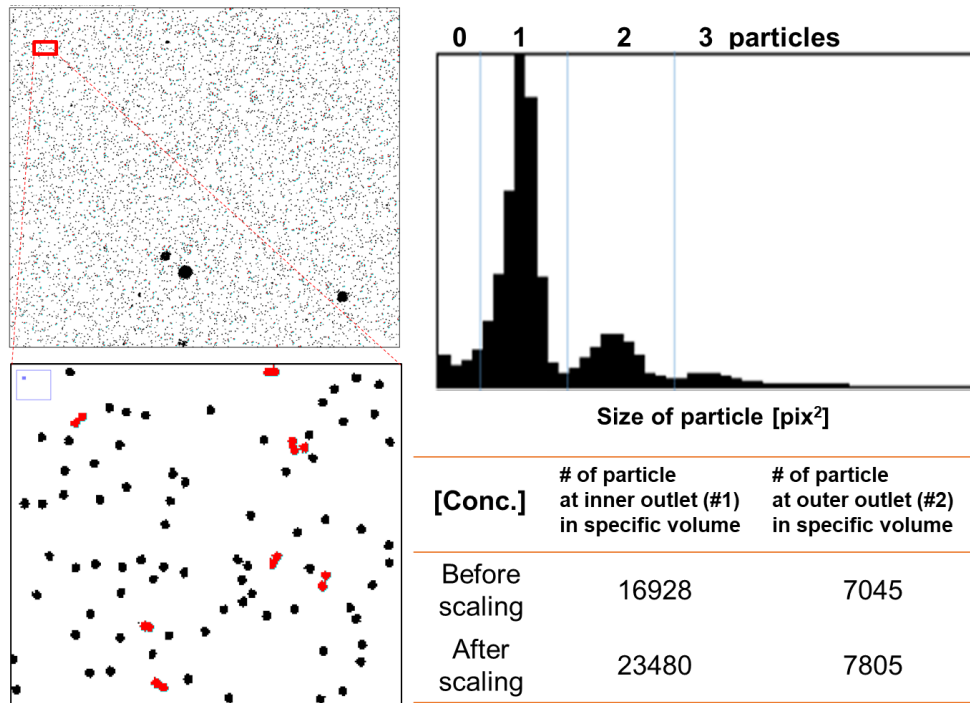


Figure 5-5 Analyzed binary data by *ImageJ* (left) its counting histogram (upper right) and total number of particles counted on the picture (lower right)

Analyzed data from the picture of two outlet of the 2 μm in Figure 5-3. Histogram, right-hand side, with the number particles at each bin in the Y-axis and particle area [pix^2] in the X-axis, which is divided in 50 bins. Bin range of largest frequency is 16-18 pix^2 and it could be considered as 2 μm particles. Even though only 2 μm particles are injected, range shows from 0 to 100 pix^2 . Also, several bell-shaped curves are shown on the histogram. They represent the existence of aggregates. The number colored white in the black bottom on the histogram represents the number of particles composing an aggregate. Blue lines divide their range. If small debris on the image are neglected and aggregates are scaled up, the number of total particles would be estimated more accurately. The number of particles counted by *ImageJ* without scaling is 16928 and the one with scaling yields 23480; 2539 particles are neglected, and 4468 particles are scaled up.

5.2.3 Calculating particle-rate and separation efficiency

The value measured above is particle concentration. Water, or solute, gets transferred between the inner and outer lanes in the microfluidic device, changing the concentration of the streams. Thus, particle concentration cannot be employed to calculate particle separation. Instead, particle-rate should be utilized for separation efficiency because the total particle mass does not

change in the system. Particle-rate could be estimated by multiplying flow-rate and particle concentration.

Such estimation of particle-rate to evaluate separation efficiency is illustrated in the following. 6 ml of particle solution and water were injected at the inner and outer inlets respectively. 9.5 ml of solution came out through the inner outlet (#1), while 1.5 ml of solution did through the outer outlet (#2). It seems that 1 ml of solution remained inside the channel, which makes sense because the channel was empty when the process started. Ignoring volume that remained in the channels, the ratio between inner and outer outlet volumes yields 6.33, in good agreement with the flow-rate ratio of 1:6.15 calculated by computer simulations [Table 5-5]. Also, concentration ratio estimated by image processing gives a ratio of 23480:7805 (see § 5.2.3). Then, particle-rate ratio, determined by multiplying flow-rate ratio and particle concentration, becomes 23480:49405. Assuming that the number of particles injected into the inner inlet is the sum of the number of particles collected from the outlets, separation efficiency becomes $SE = 49405 / (23480 + 49405) \times 100 = 67.78 \%$ according to equation. This value is in very good agreement with the result calculated by computational simulation: 69.7% or 68.3% [Table 5-5].

Table 5-5 Separation efficiency evaluation using experiment and simulations

Case	Inlet flow	Inlet length	# of particle per second	Particle concentration	Flow-rate ratio	Separation Efficiency
	[ml/min]	[μm]	In1/Out1/Out2	Out1/Out2	Outlet1/Outlet2	[%]
Exp.	0.50	>1000	-	23480/7805	6.333	67.8
Sm.1	0.50	1000	514/358/156	-	6.181	69.7
Sm.2	0.50	2000	922/630/288	-	6.150	68.3

5.2.4 Durability test for multiple running

For A-batch particles separation test, most of channel except A16 cannot collect any solution at outlet. Test was conducted at 0.1 ml/min to all channel. Volume ratio at outlet was similar compared to pressure model in first running (volume ratio of volume collected at outer lane to inner lane is measured as 2.2 in experiment and expected ratio by circuit model is 2.64). However, even A16 represents bad particle separation during the test. 10 μm particles, which should not be observed at outer lane, are observed at collected outer lane solution. Several tests are repeated for A16, particles aggregation was observed in the microchannel [Figure 5-3]. Sometimes, aggregation blocks one of lane. Washing out at ultrasonication bath help to reflow solution inside of the channel, but volume ratio is not one we expect. See more information about repeating test in channel A16.

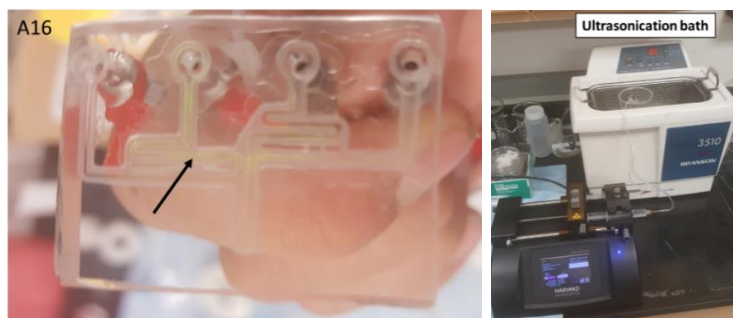


Figure 5-6 Particle aggregation on the channel

Left, image for channel A16. Black arrow is pointing to yellow-green aggregates in the microchannel. Right, ultra-sonification bath was employed to wash out aggregates particles.

Table 5-6 Repeating water injection tests for A16 channel

Volume collected at outer outlet is larger than one at inner outlet in the first running. It was similar result drop expected by pressure circuit model. However, volume collection tendency was switched at 2nd and 3rd running. Inner lane was closed off totally at 4th running. After 4th running, aggregated particles were pre-cleaned by DI water of 0.1 ml/min for 50 minutes in the ultra-sonication bath. Then, flow started to run again. After 8th running, however, cover is delaminated from the body and water start to leak. Volume difference between inlet and out is due to volume of external tubing around 0.79 ml.

#	Flow rate [ml/min]	Volume injected at each Inlet [ml]	Volume Collected at Inner Outlet [ml]	Volume Collected at Outer Outlet [ml]
1	0.1	5 / 5	2.5	6.6
2	0.1	5 / 5	7.0	3.0
3	0.1	5 / 5	6.0	3.3
4	0.1	5 / 5	0.0	9.5
5	0.15	5 / 5	5.0	4.1
6	0.15	5 / 5	5.2	4.0
7	0.20	5 / 5	3.5	5.7
8	0.25	5 / 5	3.0	6.5

After 8th running, cover of the channel was delaminated from the body. Water started to leak

Other A-batch channels does not have solution collection during the test. Instead, there are some defect are observed and interestingly highly related to bonding method used. During the test with channel A1-A12, made by dry adhesive and solvent bonding, tubing was popped off from the tip after around half hour from water injection started. However, A13, A14, A15, A17 and A18, UV adhesive is employed are facing with leaking problem at the cover and the tubing. A16 was working good channel. More investigation is required to verify this relationship and imaging investigation is determined.

5.3 Imaging investigation

Microscopy will enable the observation of micro structure inside of the microchannel nondestructively. Upright microscope (Axioskop 2 plus, Zeiss) equipped with a camera (Grasshopper3, PointGrey), a mercury lamp (HBO 100) as an upright light source, blue light with filters (FITC) was employed. Extra light source (3115PS-12WB20, Schott Fostec LLC) was

installed at bottom of the channel [Figure 5-7]. Channel located on the fixture with cover-side of the channel pointing up. Objectives providing various levels of magnification will be used: 4X is adequate for observing the entire curved segment in a single shot but it is a little bit dim; 10X and 20X are proper to observe particle trajectories in the channel or a specific pattern on a single lane. Microstructure along all lane is recorded and we look for something in common from all images for both good channel and bad channel.

Fluorescence particles with 2 and 10 μm diameter Fluoresbrite® YG Carboxylate Microspheres (excitation 441 nm, emission 486 nm) are injected into some channels to represent behavior of particle inside of the channel. Some aggregates are still remained on the channel.

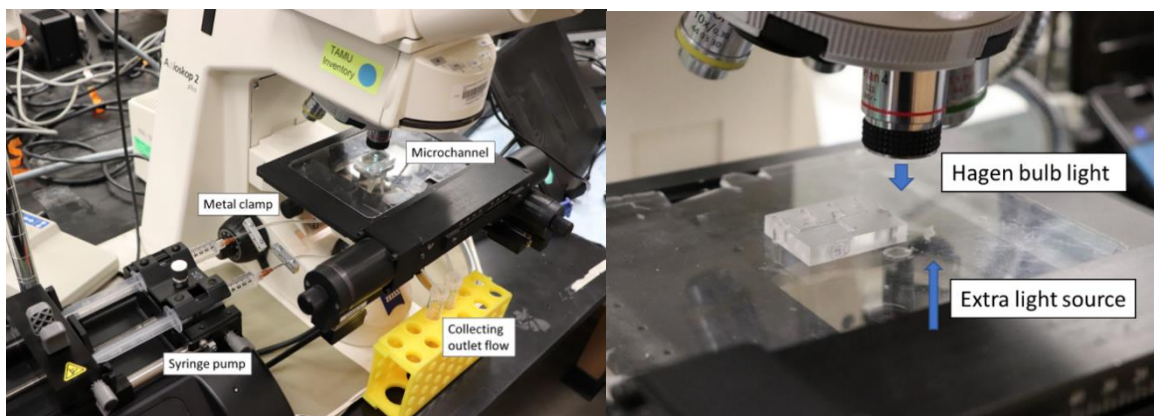


Figure 5-7 Configuration for image processing

Left, configuration of the system for imaging inside of water injection. Right, halogen lamp exposes white light (or filtered blue light) from magnification lenses and extra light source is exposing light below the channel.

5.3.1 Water injection test and its images

To comparing result by particle injection test and microscopic image investigation, Simplified particle injection test was conducted to B-batch and C-batch channels. Instead injecting particle solution at inner lane, DI water was injected at both lanes to check defect.

For B batch channels, water injection test was conducted at flow-rate of 0.3 ml/min each to inner and outer lane. The results initially obtained can be summarized as follows. Case (1): water came out at both exits only in the case of B2, B10 and B15, but pump is stalled in the end. [Figure 5-8] demonstrates water flowing along lanes. Case (2): water came out only at outer lane and the pump are finally stalled in the B3, B7, B8 and B13 channels. Case (3): water is not coming out at both exits and pump are automatically stalled in B1, B4, B5, B6, B9, B11 and B14 channel. Case (4): There was water leakage at B12. Most of channel does not have leakage. It means adhesive is working well up to 146.4 PSI (maximum pressure delivered to each syringe with PHD-ULTRA and BD 10 ml plastic syringe, explained in section 1.3) at first time. However, this test does not guarantee durability of adhesive. Multiple exposure to pressure below 146.4 PSI might damage to bonding.

Water injection test was conducted to some channel for C9, C13 C14 and C21 with flow-rate of 0.1 ml/min. Channel C9, C13, C14, made by UV bonding has water invasion over the fluid path. Water goes everywhere in the channel. However, images of channel C21, made by solvent shows blockage at the entrance of the channel. Thus, pump is stalled in the end. [Figure 5-9] represent two kinds of not working channel.



Figure 5-8 Good bonding at entrance (B10)

B10 from inner inlet images. Empty lane (Left) is filled water after water injection (Right)

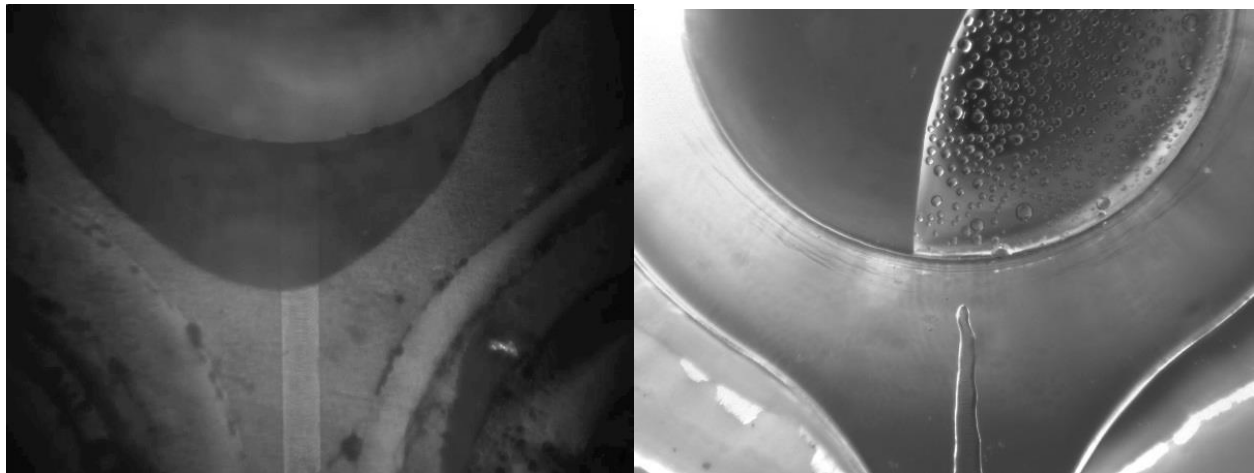


Figure 5-9 Water test images for C9 (left) and C21(right) channel

Left, made by UV bonding. Water from reservoir goes over the weir of the channel. Fluid do not follow fluid path, rather create new bypass. It seems that some of working channel reduce their required pressure by this bypass flow. Right, entrance of the channel, made by solvent bonding with Ethynol. It is definitely seen that fluid path is deformed and blocked. Pump was stalled right after this image frame.

5.3.2 Candidate for well-made channel

Micro-milling machine etches plastic channel by rotating their sharp end tip. Thus, well micro-milled channel has circular wave pattern on the bottom of microstructure and it should keep their pattern even after bonding process. Guckenberger[84] represents wave-pattern images from micro-milled channel, definitely different compared to embossed channel. Microscopic image taken from our microchannels, determined as a good one at water injection test, also show wave-pattern, too [Figure 5-10]. If some of adhesive remained on lane or reactive solvent damages to microstructures after bonding process, however, wave-pattern seen on the images are weakened or disappeared. Therefore, wave-pattern could be employed as a ground to determine bonding condition as good. It should be noted that even one closed-off point result in result that channel is not working properly. Thus, wave-pattern should be continuous throughout entire lane from entrance to exit of the channel to be a good-working channel. Microscopic image investigation is conducted based on this criterion and A16, B2, B10, B15, C2 and C4 channel turn in to be a good-working channel on both inner and outer lane, which is almost same result compared to water injection test. A11, B3, B8 and B13 channel has continuous wave-pattern only on bottom of outer lane. All of other channel has defects both on inner and outer lane.

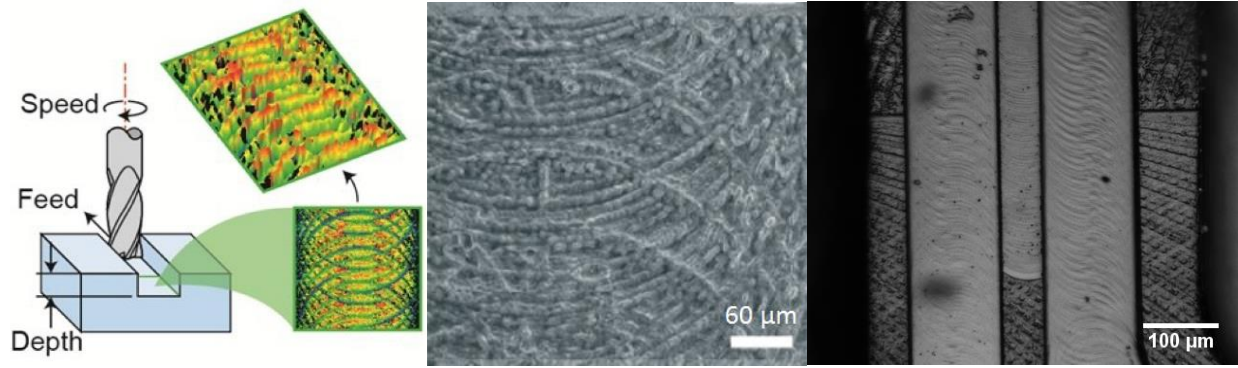


Figure 5-10 Pattern generated by micro-milling on bottom of the lane

Reprinted from ref.[84] Guckenberger with permission. (Left, ref.[84]) Schematic diagram for a milling operation. The inset image was obtained from a profilometer measurement of surface roughness. (Middle, ref.[84]) Phase contrast microscopy image for micro-milled channel by 10x magnification. (Right, this study) 4x magnification upright microscopic image -for channel A16, proved as a working channel by water injection test and particle injection test. It represents circular wave pattern on their channel.

A. CNC Mill Comparison															
	Manufacturer	Model	Cost (USD)	Work Envelope (X,Y,Z)			Feed ipm	Speed RPM	Power HP	ATC tools	Accuracy				
				in mm	in mm	in mm					μin	μm			
< \$50k	Tormach	PCNC 770	\$ 15,500	14.0	356	7.5	191	13.3	337	135	10,000	1	10	600	15
	Minitech Machinery	Mini-Mill/GX	\$ 21,750	12.0	305	9.0	229	9.0	229	40	25,000	-	N/A	-	-
	Haas	Minimill	\$ 34,000	16.0	406	12.0	305	10.0	254	600	6,000	7.5	10	-	-
\$50k - \$100k	Mill Tronics	RW15	\$ 63,000	25.0	635	25.0	635	20.5	521	800	8,000	12	16	400	10
	Bridgeport	GX 480	\$ 68,000	19.0	483	16.0	406	17.0	432	590	10,000	20	20	40	1
	DMG Mori Ellison	Milltap 700	\$ 70,000	27.6	700	16.5	420	15.0	380	590	10,000	7.5	15	400	10
	DMG Mori Ellison	DMC 635 V	\$ 80,000	25.0	635	20.1	511	18.1	460	1181	8,000	17.4	20	40	1
\$100k <	Microlution	363-S	\$ 100,000	2.5	63	2.5	63	2.5	63	-	50,000	-	36	40	1
	Atometric	G4-Ultra CNC	\$ 130,000	4.0	102	4.0	102	3.0	76	1181	100,000	-	14	20	.6
	Datron	Datron M7	\$ 150,000	20.0	508	20.0	508	9.0	229	639	48,000	2.6	15	-	-
	Sodick	TT1-400A	\$ 220,000	15.8	400	9.8	250	11.8	300	1440	40,000	-	N/A	120	3

Figure 5-11 CNC milling comparison

Reprinted from ref.[84] Guckenberger with permission. Expensive micro-milling can control up to 0.6 μm accuracy.

5.3.3 Evidence of bad channel on microscopic images

Although some of the channel has continuous wave-patterns, most of the channels we have has unexpected pattern or shape on their microscopic image. Patterns can be categorized in several

types and how often each pattern is observed was counted. Note that it is something in common for badly bonded channel made by specific bonding method, not all channel produced by specific method. For batch A, dominant pattern was highly related to the bonding methods: dry adhesive, UV adhesive and solvent bonding [Table 5-7]. As basically, bad channel image does not have circular wave-pattern for all bad channel. Images from bad channel made by dry adhesive has many discontinuities, which seems to be air bubbles [Figure 5-12 A1]. Bad channel made by UV adhesive has one more layer which covers the microstructure in the channel. Some tiny dots are observed on the bottom of the channel. Since UV adhesive has high viscosity in usual, it is not easy to apply proper amount of adhesive on correct place, resulting in many failures of microchannel fabrication. If adhesive is not applied enough, place with weak bonding can be broken and turned into be a bypass of fluid. Also, if excessive adhesive is applied on the channel, adhesive could invade the fluid path and can close it off. Furthermore, there is no way to get rid of excessive adhesive remained on the fluid path after UV adhesive become hardened by UV light [Figure 5-12 A14].

Bad channel made by solvent bonding looks simpler. It can be distinguished even by naked eye. If lighter patches with colored interference fringes is observed near free edges of the device [Figure 5-13 left], it can be interpreted as poor bonding coverage. Solvent is evaporated before solvent induce enough reaction to bond between cover and body of the channel, delamination of the channel. If solvent is excessive, on the other hand, bonding will be completed strongly to the degree which microstructure is damaged and close off fluid path [Figure 5-13 right, Figure 5-14 middle]. It can be told from the point that fluid path in the channel is disappeared. If observing through microscope, only parallel guideline is seen on the image and no pattern is observed at place where wave-pattern should exist [Figure 5-12 A10]. There were two possible explanations

for closed-off fluid lane on the images. One is micro-milling was not well established before bonding process. The other explanation is excessive solvent in specific condition can dissolve channel and change the microstructure and its pattern. Latter one seems to be correct in that this pattern is observed only where solvent bonding is employed. For former hypothesis to be a reasonable answer, no wave-pattern should be seen on every bonding method. Channel made by solvent. Other features are also seen on the bad channel with solvent bonding. Single discontinuity and uneven narrow lane are the other feature easily seen on bad microchannel [Figure 5-15 B4]. Image feature called multiple guideline is seen on [Figure 5-15 B11]. It is expected that wrong controlled micro-milling makes multiple line. Dark v-shaped pattern observed near the entrance/exit, especially does at the channel with which the syringe pump was stalled before. It seems to look that closed-off channel are damaged by high pressure [Figure 5-16 (a)]. Diagonal pattern is expected that characteristic of intact surface of COP channel. Irregular depth diagonal pattern is observed on the image like [Figure 5-16 (b) upper]. Particles and fluid are also observed on this pattern after water/particle injection test, meaning that bonding nearby is destroyed. All has crack-like shape on the microstructures [Figure 5-16 (b) lower]. Also, some of curved lane has different color and texture compared to the straight segment [Figure 5-16 (c)]. Finally, liquid is observed in the fluid path in some of microchannel. However, it is not clear whether DI water or solvent (such as isopropyl alcohol) is remained on the channel [Figure 5-16 (d)]. [Table 5-8] demonstrates different criteria turn out similar result. It also represents relation between image feature and channel classification. Interestingly, many of image feature of multi guideline, diagonal pattern, dark V-pattern and dark color in curved lane are observed on classification (2).

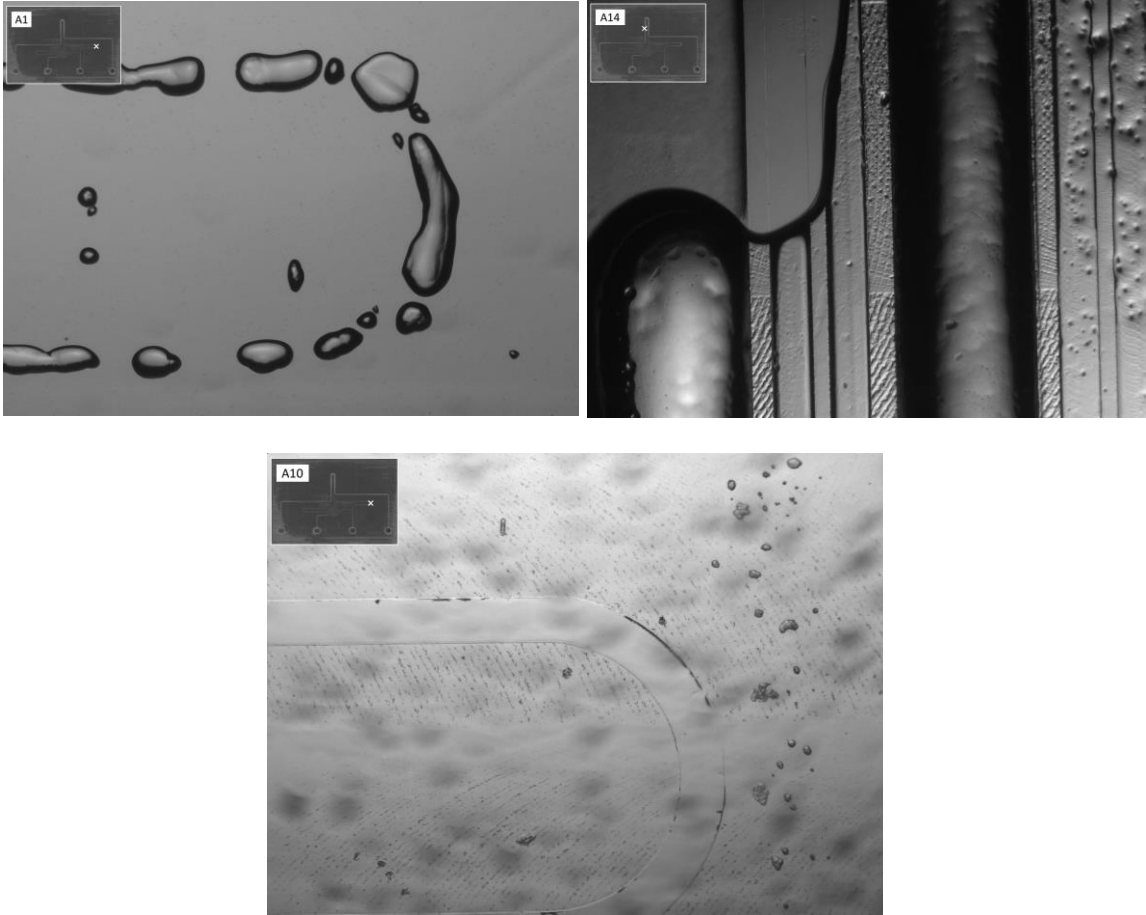


Figure 5-12 Classification of bad channel among batch A

Three figures above are most common pattern observed on batch A channel in terms of their bonding method. Image of A1 refers to as many discontinuities and observed on the channel with dry adhesive. Image of A14 is named as excessive adhesive and seen on the channel made by UV adhesive. Image of A10 are called as no wave pattern and dominant on the channel made by solvent bonding.

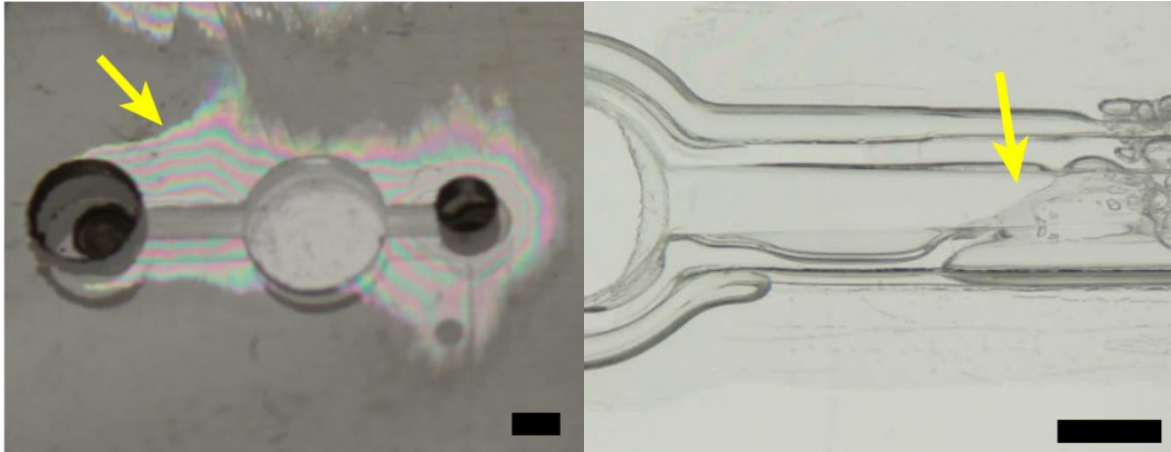


Figure 5-13 Cases solvent bonding is not well established

Reprinted from Wan[85]. Left, poor bond coverage. Region yellow arrow are pointing to is poor bond coverage. Right, excessive bond coverage. Yellow arrow is pointing to damaged microstructure by overly aggressive solvent bonding. Black bar means 1 mm for both picture.

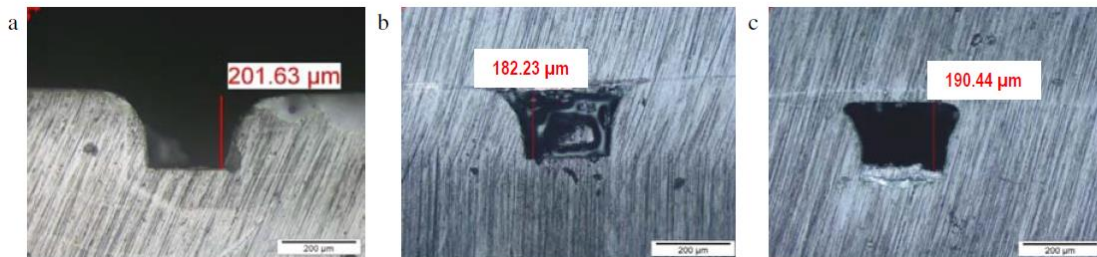


Figure 5-14 Importance of temperature annealing

Reprinted from Ng[86]. Poor bonding is observed when the substrates were not annealed before bonding. Microchannel without annealing was clogged after solvent bonding. PMMA is substrate, solvent is isopropanol, denatured ethanol and acetone.

Table 5-7 Relationship between bonding method and image investigation

Name	Image condition	Bond Method	Weird pattern
A1	Many discontinuity	Dry adhesive	
A4	Many discontinuity	Dry adhesive	
A5	Many discontinuity	Dry adhesive	
A6	Many discontinuity	Dry adhesive	
A7	Many discontinuity	Dry adhesive	
A9	Many discontinuity	Dry adhesive	
A2	No pattern	Solvent	Dark V-shaped
A8	No pattern	Solvent	Dark V-shaped
A10	No pattern	Solvent	Dark V-shaped
A11	No pattern / Unblocked	Solvent	Horizontal crack-like pattern
A12	No pattern	Solvent	Dark V-shaped
A3	No pattern	Solvent	Dark V-shaped
A14	Excessive adhesive	UV adhesive	
A15	Unblocked / cover destroyed	UV adhesive	
A16	Unblocked	UV adhesive	
A17	Excessive adhesive	UV adhesive	
A18	Excessive adhesive	UV adhesive	

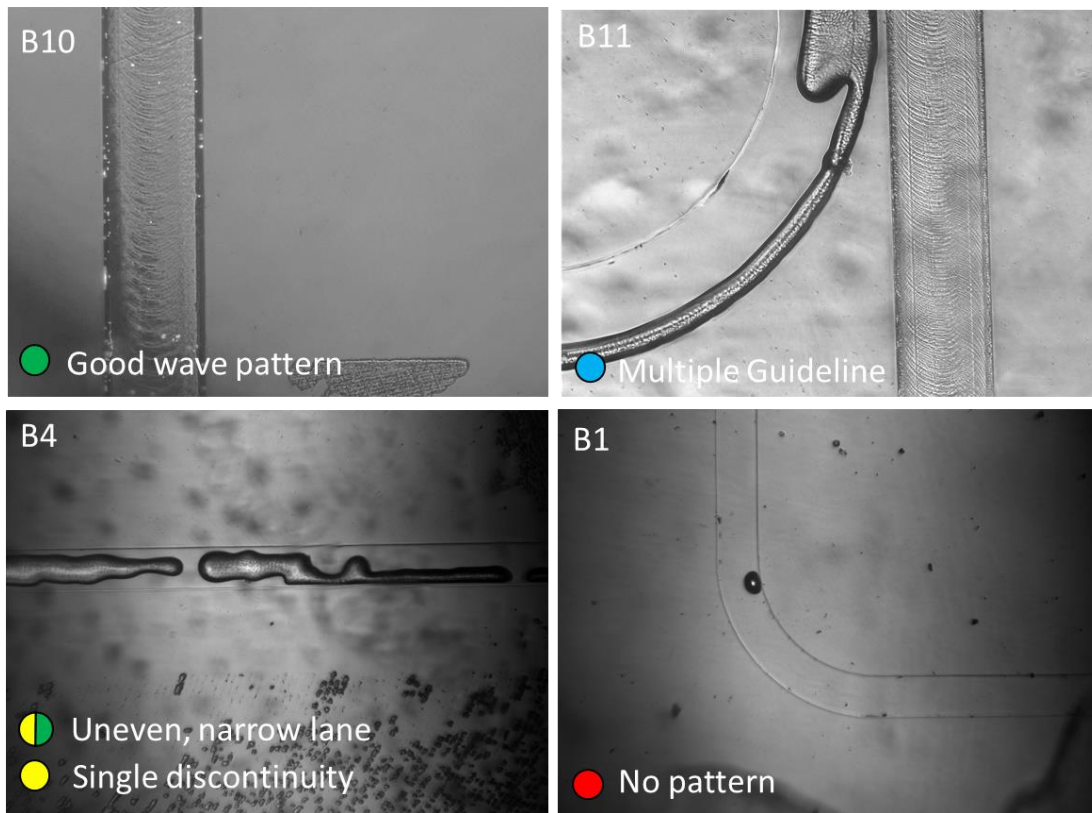


Figure 5-15 Major features for channel B1-B14 made by solvent bonding

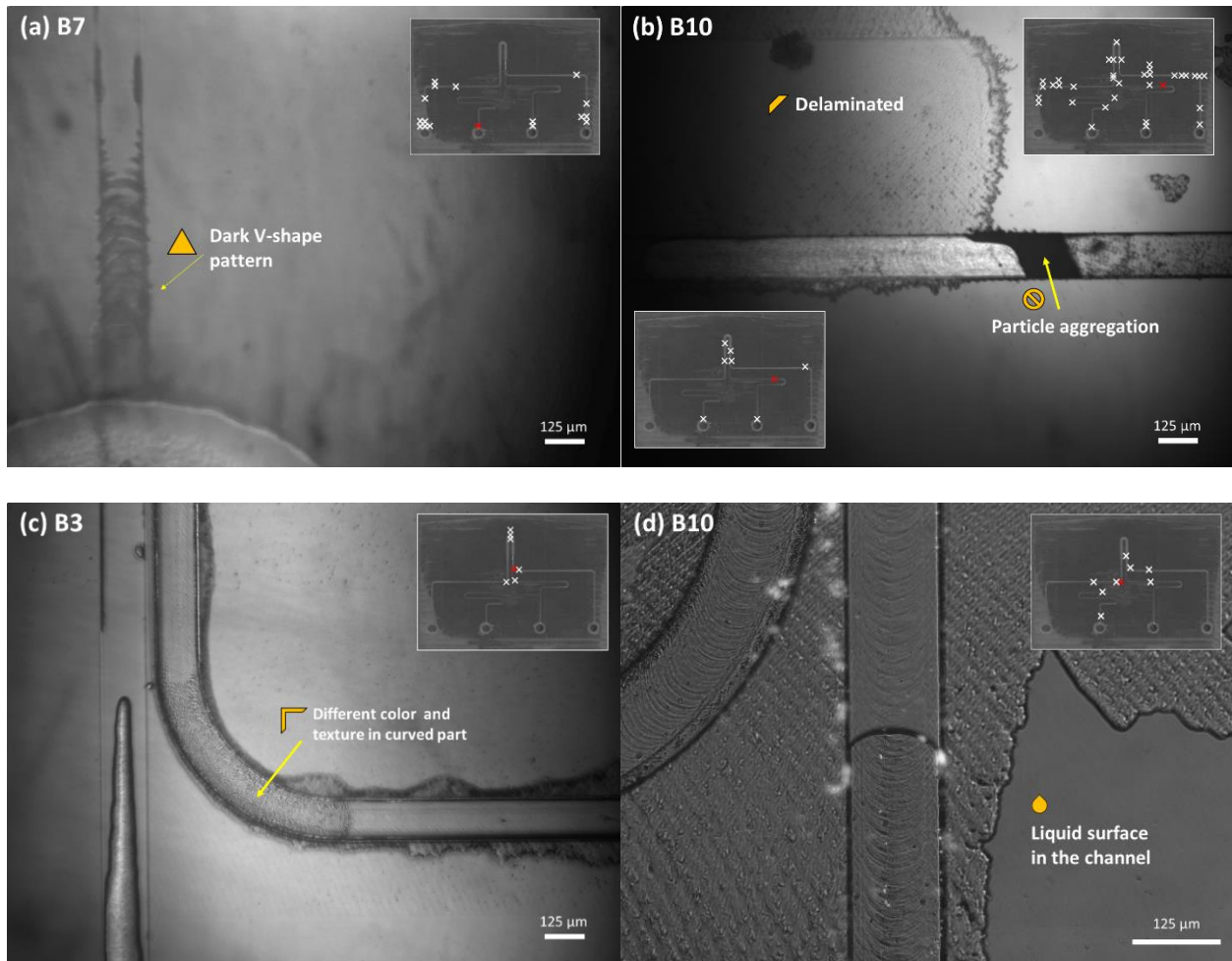


Figure 5-16 Minor features for channel B1-B14 made by solvent bonding

X mark in Inset pictures represents all point that corresponding feature is reported. Red mark is for the picture.

Table 5-8 Feature summaries for B batch channels

Classification for water injection test is: (1) Water came out at both exit, called good channel. (2) Water came out only at outer lane, then pump stalled. (3) water did not come out at both lanes, pump stalled. (4) water leakage is observed. Classification for image investigation test. (1) No pattern and discontinuity are not observed throughout entire channel. (2) No pattern and discontinuity are not observed on entire outer lane. Feature of inner lane is not important. (3) At least one no pattern or discontinuity is observed on each inner and outer lane. (4) Delamination of the cover is clearly recognized on naked eye.

	Water injection test	Image investigation										
B2	(1)->(4)	(1) and (4)	Damaged	0	0	2	0	3	6	0	0	0
B10	(1)->(4)	(1) and (4)	Damaged	0	0	0	0	6	7	0	0	3
B15	(1)->(4)	(1) and (4)	Damaged	0	0	0	0	8	9	0	0	0
B3	(2)	(2)		5	1	0	3	0	2	0	3	0
B8	(2)	(2)		4	1	5	1	0	5	2	0	2
B13	(2)	(2)		5	0	1	2	0	1	5	0	0
B7	(2)	(3)	Difference?	9	0	2	2	0	2	4	2	0
B1	(3)	(3)		5	0	1	0	0	2	1	0	0
B4	(3)	(3)		9	5	3	0	0	1	0	1	0
B5	(3)	(3)		12	0	0	0	0	2	2	0	0
B6	(3)	(3)		8	2	2	0	0	0	1	0	0
B9	(3)	(3)		4	2	1	0	0	1	0	0	4
B11	(3)	(3)		6	0	1	2	0	0	2	0	0
B14	(3)	(3)		6	0	4	0	0	3	0	1	0
B12	(4)	(4)		7	0	2	1	0	2	0	0	0

- No pattern
- Discontinuity
- Not even, narrow
- Multi guideline
- Particle aggregation
- Delaminated, diagonal line ptn.
- Deformation near etrnc./exit dark V ptn.
- Dark color in curved part
- Liquid

Table 5-9 Feature summaries for C batch channels

Channel made by solvent bonding has many defects of no milling while one made by UV adhesive has many stops. C11 and C12 is not delivered from the company.

Name	Type	No milling	Discontinuity	Not even channel	Spot
C1	Solvent bonding	9	2	5	5
C3	Solvent bonding	13	1	1	0
C5	Solvent bonding	10	1	1	2
C6	Solvent bonding	6	0	0	0
C7	Solvent bonding	7	1	1	1
C8	Solvent bonding	10	1	1	0
C15	Solvent bonding	5	4	1	0
C16	Solvent bonding	10	3	2	0
C17	Solvent bonding	8	5	1	0
C18	Solvent bonding	7	2	0	1
C19	Solvent bonding	7	3	3	0
C20	Solvent bonding	3	8	6	0
C21	Solvent bonding	7	4	2	0
C2	UV Adhesive	0	0	0	1
C4	UV Adhesive	0	0	0	0
C9	UV Adhesive	0	0	0	2
C10	UV Adhesive	1	0	1	6
C13	UV Adhesive	1	0	0	6
C14	UV Adhesive	3	0	1	4

5.3.4 Aggregation of particles in the channel

Channel of prototype, A16, B2, B10 and B15 in which flow can move at both lanes are and investigated by microscope. They have some common on images. Fluorescent particles are observed on the place where it should not exist, meaning there is a bypass or room for fluid to be collected somewhere in the channel. The reason why flow can move in these channels was reduced pressured drop can be obtained from bypass and empty room. However, it is the reason not only

channel work but also channel stop. As flow running, bypass is getting large and finally delaminate the cover. Also, empty room become fully filled with solution, then channel cannot save pressure, turning into close-off problem [Figure 5-17].

Also, particles are aggregated in many areas of microchannel, resulting in lane close. It can be observed at supplying line [Figure 5-18] and bridge [Figure 5-19]. At adjacent to closing point, we can see delamination of channel [Figure 5-19]. One of hypothesis for aggregation in the microchannel is that COP has high hydrophobicity which might hold hydrophobic fluorescent particles. Li [87] said that polyacrylamide coating is proceeded to attenuate its hydrophobicity. There is possibility that company did not know about this process and thus did not do it. Or, test was conducted more than several months after the microchannel is fabricated. This long period might weaken coating effect.

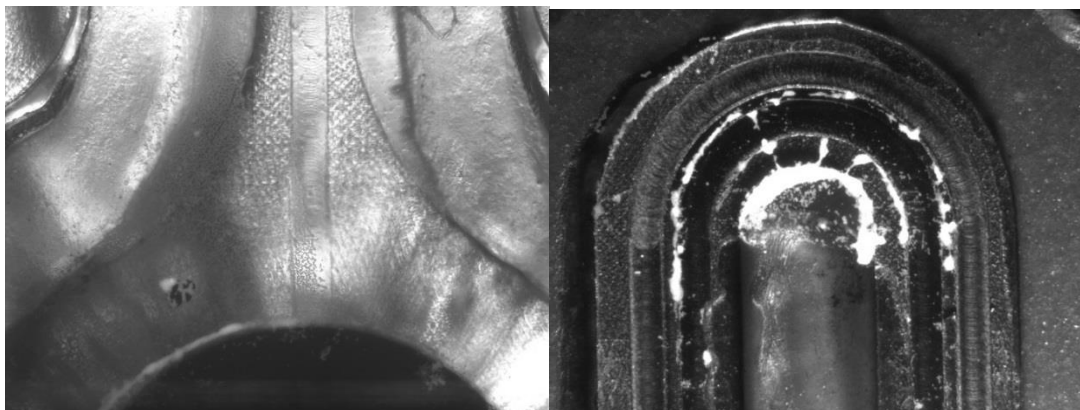


Figure 5-17 Fluorescence particle images for good prototype channel

Left, fluorescent particles are observed on bypass. Right Particles are aggregated at not only bridge, but it is also at groove for silicon gasket.

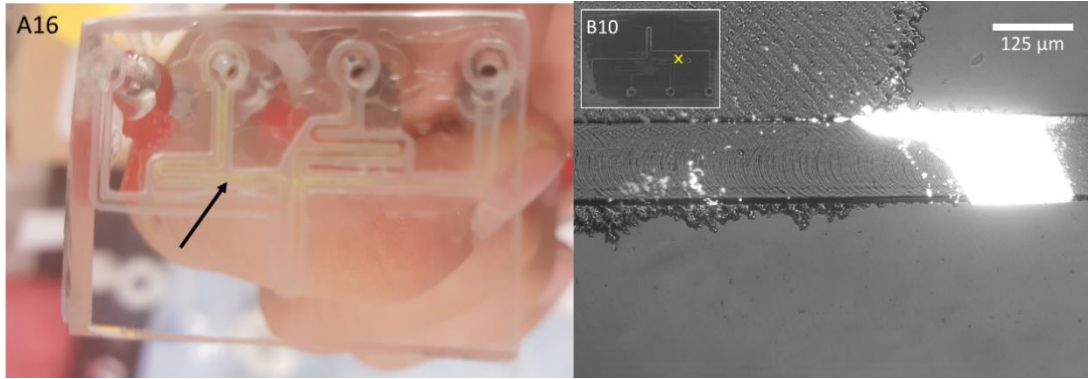


Figure 5-18 Particle aggregation on the channel

Left, camera image for channel A16. Black arrow is pointing to yellow-green aggregates. Right, fluorescence image for channel B10. Bright part is a particle aggregate closing off the lane. Inset and yellow X mark represent position of the picture. To avoid this aggregate bonding near lane are broken and cover is delaminated from the cover. Bypass is generated.

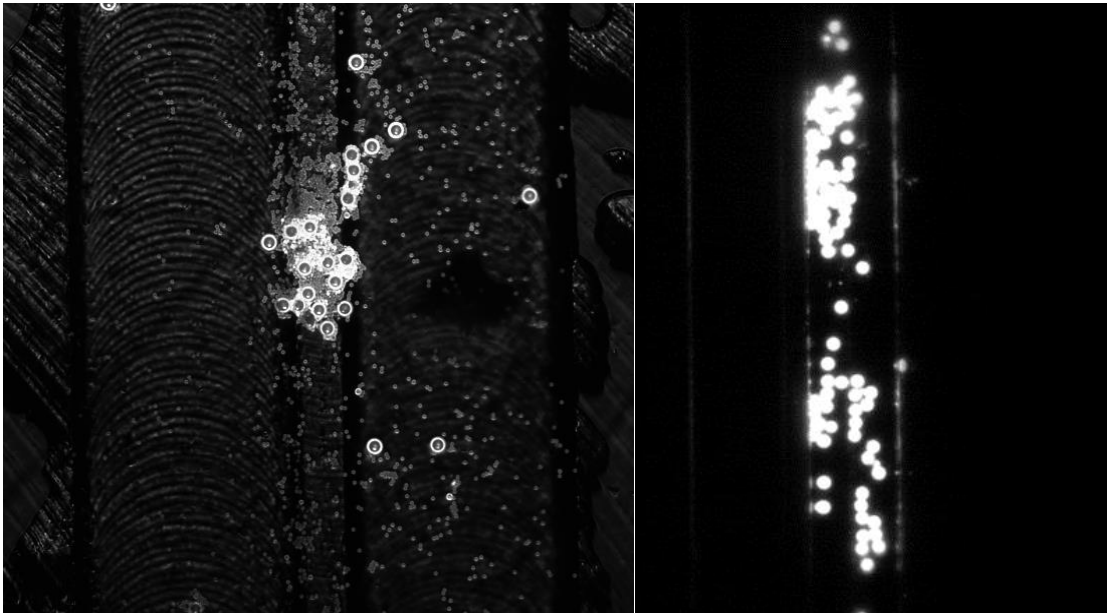


Figure 5-19 Fluorescence particle images

Left, x10 magnification images for Channel B15 after 8 running. Particles are aggregated at bridge area. Also, 10 μm particles are observed both in inner and outer lane. Bridge did not act as a filter. Right, x4 magnification images for prototype channel. Particles has 20 μm diameter are aggregated in the lanes.

5.3.5 Particle trajectories

Particle trajectories can be observed through blue laser with Halogen lamp and FITC filter, essential for tracking inertial focusing or quasi-inertial focusing. B3, the channel that only outer lane is employed. Since no separation is expected in this channel, inertial focusing can be solely focused on. 2 μm fluorescent particle solution are injected into the lane at 0.1 ml/min. 10x and 20x magnification lenses are employed. Strains of particle trajectories can be recorded by increasing exposure time or stacking video frames. [Figure 5-20] represent particles movement in the channel. Since particles is not large enough and outer lane is large (Re_p 0.0217 and R_f 0.022), inertial focusing is not observed and particle are well distributed. Bright parts are particle aggregates in the channel. We also conducted 20 μm fluorescent particle injection into B3 channel, representing different behavior of particle in the channel (Re_p 2.17 and R_f 2.20). [Figure 5-21] represents inertial focusing of particles near at outer wall. After several tests, particles are aggregated at specific region in the fluid path to bother particle movement [Figure 5-22]. We would like to test for 10 μm particles in identical condition (Re_p 0.54 and R_f 0.55) but B3 channel is delaminated, impossible to generate flow in the microchannel.

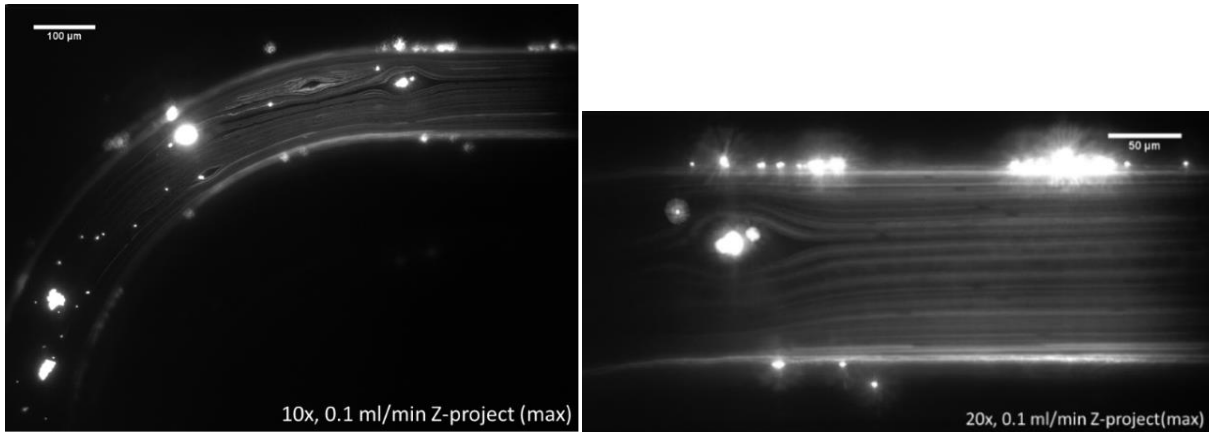


Figure 5-20 Particle trajectories for 2 μm fluorescent particle

Channel B3 is employed. Left: 10x lens is employed. It had recorded for 10 seconds with 30 FPS and all frame are staked on one image to see particle trajectories. Right: 20x lens is employed. It had recorded for 6 seconds with 30 FPS and all frame are staked on one image to see particle trajectories. Because of long exposure, particle trajectories look as a strand on the picture. Glittering spot indicates an aggregate attached to the wall. Some of aggregates are stacked on outside of the channel and something moving outside of the channel. It indicates that bondage is slightly damaged, and space are formed.

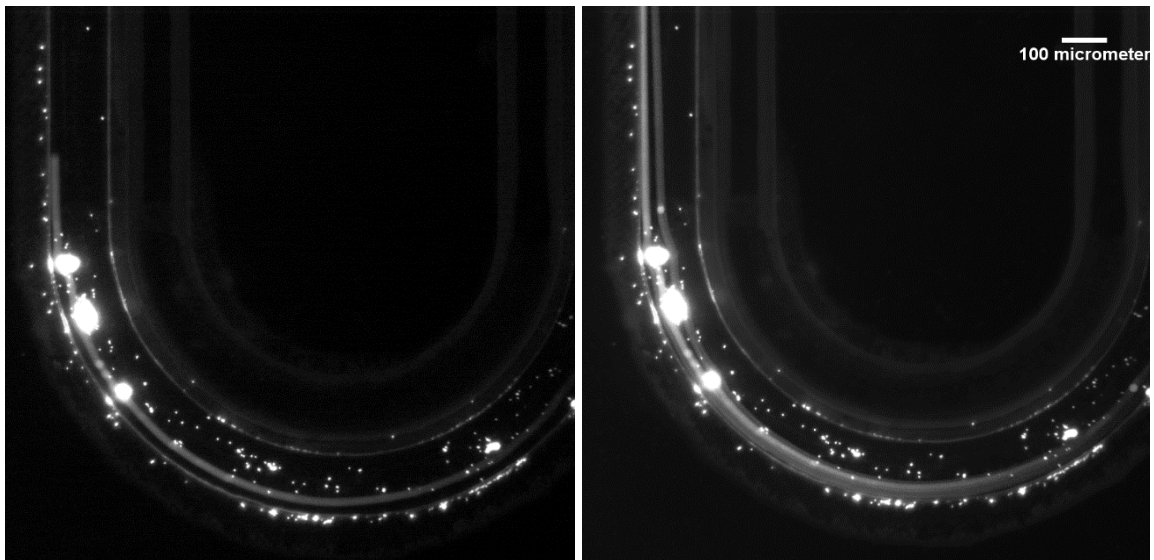


Figure 5-21 Particle trajectories for 20 μm fluorescent particle

Particle trajectories are recorded for 6 seconds with 20 FPS. All frame is staked on one image to see particle trajectories. Left image illustrates single frame and right shows staked images by *imageJ*. Bright dots are particle aggregates already stick to the channel. Almost single strand of particles trajectory is observed on the images. Channel B3 is employed.

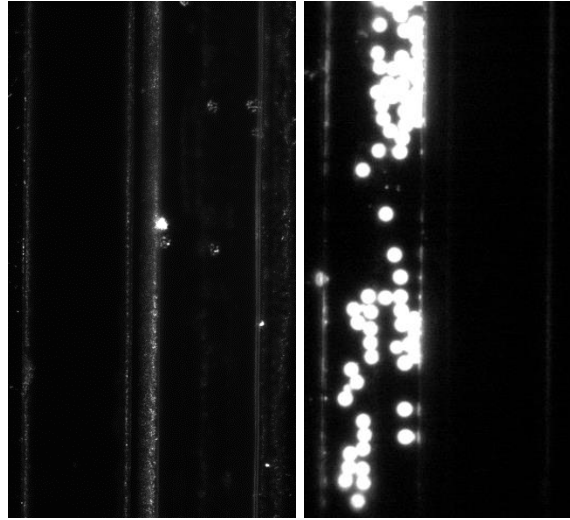


Figure 5-22 Particle aggregates at filtration part

Left is image before injecting 20 μm particle and right is after image. After several experiments tries, particle aggregation is observed on the fluid path. Channel B3 is employed.

5.4 Conclusion

Design of the channel has not only unnecessary part but also careless fabricated part. Its design require high pressure drops though pressure employed for separation is not massive, bringing out physical damages on the bonding between cover and channel. Supplying line is not related to performance of the channel but taking lots of pressure. So, it should be redesigned to minimize pressure drop. Retrieving line has high relation to enrichment of the solution to be separated. It should be redesigned to improve suction power. Driving source of this separation system is pressure difference between parallel lane in filtration part. However, pressure difference in current design are diminished in rapidly because hydraulic resistance of the bridge is not high enough. By increasing length of bridge or adding membrane, secondary direction flow could be survived along the whole filtration part. Also, particles trajectories in the channel is highly related to quasi and ordinary inertial focusing. It should be more studied for finding out optimized size of

the channel based on microfluidic dimensionless variables. We can control large particle away from the bridge not to be separated and not to damage to the channel by employing inertial focusing.

Company does not have ample knowledge for bonding methods, turning out wrong fabrication of the channel. They tried many kinds of adhesive and bonding method. UV adhesive and solvent bonding are notable method by which channel represents some working performance once. For UV adhesive channels, they have some leaking feature for certain reason. So, company employed gasket in the channel to seal aperture. They made groove near fluid path to install gasket. It might prevent flow outside to gasket, fluid can flow freely inside of the gasket. flow does not follow our intended flow path. Also, gasket and groove does not perfectly fit, empty space is created, turning out weak point. Bypass is generated, and solution and particles are collected. It is believed that fluid can flow in this high pressure consuming channel thanks to this empty space, but it is not usual operation. Channel made by UV adhesive are delaminated well, attributed to the fact that bypass generated in the channel could damages to bonding.

In solvent bonding methods, solvent (usually isopropyl alcohol), after bonding should be removed to prevent further deformation by solvent. It is either usually naturally vaporized and forcedly dragged out from the channel. However, design we have has tiny and long path, not good for circulation, yielding solvent residue in the channel. It could deform fluid path, finally closed off inner lane. Inherent channel blocking is usually observed in inner lane of microchannel with solvent bonding, supporting my hypothesis. Also, it is reported that solvent bonding reduces height of the channel even though it is working channel. It was reported that 10 μm reduction is observed on 200 μm height microchannel. Considering our height was 5 – 40 μm , even though solvent bonding was successfully completed, there is a possibility that channel is blocked inherently. Many reports note that temperature annealing is most important factor for solvent

bonding. However, there is no information from the company about temperature during solvent bonding. It is suspected that company did not understand importance of temperate during bonding process. Finally, many fabrication papers about solvent bonding recommend grooving near microstructure and edge of the channel. However, I could not observe any evidence of grooving in the microchannel fabricated by solvent bonding. Even well bonded microchannels are broken in the end after several usages, showing particle aggregation in the microchannel. It seems that feature of hydrophobicity of COP channel was not attenuated enough before hydrophobic fluorescent particles are injected.

6. SUMMARY AND FUTURE WORK

6.1 Investigation of the effect of curve segment

This filtration system in straight microchannel has a limitation on improving particle separation efficiency. Since pressure difference only exists near the filter (or the bridge), only a fraction of the particles experiences sufficient secondary drag forces to be transferred through the bridge and separated. Particles far from the bridge keep their location and does not have chance migrate near the bridge. Thus, at certain point, particles separation efficiency cannot be improved solely by pressure difference between lanes because there are no particles to be separated near the bridge. Particles far from the bridge should be moved toward the bridge to enhance particle separation efficiency by generating secondary flow at entire microchannel. Curvilinear channel is introduced because the curved segment could partially make up for it by Dean vortices that increase particle encounters with the bridge. However, this idea has faced with difficulties that unexpected behavior of either particle or fluid occurs under certain conditions. For instance, pseudo-inertial focusing in the curved segment prevents some particles above a certain size from migrating toward the bridge and crossing the channel. Further study is essential to achieve optimized performance.

Radius of curvature of the curve segment, a length from origin to middle of channel, is the one of main parameter to determine its characteristics. However, radius of curvature of curved segment is yet to be studied. It is attributed to the fact that many effects are integrated when dealing with this parameter, being hard to separate one factor solely from others. Factors can be

summarized in three categories: particle residence time, behavior of particle and behavior of secondary Dean flow. See [Figure 6-1].

Radius of curvature is directly related to total length and velocity of fluid, which affects resident time of the particle. If radius of curvature is not large enough, particles could pass the segment before something occur. The main driving force to be employed in the curved channel is particle rotation and inertial focusing and both need a certain length to be developed.

Also, radius of curvature determines the strength of vortices and inertial focusing generated in the curved segment. It affects both particles and fluid behavior, and distinct regions can be distinguished in terms of radius of curvature for both instances. From the point of view of fluid behavior, a pair of vortices are typically generated in a curved channel. In the cases of extremely small or extremely large radius of curvature, however, multiple vortices or no vortex are generated, respectively. This can be expected based on the Dean number. Multiple vortices are a complex condition to be controlled, so it should be avoided. On the other hand, particle behavior is more complex. In small radius of curvature, the R_f value is less than 0.1, so particles are entrenched in the vortices and rotating along the streamlines. In intermediate radius of curvature, particles are still rotating but following smaller rotating trajectories due to vertical shear-induced lift force. When the R_f value is large, inertial force becomes dominant and inertial focusing is observed in specific regions. But the position and the number of focusing points is still ambiguous. This inertial force dominant case is not considered to avoid trying to control complex condition that can occur. Summarizing, optimization of the radius of curvature is not an easy problem. First, it should be determined which forces are being employed for separation. Then, the optimal length is investigated in terms of separation efficiency. The concept employed in this study is to increase the chance for particle to interact with the narrow bridge by Dean vortices. So, small radius of

curvature keeps particles in the Dean drag force dominant region where Dean vortices is generated. However, too small radius of curvature might generate multiple vortices. There were difficulties in certain conditions to conduct computational simulations, as they did not converge well. All had similar large Dean numbers in common, suggesting that the problems with the simulation emerge from the generation of multiple vortices in that condition. Also, 500 μm radius of curvature employed in this study is somewhat short to give enough chance for particles to rotate. Due to this short length, particles did not complete one rotation while they were in the curved channel. In other words, they get out from the curved segment before they rotate one full cycle. It means that some particles do not have the chance to face with the narrow bridge to be sucked. Therefore, optimum radius of curvature should be investigated in future studies: longer radius of curvature for more rotation of particles but without generating any quasi-inertial focusing. To investigate the effect of radius of curvature, spiral microchannel has been widely studied by many research groups because it could have long enough length for curve effect to affect the particle behavior. Some of them focused on behavior of inertial focusing and others employed dean vortices to separate particles. Reynolds number Re_c , Dean number De , confinement ratio λ and curvature ratio δ , and the R_{fvalue} suggested by Gossett [72] are parameters that represent the characteristics of a spiral channel. [Table 6-1] summarize the spiral channel study conducted, its dimensionless values, and its behavior region.

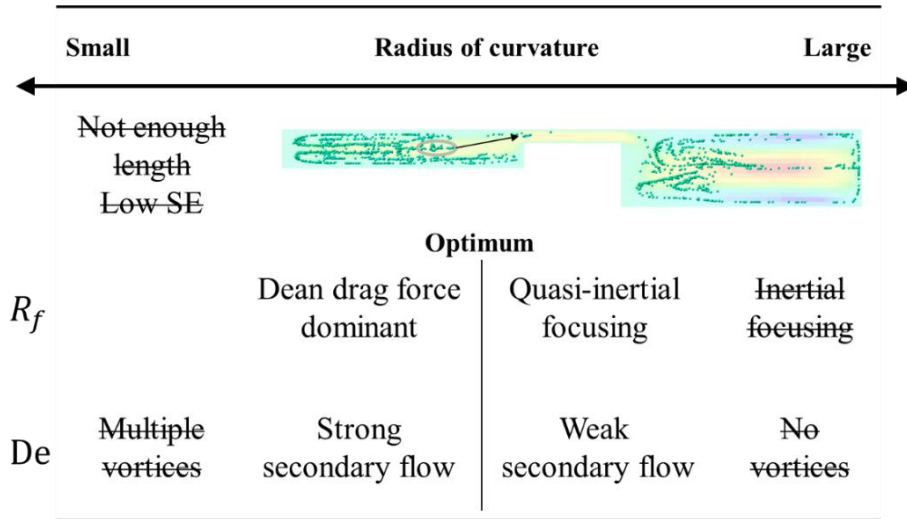


Figure 6-1 Effect of radius of curvature

Table 6-1 Non-dimensional values for spiral channels in the literature

RC is radius of curvature, W and H is width and height of channel, respectively. Dh is hydraulic diameter of the channel. V is average velocity at inlet flowrate. Re,c and Re,p is channel and particle Reynolds number, respectively. δ is curvature ratio and λ is confinement ratio. Rf is force ratio suggested by [72]. DD stands for Dean drag dominant, IM does for intermediate, and IF does for inertial force dominant.

	RC [μm]	W [μm]	H [μm]	Q [ml/min]	Re,c	De	Dp [μm]	λ	Re,p	Rf	Region
Nivedita [16]	3500	250	150	3	250	40.9	10	0.053	0.71	0.106	DD
	3500	250	100	3	286	40.8	10	0.070	1.40	0.240	DD
	3500	500	100	3	167	25.7	10	0.060	0.60	0.151	DD
Warkiani [88]	10000	500	150	0.6	31	3.3	3	0.013	0.01	0.015	DD
							15	0.065	0.13	0.366	IM
Guan [18]	7500	600	80	3.5	172	16.6	5.8	0.041	0.29	0.178	DD
							9.8	0.069	0.82	0.508	IF
Keinan [17]	900	200	33	0.300	42.9	7.61	15.5	0.274	3.213	2.378	IF
				1.800	258	45.6	15.5	0.274	19.27	2.378	IF
Clime (Circle) [69]	15000	100	100	0.100	21.2	1.23	2	0.020	0.008	0.120	DD
							5	0.050	0.053	0.750	IM
							8	0.080	0.136	1.920	IF
Martel [71]	2000	100	50	0.210	44.6	5.75	15	0.225	2.256	3.038	IF
				0.520	110.3	14.25	15	0.225	5.586	3.038	IF

6.2 New fluid path design

As mentioned in Section 4, current design has inherent problem on pressure distribution on the microchannel; High pressure should be loaded on the microchannel and its distribution is biased on specific position. This section will demonstrate new design of the microchannel to resolve these problems. It will be strongly proposed that cross-section should be enlarged and length of supplying and retrieving lines should be manipulated.

One of the easiest method to reduce pressure drop at microfluidic device is to enlarge cross-section of the microchannel. Enlarged cross-section dramatically reduce pressure drop required and thus flow-rate, which directly related to high-throughput, can be increased. However, it is not easy tasks. Change of cross-section might result in huge change of fluid characteristics, being hard to estimate the result. Identical fluid pattern, two Dean vortices in curve segment, is recommended to understand phenomena easily. Multiple vortices region should be avoided. Thus, channel Reynolds number and Dean number should be kept by manipulating flow-rate and geometric factors precisely.

Behavior of particle in the curve segment will also be changed as cross-section of the microchannel has been modified, too. However, it does not need to maintain its feature as same as one current design have because it reduces separation efficiency. Unexpected quasi-inertial focusing is observed at high flow-rate, attenuating separation efficiency of particle with diameter of 3 μm . Considering inertial microfluidic effect cannot be negligible at high throughput system, it would be better to figure out how to control inertial focusing for specific particle size on purpose. A new device design should be proposed to perform optimally for CTC separations. Small cells should be get rid of from the lane where they are injected, and large cells should be remained in the lane [Figure 6-2]. To do so, the microchannel geometries should be selected to avoid the region where inertial focusing captures small particles in the curved segment and the effect is also used to capture

large particles for improved separation efficiency at the same time. It is expected that R_f and Aspect ratio is the parameters related to particle behavior feature. By trimming geometric parameter, R_f value for particle with a diameter of $15\ \mu\text{m}$ at new design channel could have its value as similar as that of $3\ \mu\text{m}$ at current design channel. We can expect small particles are under Dean vortices dominant region and large particles are under (quasi) inertial focusing dominant region. [Table 6-2] demonstrates some of suggested geometric parameters of cross section, radius of curvature for new microchannel design and its flow-rate. Their value is specified to maintain channel Reynold number and Dean number and satisfy R_f value for target size of particle.

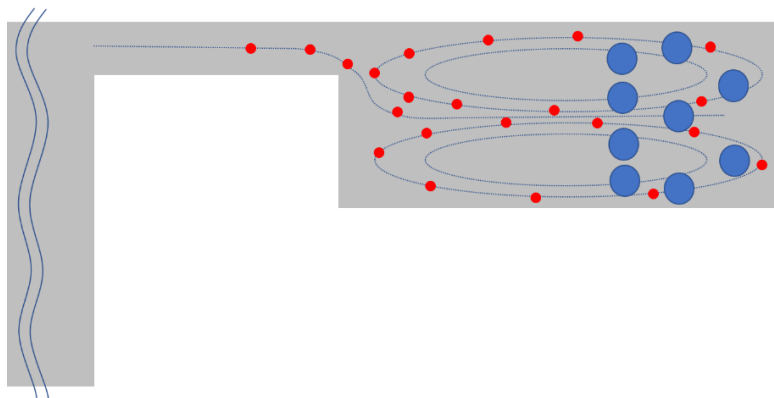


Figure 6-2 Schematic diagram of new device operation

Cross-section view of the device. The outer lane (left), in which sheath flow is injected, is omitted on the figure. The rotating axis of the channel is located at the right-hand side of the channel cross-sectional view. Big particles (blue), being inertially focused, stay in the inner lane away from the bridge. Small particles (red) are rotating in vortices and sucked near the bridge

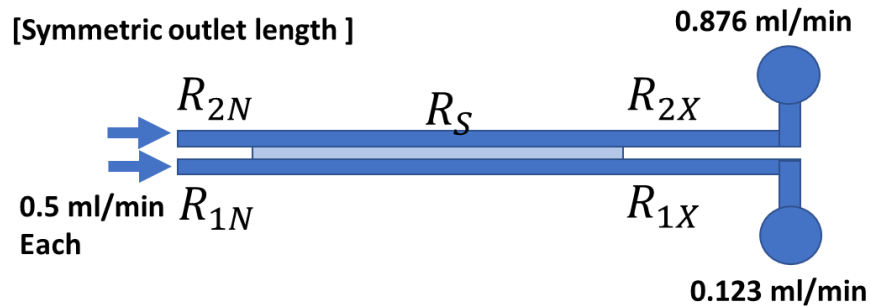
Table 6-2 Enlarged microchannel geometry, keeping its microfluidic characteristics

	RC [μm]	W [μm]	H [μm]	Q [ml/min]	Re,c	De	Dp	λ	Re,p	Rf	Dp	λ	Re,p	Rf
This	650	125	20	1	229.9	40.25	2	0.058	0.773	0.110	3	0.087	1.740	0.247
			40	1	202.0	42.41	2	0.033	0.220	0.025	3	0.050	0.495	0.056
Future 1	3000	500	100	4	222.2	39.04	3	0.018	0.072	0.010	15	0.090	1.800	0.262
			150	4	205.1	38.36	3	0.013	0.035	0.005	15	0.065	0.867	0.121
Future 2	7500	500	150	4	205.1	25.97	3	0.013	0.035	0.011	15	0.065	0.867	0.264
			200	4	190.5	25.78	3	0.011	0.021	0.006	15	0.053	0.525	0.150

Length of supplying and retrieving lines is another important factor to be precisely controlled to reduce pressure drop at the microchannel. One of most different factor between previous channel [Figure 2-5] and current channel [Figure 4-1] is length of supplying and retrieving lines, bringing out the failure of current channel design. Long supplying/retrieving lines require tremendous pressure for fluid to flow without improvement for separation efficiency. High pressure loaded on the microchannel make damage on the bonding of microchannel. From the equation derived from simple circuit analogy model [Figure 4.5], it is reveals that length of supplying lines does not affect to amount of separation performance. Accordingly, the shorter length the supplying lines has, the better the design is. However, length of retrieving lines has something to do with its enrichment. Asymmetric length of retrieving lines which inner one is longer than outer could result in better enrichment of fluid collected at the outlet of inner lane. By increasing resistance of the channel, flow can search other path to reduce their energy, resulting in more transfer of water to outer lane. All design was same except the length of retrieving lines. [Figure 6-3] represent an example of it. If inner lane is elongated to 5 cm from 3 cm and outer lane is shorten to 1 cm from cm, the fluid volume ratio collected on each outlet is enhanced to 26 from 7. Strong suction of fluid might result

in more particle transfer. [Figure 6-4] demonstrates pressure distribution estimated by circuit theory for the geometric condition of future 1 on the [Table 6-2], enlarged channel with similar microfluidic characteristics. Circuit analogy method represent that maximum pressure drop loaded is around 1.93 bar, volume collected ratio is estimated to 10.7. All of indicator for particle separation is better than that of current design.

(A)



(B)

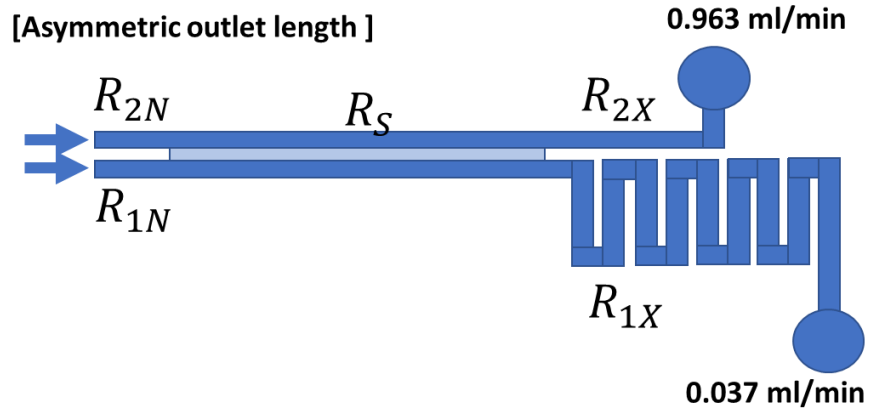


Figure 6-3 Symmetric and asymmetric retrieving lines

(A) pattern has 3 cm of retrieving lines, respectively while (B) pattern has 1 and 5 cm of outer and inner retrieving lines, respectively. Upper lane is determined as outer lane and lower one is done as inner lane.

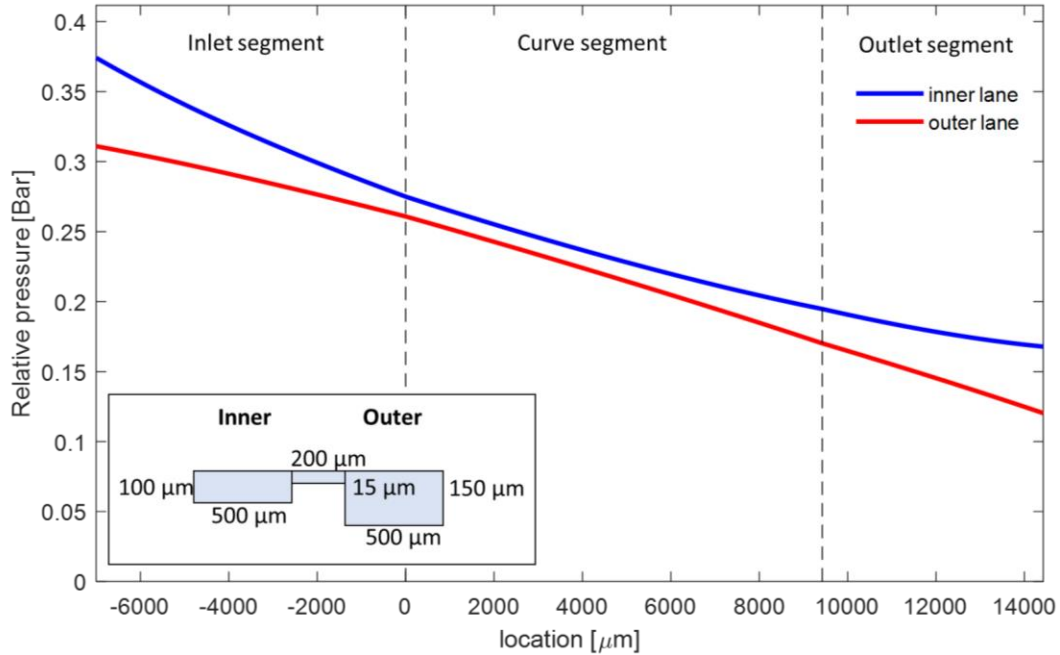


Figure 6-4 Graph for pressure distribution for enlarged channel

Inset represents geometric parameter for cross-section of the channel, radius of curvature is 2000 μm and flow-rate is 4 ml/min. Inlet and outlet length of filtration part is 5 and 7 mm. Length of supplying line for outer inlet, inner inlet, inner outlet and outer outlet is 3 cm, 3 cm, 5 cm and 10 cm, respectively. This channel has similar microfluidic characteristics compared to current channel design: such as Dean number, Reynolds number and particle Reynolds number. See Future 1 row of [Table 1.6] Maximum pressure difference is 0.0665 bar. Pressure drop along lane is 0.1807 bar. Total length of filtration part is 18 mm and width of the channel is 1.2 mm

An alternative new design concept is only employing straight filtration. According to the simulation results, more than half separation had already taken place in the straight channel, suggesting that an improved design with a straight channel could be enough for high separation efficiency. The reason why a straight channel is not solely employed is that particles locate away from the bridge, due to the absence of forces in the secondary direction. Flow suction near the narrow bridge affects flow streamline only in its vicinity, resulting in low separation efficiency. So, secondary flow is mandatory to allow particles to migrate near and then across the bridge between channels. New design concept #2 [Figure 6-5] makes enhanced separation possible by

shrinking the first lane where the particles are injected, thus generating secondary flow in the straight channel. Also, it is expected that shrinking the first lane while broadening the second lane continue to keep pressure difference, yielding high separation efficiency.

The other alternative idea is below. Curved segments are designed to increase particle encounters with the bridge by placing a spiral channel upstream to first produce inertial focusing of large particles, followed by a curved weir-filtration segment where vortices still remain and enhance separation of smaller particles [Figure 6-6].

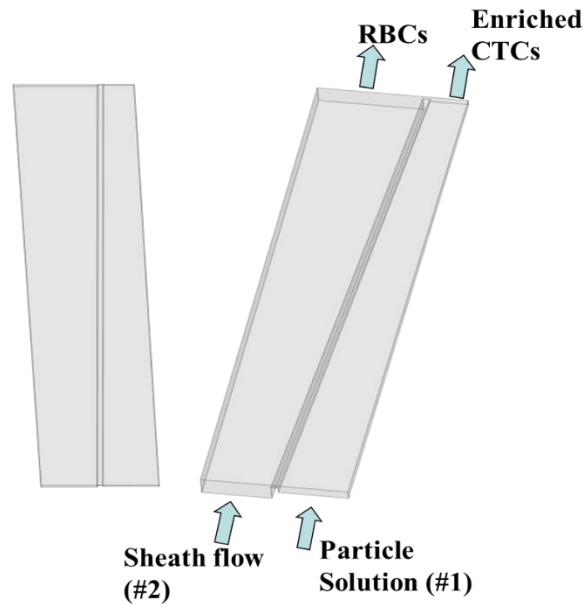


Figure 6-5 Schematic diagram of new design for a separation device employing slanted straight channel

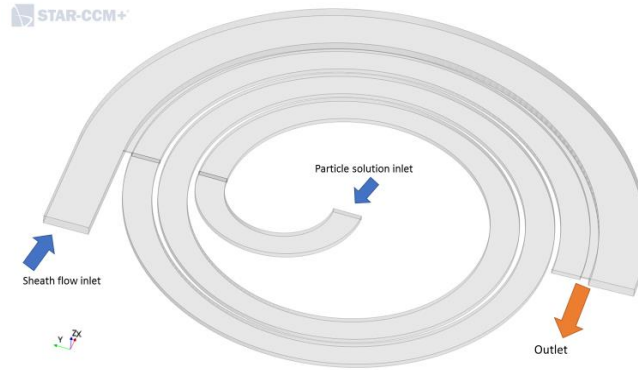


Figure 6-6 New device design to take advantage of inertial focusing

Large particles get focused at the inner side of the spiral lane while small particles remain rotating and start to migrate to the other lane once the two lanes become parallel and connected by a bridge.

6.3 Improvement of channel fabrication

6.3.1 Re-bonding channel by solvent bonding with groove

One of improving method for solvent bonding is making groove near channel [Figure 6-7]. It is not easy to reorder new micro-milled channel in this point, requiring spending time and money. However, we already have some channels with groove for silicon gasket, usually UV adhesive is applied for bonding. By removing UV adhesive and silicon gasket, we can get well micro-milled channel with groove. We can try solvent bonding with uncovered channel. [Figure 6-8] demonstrates grooves covering fluid path.

It would be many different compared to company's work. Temperature annealing is very important on solvent bonding[86] but there was no information on company's note. Pressure applied is lower than paper suggestion. Also, while paper recommend using mixture of 2- propanol and cyclohexane, Company's note has only 2-propanol and ethynol. Most of all, groove for solvent bonding is not observed on company's design.

Paper's recommendation is followed. To get solvent bonding for COP (glass transition temp. 102 °C), 65:35 mixture of 2-propanol and cyclohexane are dropped on the surface. Apply 350 kPa pressure and increase the temperature from 25 °C to 70 °C at a rate of 5 °C/min. After reaching 70 °C (after 9 min), bond for an additional 15 min. place bonded device on hotplate and bake at 45 °C for 24 hr to remove any remaining cyclohexane [85, 89].

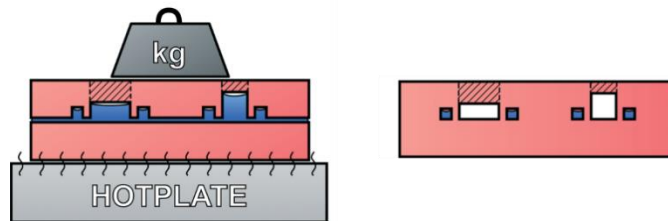


Figure 6-7 Schematic illustration for solvent bonding with groove

Reprinted from ref.[89] Wan with permission

For conducting this works. We need to search below information and get some device.

1. Though UV adhesive is well peeled off even in by hand, some of debris could remained on the plate. Remover for UV adhesive but not damage to COP polymer should be employed. Air or other gas compressor might be employed for cleaning debris.

2. Material of channel we have is made of COP-1420R (Zeonex). We need extra COP block for practicing new cover. Its glass transition temperature is 136 °C. COP plate can be made by pressing COP resin on mold by pressing machine with heater (156 °C). Or, we can also order molded block/plate.

3. Pressing machine with heater is mandatory for solvent bonding. Wooden block with hole can cover channel with tips to deliver pressure evenly. There is pressing machine in Dr. Jeong's lab. However, they don't have heating function. Check machine shop or other labs.

4. Many practice of solvent bonding should be conducted before actual channel is employed. We can make hole and large path on COP block. Well bonded channel might be employed for measuring bonding strength

5. Let's check there is 2-propanol, cyclohexane and glass pipette on lab

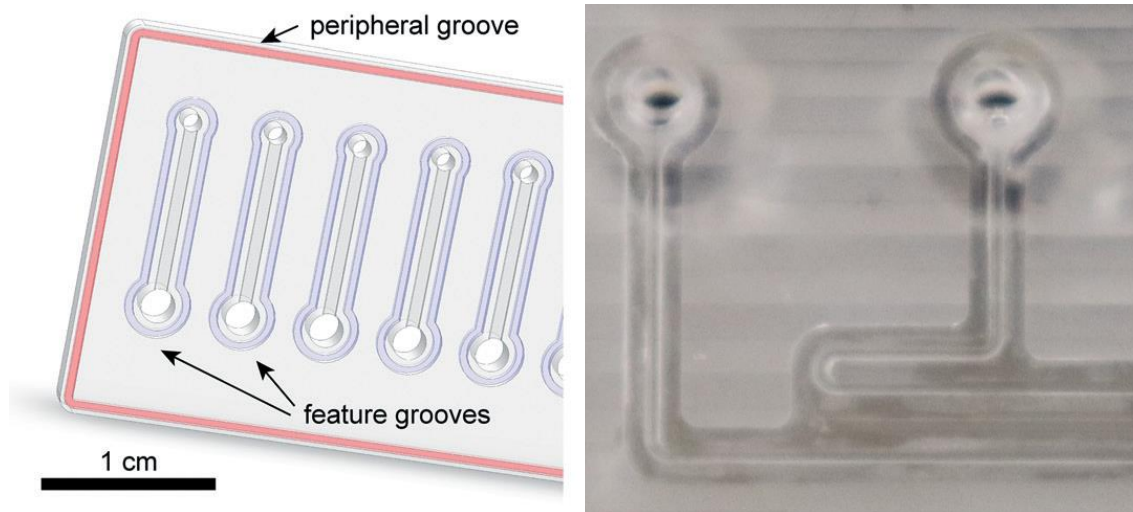


Figure 6-8 Groove in the channel

Left, Reprinted from ref.[89] Wan with permission, Feature groove along fluid path and peripheral groove along the edge of channel is suggested for good solvent bonding Right. Magnified top view image for uncovered A15 channel. Darkest part is the groove surrounding weir and fluid path. Horizontal pattern on the channel is UV adhesive coated on the surface. The UV adhesive on the cover was well peeled off by a little force by hand. It is not tested to the body.

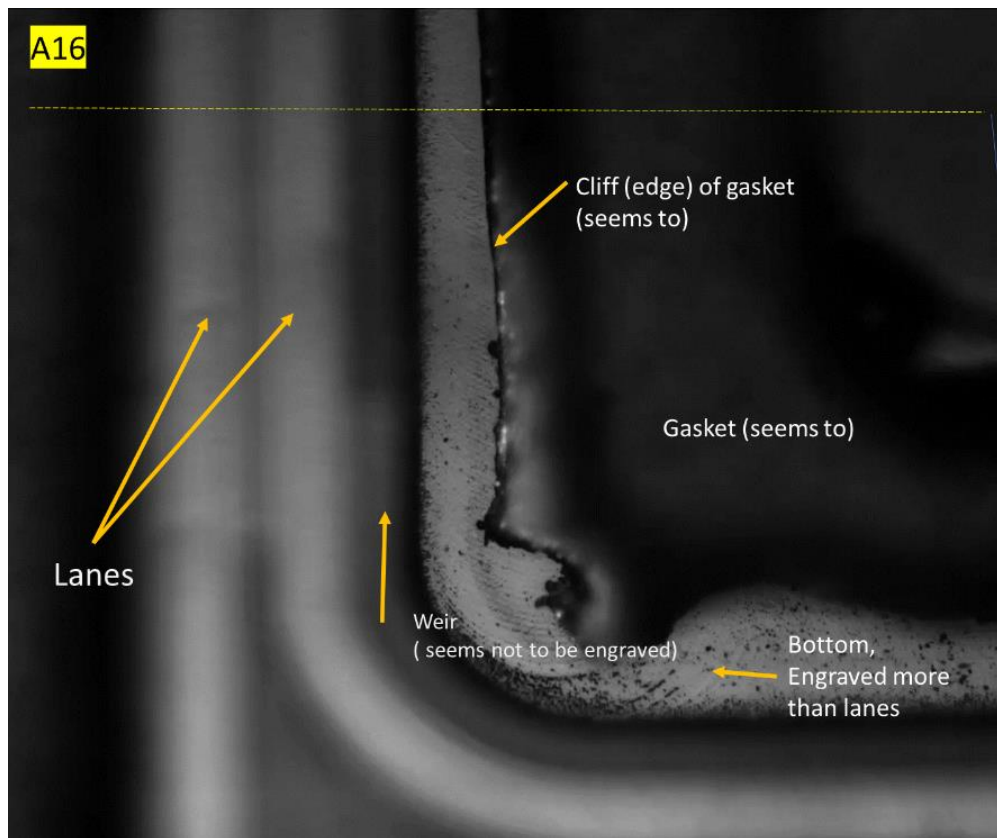
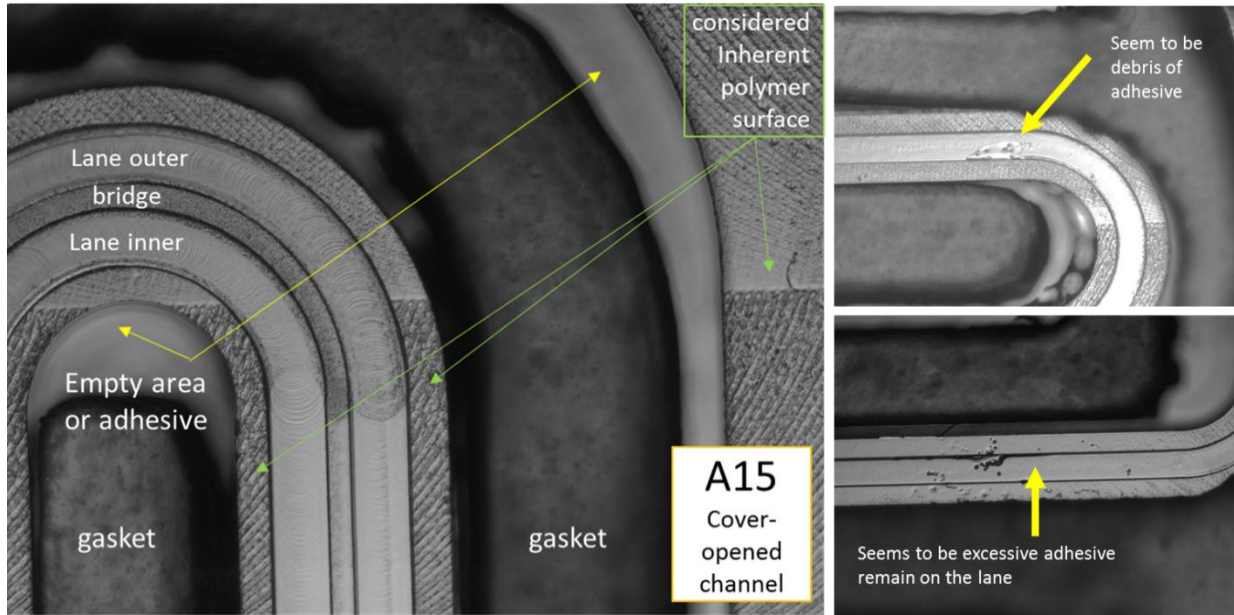


Figure 6-9 Existence of groove for gasket
 Channel A16, Groove is deeper than any other lane

6.3.2 Pseudo greyscale photomask

To make multi-level structures of master mold for microchannel, ordinary photolithography should be performed repeatedly with exact alignment, requiring complicated steps and lots of time. However, backside diffused light lithography can help us to make multi-level structure in one step. UV light exposed on negative photoresist SU-8 through transparent substrates can generate crosslink between photoresist and substrates, enabling well-defined master mold for PDMS channel. Height of master-mold is determined by total amount of energy exposed to substrate coated with SU-8 [Figure 6-10]. Binary patterns of transparent/opaque square could produce different level of light, acting as filter. Light passing small hole are diffracted and spread to the photoresist, enabling even but reduced amount of exposure. Photo plotter is commonly employed to print making mask. Plotter resolution could be up to 50,800 dpi with minimum resolution of 7 μm [photoplotstore.com, \$135/100 square inches]. Similarly, width of slit on photomask also bring out different height of master mold [Figure 6-11, left]. Glass[90] or PET film[91] can be employed as substrates. Spin coater is located at MCF in GURB. Uneven SU-8 coating without spin coater can be employed because surface of coating where light is exposed is flat [90]. Photomask depicted in [Figure 6-11, right] is exemplary for our design.

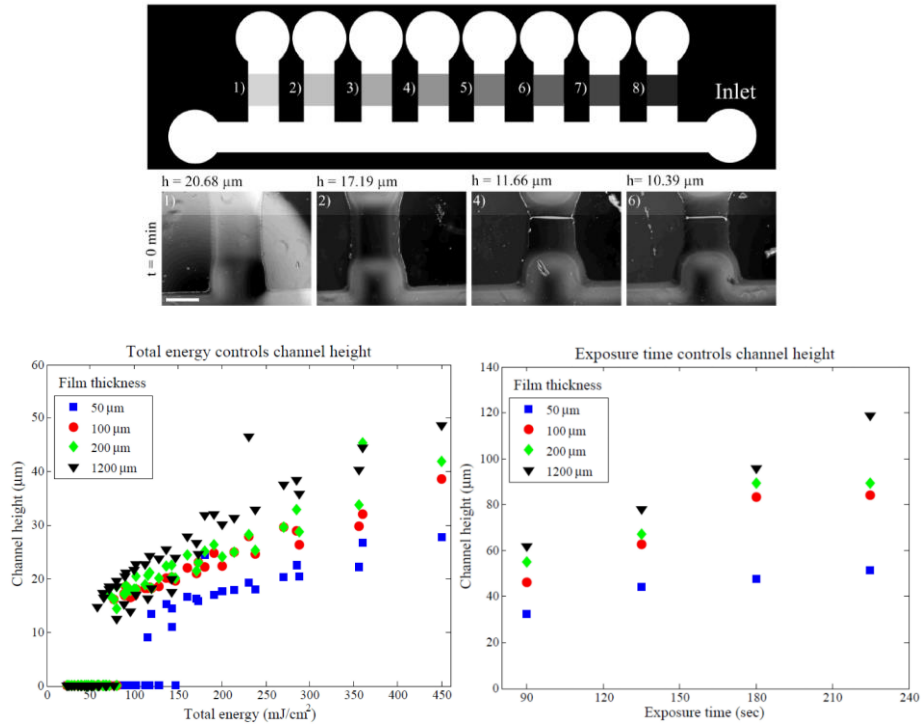


Figure 6-10 Fabrication of multi-level master mold using greyscale photomask

Upper represents height different in terms of brightness of photomask. Lower two grapes show height of master mold relation to total energy, thickness of photoresist and exposing time. Reprinted from ref.[90] Lai with permission

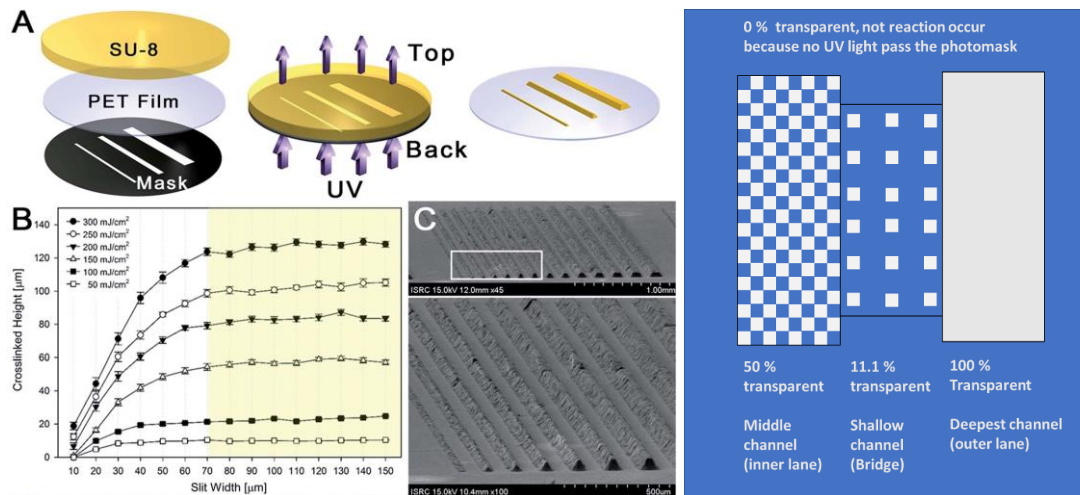


Figure 6-11 Multi-level microstructure with slit mask

Left, Reprinted from ref.[91] Kang. Right, prototype of greyscale photomask

6.4 Multiple enrichment stages for CTCs

6.4.1 Overview for future experiments

The ultimate goal of the project is to collect and enrich CTCs from human blood to later identify them using an interference-based label-free imaging technology. Considering image processing throughput: a time scale of one second is required to acquire each image, and approximately 10 particles are located within a single image. Therefore, if 1,000 images can be collected from cells dispersed inside a single imaging chamber (requiring a total time of approximately 17 min), the total number of all cells in the CTC enriched solution should not exceed ten thousand. Additionally, to ensure reliability of identification, at least 10 CTCs should be collected and observed in each imaging chamber. Assuming volume of the imaging chamber as 10 μl , concentration of the solution injected into the chamber should be at least 1 CTCs/ μl to fulfill the number of 10 CTCs in the chamber. It required at least 50-fold concentration relative to the 5-fold diluted blood solution (assumed based on previous experiments) with 0.02 CTCs/ μl during the process.

In summary, our isolation and enrichment target should be (1) achievement of a 1:1000 ratio between CTCs and other cells [E6-1]; (2) minimum concentration to fulfill at least 10 CTCs in the imaging chamber, equivalent to 50-fold relative to 5 fold diluted blood solution [E6-2]; and (3) the total number of cells in the imaging chamber should not account for more than 10 % of the surface area at the bottom so that all cells can be viewed [E6-3]. The NL can be interpreted as concentration of other cells and would be the function of ER and ES.

$$\text{ER} \sim 100 \quad [\text{E6-1}]$$

$$(\text{ES}_{\text{CTC}})^N > 50 \quad [\text{E6-2}]$$

$$\text{NL} < 0.1 \quad [\text{E6-3}]$$

In the above equations, ER is the enrichment ratio [E6-8], ES is the single enrichment factor [E6-5] and NL is the number of layer on the bottom [E6-7] Future plans will be directed toward designing the cell separation system to achieve these targets. N is the number of stages.

6.4.2 Enrichment calculation

Multiple separation stages can be arranged in series to achieve desired enrichment levels. The enrichment factor at each stage (ES) is estimated as the ratio of concentrations after/before a given stage. Concentration is calculated by the number of particles divided by volume of solution. Assuming the number of particles as X and the volume of solution as Y in the before-stage, the number of particles in the after-stage X' can be calculated by employing the separation efficiency (SE) as follows [E6-4], in the numerator]. The transferred solution ratio is defined as the volume of solution transferred to outer lane outlet divided by the volume of sample injected. The volume of solution in the after-stage Y' is determined by TR and Y [E6-4], in the demoninator]. Both SE and TR can be measured by either experiment or simulation, enabling the enrichment factor at a single stage (ES) to also be evaluated by either experiment or simulation [E6-5].

$$\frac{X'}{Y'} = \frac{(1 - SE) \cdot X}{(1 - TR) \cdot Y} \quad [E6-4]$$

$$ES = \frac{X'}{Y'} \bigg/ \frac{X}{Y} = \frac{(1 - SE)}{(1 - TR)} \quad [E6-5]$$

When multiple stages will be employed for separating RBCs and WBCs from blood and enriching CTCs, the final enrichment factor (EF) can be straightforwardly estimated from the power of enrichment factor at a single stage (ES) as follows, where n is the total number of stages [E6-6].

$$EF = ES^N \quad [E6-6]$$

Here, N is the number of stages. Therefore, the total enrichment factor at the final stage for RBCs, WBCs and CTCs can be calculated. In whole blood, the concentration of RBCs, WBCs and CTCs are 5×10^9 , 1×10^7 and 100 cells per milliliter. Previous experiments employed a 5-fold dilution before using, although dilution may not be necessary. Previous experiments by Huang using this device design reported separation efficiencies of RBCs, WBCs, and CTCs to be 0.5, 0.05 and 0, respectively (CTC separation of 1% is ignored for simplicity), and a transferred solution ratio (TR) of 0.5 (6 ml of solution is injected, and 3 ml of solution transferred to the outer lane). Thus, single-stage enrichment factors of 1, 1.9, and 2 were attained for RBCs, WBCs and CTCs, respectively.

To achieve the target concentration of CTCs (10 CTCs in the 10 μ l imaging chamber), a final enrichment factor (EF) for CTCs of 50 is required, which can be achieved by using 6 stages (exactly 5.65 stages) of the current device design.

Although this is good performance in terms of CTC concentration, it should be noted WBCs will also be concentrated by nearly the same amount (ES = 1.9 for WBCs, compared with 2.0 for CTCs) and RBCs keep its high concentration (RBCs have ES = 1 at each stage) [E6-5]. Thus, concentration of RBCs and WBCs exceed their allowed maximum concentration, expressed as the number of layers (NL) in the imaging chamber. NL is estimated by dividing sum of cross section area of all cells by surface area of the imaging chamber [E6-7]. Assuming that all particles in the chamber are deposited at its bottom, this parameter expresses how many layers are formed on the chamber floor.

$$NL = \frac{(\# \text{ of total particles in the volume}) \times (\text{Cross section area of a cell})}{\text{Surface area of the imaging chamber floor}} \quad [E6-7]$$

Because we need to take a photo of the bottom of the imaging chamber, the sum of all layers should be less than unity; precisely, sum of cross-section of cells are supposed to account less than

10 % of surface area of the imaging chamber. After 6 stages, however, NL of RBCs is 2.42 and for WBCs is 2.99 based on the imaging chamber with volume of 10 μl and surface area of its floor of 13 mm^2 (1000 shots multiplied by area of single shot of 100 μm x 130 μm) [Table 6-3]. It means that too many RBCs and WBCs still remained on the concentrated solution. For optimal performance, CTCs must be isolated from both WBCs and RBCs. It would be best to find out the geometry condition that the ES for RBCs and WBCs is lower than unity. In this case, concentration of RBCs and WBCs are diluted while concentration of CTCs is increased. Stages with different bridge heights can be employed to further separate WBCs from CTCs.

Although not ideal for CTC separation, we also considered separation performance using only the current design where RBCs and CTCs have ES greater than unity [Figure 6-12]. First, concentration ratio should be defined by the ratio of the number of CTCs to the number of other cells. Then, the total enrichment ratio (ER) is only dependent on separation efficiency of cells, assuming CTCs are perfectly separated [E6-8]. If we assume total number other cells in the imaging chamber is 10000 including at least 10 CTCs, enrichment ratio between CTCs and other cells should be 1:10³. If the total enrichment ratio is near 1:10³, concentration of CTCs can be controlled by diluting or concentrating of the solution collected, not affecting to enrichment ratio. [Figure 6-13] demonstrates the number of stages required for achieving total enrichment ratio in terms of separation efficiency. Examples of multiple stages enrichment process are summarized in [Table 6-4]. Case 4 of [Table 6-4] demonstrates multi-stage enrichment by the device tested in section 4. It works for 10²-fold enrichment of Cells/CTCs. however, 10⁵-fold enrichment needs additional diluting or concentrating of solution to achieve the goal.

$$ER = \frac{CR_N}{CR_0} = \left(\frac{ES_{CTCs}}{ES_{Cells}} \right)^N = \left(\frac{1}{1 - SE_{Cells}} \right)^N \quad [E6-8]$$

In conclusion, the device we have works for separation and enrichment of CTCs/RBCs though it might need diluting and concentrating. However, some combination of modification to the device design to further isolate WBCs, reduction in the whole blood dilution factor, and re-sizing of the imaging chamber can optimize performance for CTC isolation.

Table 6-3 Evaluation of the number of layers in the image channel (NL)

Cells	RBC	WBC	CTC
Transferred solution ratio (TR)	0.5	0.5	0.5
Separation efficiency (SE)	0.5	0.05	0
Enrichment factor at a stage (ES)	1	1.9	2
Diameter [μm]	8	10	20
Cross sectional area of a particle [μm^2]	50.3	78.5	314
Surface area of the imaging chamber [mm^2]	13	13	13
Whole blood	193.33	0.6042	2.42E-05 (0.02)
5-fold dilution	38.67	0.1208	4.83E-06 (0.04)
# of layers in the imaging chamber (the figures in the blanket refers concentration, unit of cells/ μl)	1 stage	38.67	9.67E-06 (0.08)
	2 stages	38.67	1.93E-05 (0.16)
	3 stages	38.67	3.87E-05 (0.32)
	4 stages	38.67	7.73E-05 (0.64)
	5 stages	38.67	1.55E-04 (1.28)
	6 stages	38.67	3.09E-04 (2.56)

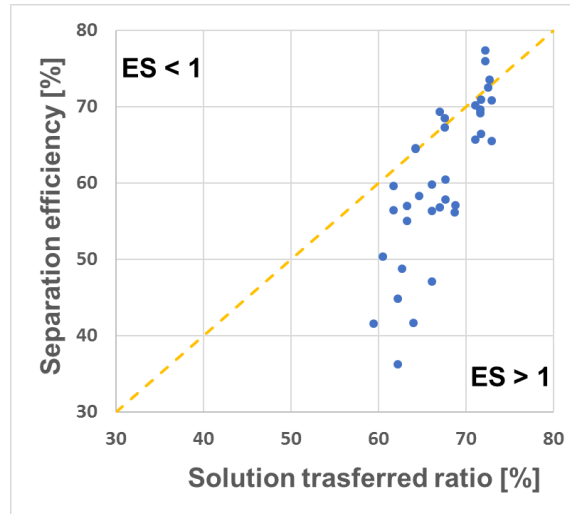


Figure 6-12 Separation efficiency and solution transferred ratio

Blue dots are simulation results conducted in section 3. Yellow dash line means value of SE and TR is identical so that ES becomes unity. Upper triangle is the region that concentration of particle/cells in the solution collected are decreased while lower triangle is one that concentration is increased after the stage.

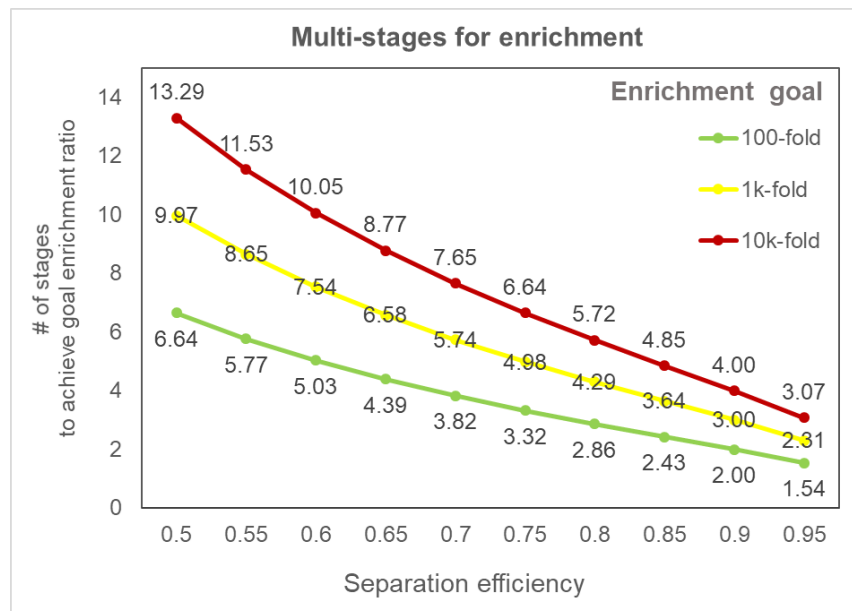


Figure 6-13 Graph for the number of stage required for the goal of enrichment ratio

The graph demonstrates how many stage is required for the goal enrichment in terms of separation efficiency. For instance, at least 5.74 stages are required to achieve 1×10^3 -fold total enrichment ratio of CTCs/other cells by using the device with 70% separation efficiency.

Table 6-4 Examples of multi stages CTCs enrichment.

		0 th	1 st	2 nd	3 rd	4 th	5 th	...	SE	TR	ES
(1)	Concentration ratio btw WBCs/CTCs	1.00E5	9.50E4	9.03E4	8.57E4	8.15E4	7.74E4	(...90 th) 9.9E2	0.050	0.500	1.900
	The number of CTCs in 10 μ l	0.20	0.40	0.80	1.60	3.20	6.40	2.48E26			
	NR - WBCs (13 mm ² *770 μ m)	0.121	0.230	0.436	0.829	1.575	2.992	1.48E+24			
(2)	Concentration ratio btw WBCs/CTCs	1.00E5	5.50E4	3.03E4	1.66E4	9.15E3	5.03E3	(... 8 th) 8.37E2	0.450	0.700	1.833
	The number of CTCs in 10 μ l	0.20	0.67	2.22	7.41	24.69	82.30	3.05E3			
	NR - WBCs (13 mm ² *770 μ m)	0.121	0.222	0.406	0.745	1.365	2.503	15.42			
(3)	Concentration ratio btw WBCs/CTCs	1.00E5	2.26E4	5.12E3	1.16E3	2.62E2	5.92E1		0.774	0.722	0.812
	The number of CTCs in 10 μ l	0.20	0.72	2.58	9.26	33.25	119.37	-			
	NR - WBCs (13 mm ² *770 μ m)	0.121	0.098	0.080	0.065	0.053	0.043				
(4)	Concentration ratio btw WBCs/CTCs	1.00E5	3.22E4	1.04E4	3.34E3	1.08E3	3.46E2		0.678	0.750	1.288
	The number of CTCs in 10 μ l	0.20	0.80	3.20	12.80	51.20	204.80	-			
	NR - WBCs (13 mm ² *770 μ m)	0.121	0.156	0.200	0.258	0.333	0.428				

Initial concentration of cells and CTCs are assumed 1×10^7 cells/ml and 100 CTCs/ml, respectively. So, goal becomes 100-fold enrichment ratio between cells and CTCs. Whole blood is 5-fold diluted before enrichment processing. (1) The device by Huang and 5% of separation efficiency for WBCs is employed. The goal, which is 1 to 1000 enrichment ratio of CTCs/cells and at least 10 CTCs in the imaging chamber of 10 μ l is achieved after 45 stages. However, it must require dilution during the process due to many stages (2) one possible device. It requires 8 stages to reach the goal. However, it also requires dilution during the process. The device with higher SE and lower ES is required for realistic process. (3) The device with best SE and ES among simulation results conducted in the section 3: Separation efficiency of RBCs is employed: Particle size of 2 μ m, inlet length of 1000 μ m, Radius of curvature of 500 μ m and flow-rate of 0.5 ml/min. The final enrichment ratio is attained after 4 stages. No dilution or concentration is required for the imaging processing. Because it is the case of $ES < 1$, no dilution or concentration is required for higher enrichment i.e. 1×10^5 -fold enrichment. (4) The device used in the experiment in section 4 is employed. Separation efficiency of RBCs is employed. The goal is completed after 5 stages. Concentration of cells and the number of CTCs satisfy the criteria. ($NR < 0.1$, and # of CTC is more than 10). However, because it is the device with $ES > 1$, Dilution or concentration might be required for higher enrichment ratio. See stage 10 in the case (4)

6.4.3 Design of multi stage enrichment systems

As a first step for optimization toward CTC analysis, the injected blood solution should be enriched for CTCs from other cells [Figure 6-14]. Multiple stages will be required to achieve the target enrichment level, with buffer possibly added to replace transferred fluid during each stage (biased injection of solution near the bridge due to buffer injection may also increase separation efficiency by increasing encounters with the bridge). To guarantee at least 10 CTCs in the imaging chamber, the concentration of CTCs should be increased at least 50-fold during entire process (assuming whole blood has a concentration of 100 CTCs/ml and it is 5-fold diluted at the beginning), the number of CTCs in the imaging chamber of 10 μ l would be 0.2 CTCs) [Figure 6-15]. Performance can be estimated by multiplying all TR values at each stage. Subsequent injection into the imaging chamber [Figure 6-15] will be achieved by a squeezing chamber where the concentration of CTCs in solution is increased to satisfy at least 50-fold concentrated concentration compared to diluted blood solution, essential for at least 10 particles in the imaging chamber. Parallel lanes with the bridge connecting each other can be employed to squeeze solvent. The bypass of flow which has smaller size than CTCs can also suck solvent, and thus increase concentration of CTCs in solution. The blood suspension containing CTCs will then flow into the imaging chamber, which could include an integrated valve and bypass.

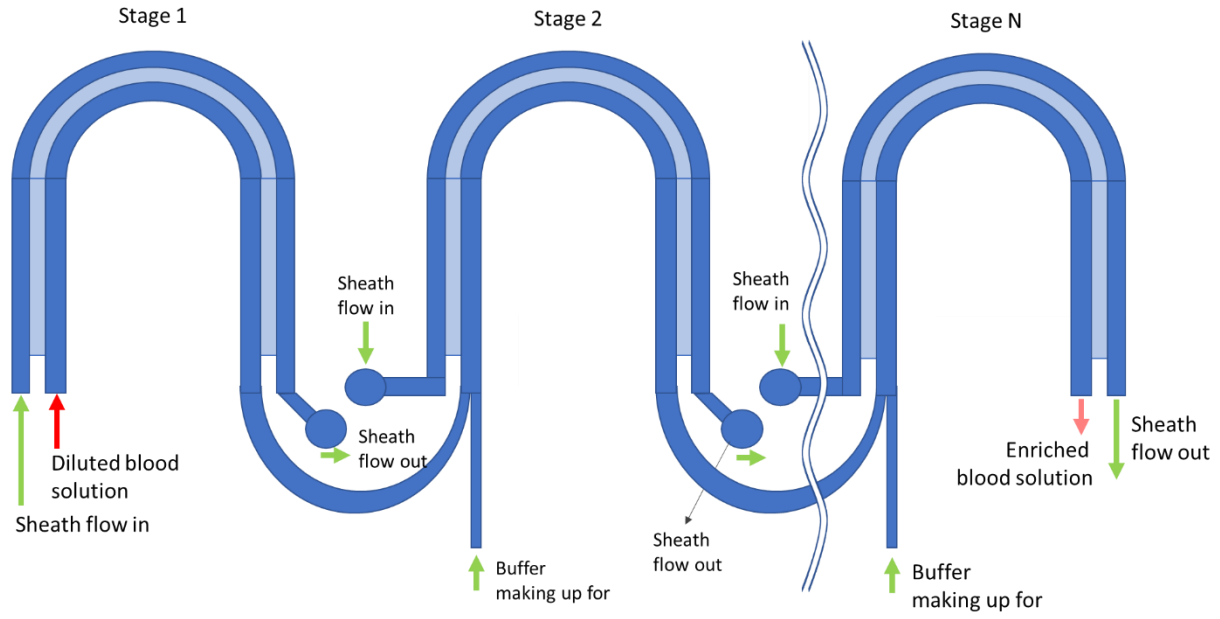


Figure 6-14 Diagram of multi-stage enrichment

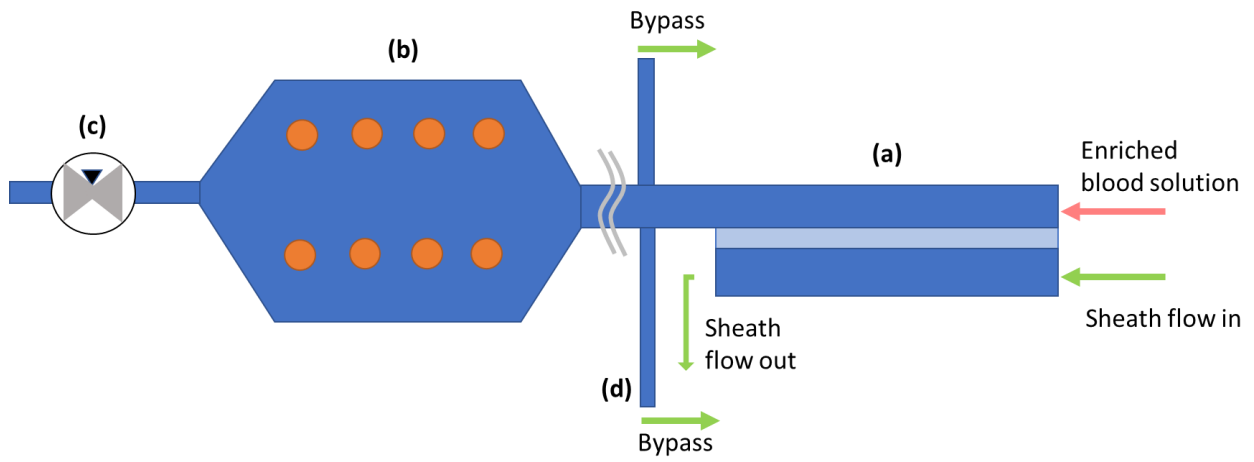


Figure 6-15 Diagram of squeezing solution and the imaging chamber

6.5 Experiment plan

One urgent task to be performed would be conducting experiments of quasi-inertial focusing in curved segments to verify our simulation results. The model used in this simulation has some difference compared to existing theories. Conventional studies explained particles' behavior in a curved microchannel as the balance of secondary Dean drag force and shear-gradient-induced lift force with shear gradient effect. However, even though the Saffman lift force, which omits shear gradient effect and is one order of magnitude smaller than the shear-gradient-induced lift force [92, 93], is solely employed, some inertial focusing is observed in our simulation. Therefore, comparison between experimental and simulations results will determine whether shear-gradient-induced lift force should be considered in the simulation. Also, our simulation results that Saffman lift force makes particles cross streamlines and switches their path could offer a better explanation for inertial focusing in curved channels, as opposed to the fact that many papers consider Saffman lift force to be so small and ignore it [50]. So, verifying our model is critical.

Experimental verification methods should not be difficult to implement. For simplicity, only a single spiral PDMS channel of equal height could be custom made and fabricated, and a solution of florescent particles injected into this channel would reveal the existence of inertial focusing. In addition, the continuous change of the radius of curvature in a spiral channel makes it easier to find out when quasi-inertial focusing starts to be generated. If inertial focusing is not observed, we then go to step two. A device with two-parallel curvilinear channels will be tested for the presence of inertial focusing, revealing if secondary flow due to different pressure between the parallel channels has a critical role for this inertial focusing to occur. In the case that both experiments could not reproduce the inertial focusing behavior observed in simulations, there would be two possible conclusions. First, there is a possibility that inertial focusing is negligible in our separation

design. Only drag force would be an important factor. Or, a new model such as shear-gradient-induced lift force is needed for the simulations.

REFERENCES

1. Shields, C.W.t., C.D. Reyes, and G.P. Lopez, *Microfluidic cell sorting: a review of the advances in the separation of cells from debulking to rare cell isolation*. Lab Chip, 2015. **15**(5): p. 1230-49.
2. Warkiani, M.E., et al., *Ultra-fast, label-free isolation of circulating tumor cells from blood using spiral microfluidics*. Nat Protoc, 2016. **11**(1): p. 134-48.
3. Xiang, N. and Z. Ni, *High-throughput blood cell focusing and plasma isolation using spiral inertial microfluidic devices*. Biomed Microdevices, 2015. **17**(6): p. 110.
4. Rafeie, M., et al., *Multiplexing slanted spiral microchannels for ultra-fast blood plasma separation*. Lab on a Chip, 2016. **16**(15): p. 2791-2802.
5. Ozbey, A., et al., *Inertial Focusing of Microparticles in Curvilinear Microchannels*. Sci Rep, 2016. **6**: p. 38809.
6. Zhang, J., et al., *High throughput extraction of plasma using a secondary flow-aided inertial microfluidic device*. RSC Advances, 2014. **4**(63): p. 33149-33159.
7. Mach, A.J. and D. Di Carlo, *Continuous scalable blood filtration device using inertial microfluidics*. Biotechnol Bioeng, 2010. **107**(2): p. 302-11.
8. Bhagat, A.A.S., S.S. Kuntaegowdanahalli, and I. Papautsky, *Inertial microfluidics for continuous particle filtration and extraction*. Microfluidics and Nanofluidics, 2008. **7**(2): p. 217-226.
9. Hur, S.C., A.J. Mach, and D. Di Carlo, *High-throughput size-based rare cell enrichment using microscale vortices*. Biomicrofluidics, 2011. **5**(2): p. 22206.

10. Huang, J.-H., A. Jayaraman, and V.M. Ugaz, *Enzymatic Sculpting of Nanoscale and Microscale Surface Topographies*. Angewandte Chemie International Edition, 2012. **51**(38): p. 9619-9623.
11. Bhagat, A.A.S., et al., *Pinched flow coupled shear-modulated inertial microfluidics for high-throughput rare blood cell separation*. Lab on a Chip, 2011. **11**(11): p. 1870-1878.
12. Lashgari, I., et al., *Inertial migration of spherical and oblate particles in straight ducts*. Journal of Fluid Mechanics, 2017. **819**: p. 540-561.
13. Kim, J., et al., *Inertial focusing in non-rectangular cross-section microchannels and manipulation of accessible focusing positions*. Lab Chip, 2016. **16**(6): p. 992-1001.
14. Liu, C., et al., *Inertial focusing of spherical particles in rectangular microchannels over a wide range of Reynolds numbers*. Lab Chip, 2015. **15**(4): p. 1168-77.
15. Amini, H., et al., *Intrinsic particle-induced lateral transport in microchannels*. Proceedings of the National Academy of Sciences, 2012. **109**(29): p. 11593-11598.
16. Nivedita, N., P. Ligrani, and I. Papautsky, *Dean Flow Dynamics in Low-Aspect Ratio Spiral Microchannels*. Sci Rep, 2017. **7**: p. 44072.
17. Keinan, E., E. Ezra, and Y. Nahmias, *Opposing shear-induced forces dominate inertial focusing in curved channels and high Reynolds numbers*. Applied Physics Letters, 2015. **107**(19): p. 193507.
18. Guan, G., et al., *Spiral microchannel with rectangular and trapezoidal cross-sections for size based particle separation*. Sci Rep, 2013. **3**: p. 1475.
19. Ligrani, P.M. and R.D. Niver, *Flow visualization of Dean vortices in a curved channel with 40 to 1 aspect ratio*. The Physics of Fluids, 1988. **31**(12): p. 3605-3617.

20. Sugiyama, S., T. Hayashi, and K. Yamazaki, *Flow Characteristics in the Curved Rectangular Channels : Visualization of Secondary Flow*. Bulletin of JSME, 1983. **26**(216): p. 964-969.
21. Dean, W.R., *XVI. Note on the motion of fluid in a curved pipe*. The London, Edinburgh, and Dublin Philosophical Magazine and Journal of Science, 1927. **4**(20): p. 208-223.
22. Dean, W.R., *LXXII. The stream-line motion of fluid in a curved pipe (Second paper)*. The London, Edinburgh, and Dublin Philosophical Magazine and Journal of Science, 1928. **5**(30): p. 673-695.
23. Berger, S.A., *Flow in Curved Pipes*. Annual Review of Fluid Mechanics, 1983. **15**(1): p. 461-512.
24. Ookawara, S., et al., *Feasibility study on concentration of slurry and classification of contained particles by microchannel*. Chemical Engineering Journal, 2004. **101**(1-3): p. 171-178.
25. Sudarsan, A.P. and V.M. Ugaz, *Fluid mixing in planar spiral microchannels*. Lab Chip, 2006. **6**(1): p. 74-82.
26. Seo, J., M.H. Lean, and A. Kole, *Membraneless microseparation by asymmetry in curvilinear laminar flows*. J Chromatogr A, 2007. **1162**(2): p. 126-31.
27. Bhagat, A.A., S.S. Kuntaegowdanahalli, and I. Papautsky, *Continuous particle separation in spiral microchannels using Dean flows and differential migration*. Lab Chip, 2008. **8**(11): p. 1906-14.
28. Zhang, J., et al., *Inertial particle separation by differential equilibrium positions in a symmetrical serpentine micro-channel*. Scientific Reports, 2014. **4**: p. 4527.

29. Ha, B.H., et al., *Three-dimensional hydrodynamic flow and particle focusing using four vortices Dean flow*. *Microfluidics and Nanofluidics*, 2014. **17**(4): p. 647-655.
30. Deen, W.M., *Analysis of transport phenomena*. 2nd ed ed. Topics in chemical engineering. 2011, New York: Oxford University Press
31. Stokes, G.G., *On the Effect of the Internal Friction of Fluids on the Motion of Pendulums*. *Transactions of the Cambridge Philosophical Society*, 1851. **9**: p. 8.
32. Deen, W.M., *Analysis of transport phenomena*. 2nd edition ed. 2011: Oxford University Press, USA.
33. Sommerfeld, M., *Theoretical and Experimental Modelling of Particulate Flow*. V.K.I. for Fluid Mechanics, 2000. **2000-2006**: p. 1-62.
34. Basset, A.B., *On the Motion of a Sphere in a Viscous Liquid*. *Philosophical Transactions of the Royal Society of London*. (A.), 1888. **179**: p. 43-63.
35. Boussinesq, J., *theorie analytique de la chaleur*. Vol. 2. 1903, Paris: L'Ecole Polytechnique.
36. Oseen, C.W., *Hydrodynamik*. 1927: Leipzig.
37. Parmar, M., A. Haselbacher, and S. Balachandar, *Generalized Basset-Boussinesq-Oseen equation for unsteady forces on a sphere in a compressible flow*. *Phys Rev Lett*, 2011. **106**(8): p. 084501.
38. Soo, s.L., *Multiphase Fluid Dynamics* 1990: Butterworth-Heinemann
39. Tchen, C.M., *Mean value and correlation problems connected with the motion of small particles suspended in a turbulent fluid*
in *Civil Engineering and Geosciences*. 1947.
40. Maxey, M.R., *Equation of motion for a small rigid sphere in a nonuniform flow*. *The Physics of fluids*, 1983. **26**(4): p. 883-889.

41. Loth, E. and A.J. Dorgan, *An equation of motion for particles of finite Reynolds number and size*. Environmental Fluid Mechanics, 2009. **9**(2): p. 187-206.
42. Faxén, H., *Der Widerstand gegen die Bewegung einer starren Kugel in einer zähen Flüssigkeit, die zwischen zwei parallelen ebenen Wänden eingeschlossen ist*. Annalen der Physik, 1922. **373**(10): p. 89-119.
43. Segre, G. and A. Silberberg, *Radial Particle Displacements in Poiseuille Flow of Suspensions*. Nature, 1961. **189**(4760): p. 209-210.
44. Segré, G. and A. Silberberg, *Behaviour of macroscopic rigid spheres in Poiseuille flow Part 2. Experimental results and interpretation*. Journal of Fluid Mechanics, 1962. **14**(1): p. 136-157.
45. Segré, G. and A. Silberberg, *Behaviour of macroscopic rigid spheres in Poiseuille flow Part 1. Determination of local concentration by statistical analysis of particle passages through crossed light beams*. Journal of Fluid Mechanics, 1962(14(1)): p. 115-135.
46. Saffman, P.G., *The lift on a small sphere in a slow shear flow*. Journal of Fluid Mechanics, 1965
22(2): p. 385-400.
47. Saffman, P.G., *The lift on a small sphere in a slow shear flow - Corrigendum*. Journal of Fluid Mechanics, 1968. **31**(3): p. 624-624.
48. Stone, H.A., *Philip Saffman and viscous flow theory*. Journal of Fluid Mechanics, 2000. **409**: p. 165-183.
49. ho, B.P., *Inertial migration of rigid spheres in two-dimensional unidirectional flows*. Journal of Fluid Mechanics, 1974. **65**(2): p. 365-400.

50. Martel, J.M. and M. Toner, *Inertial focusing in microfluidics*. *Annu Rev Biomed Eng*, 2014. **16**: p. 371-96.
51. Schonberg, J.A. and E.J. Hinch, *Inertial migration of a sphere in Poiseuille flow*. *Journal of Fluid Mechanics*, 1989. **203**: p. 517-524.
52. Hogg, A.J., *The inertial migration of non-neutrally buoyant spherical particles in two-dimensional shear flows*. *Journal of Fluid Mechanics*, 1994. **272**: p. 285-318.
53. Asmolov, E.S., *The inertial lift on a spherical particle in a plane Poiseuille flow at large channel Reynolds number*. *Journal of Fluid Mechanics*, 1999. **381**: p. 63-87.
54. Di Carlo, D., et al., *Particle segregation and dynamics in confined flows*. *Phys Rev Lett*, 2009. **102**(9): p. 094503.
55. Leal, L.G., *Creeping Flow – Two-Dimensional and Axisymmetric Problems*, in *Advanced Transport Phenomena: Fluid Mechanics and Convective Transport Processes*. 2007, Cambridge University Press: Cambridge. p. 429-523.
56. Liu, C., et al., *A generalized formula for inertial lift on a sphere in microchannels*. *Lab on a Chip*, 2016. **16**(5): p. 884-892.
57. Rubinow, S.I. and J.B. Keller, *The transverse force on a spinning sphere moving in a viscous fluid*. *Journal of Fluid Mechanics*, 1961. **11**(03): p. 447.
58. Wick, G.L. and P.F. Tooby, *Centrifugal buoyancy forces*. *American Journal of Physics*, 1977. **45**(11): p. 1074-1076.
59. Lee, D.J., et al., *Multiplex particle focusing via hydrodynamic force in viscoelastic fluids*. *Sci Rep*, 2013. **3**: p. 3258.
60. Ahn, S.W., et al., *Microfluidic particle separator utilizing sheathless elasto-inertial focusing*. *Chemical Engineering Science*, 2015. **126**: p. 237-243.

61. Ramachandraiah, H., et al., *Dean flow-coupled inertial focusing in curved channels*. *Biomicrofluidics*, 2014. **8**(3): p. 034117.
62. Xiang, N., et al., *Fundamentals of elasto-inertial particle focusing in curved microfluidic channels*. *Lab on a Chip*, 2016. **16**(14): p. 2626-2635.
63. Zheng, S., et al., *Membrane microfilter device for selective capture, electrolysis and genomic analysis of human circulating tumor cells*. *J Chromatogr A*, 2007. **1162**(2): p. 154-61.
64. Chen, Z., et al., *Pool-dam structure based microfluidic devices for filtering tumor cells from blood mixtures*. *Surface and Interface Analysis*, 2006. **38**(6): p. 996-1003.
65. Kang, T.G., et al., *A continuous flow micro filtration device for plasma/blood separation using submicron vertical pillar gap structures*. *Journal of Micromechanics and Microengineering*, 2014. **24**(8): p. 087001.
66. Zhou, J. and I. Papautsky, *Fundamentals of inertial focusing in microchannels*. *Lab Chip*, 2013. **13**(6): p. 1121-32.
67. Cherukat, P. and J.B. McLaughlin, *The inertial lift on a rigid sphere in a linear shear flow field near a flat wall*. *Journal of Fluid Mechanics*, 1994. **263**: p. 1-18.
68. Chun, B. and A.J.C. Ladd, *Inertial migration of neutrally buoyant particles in a square duct: An investigation of multiple equilibrium positions*. *Physics of Fluids*, 2006. **18**(3): p. 031704.
69. Clime, L., et al., *Twin tubular pinch effect in curving confined flows*. *Scientific Reports*, 2015. **5**: p. 9765.

70. Martel-Foley, J.M., *Inertial Microfluidic Cell Separation*, in *Microtechnology for Cell Manipulation and Sorting*, W. Lee;, P. Tseng;, and D.D. Carlo;, Editors. 2017, Springer International Publishing. p. 193-223.
71. Martel, J.M. and M. Toner, *Particle Focusing in Curved Microfluidic Channels*. Scientific Reports, 2013. **3**(1).
72. Gossett, D.R. and D. Di Carlo, *Particle focusing mechanisms in curving confined flows*. Anal Chem, 2009. **81**(20): p. 8459-65.
73. Squires, T.M. and S.R. Quake, *Microfluidics: Fluid physics at the nanoliter scale*. Reviews of Modern Physics, 2005. **77**(3): p. 977-1026.
74. Di Carlo, D., *Inertial microfluidics*. Lab Chip, 2009. **9**(21): p. 3038-46.
75. Di Carlo, D., et al., *Continuous inertial focusing, ordering, and separation of particles in microchannels*. Proceedings of the National Academy of Sciences, 2007. **104**(48): p. 18892-18897.
76. Bara, B., K. Nandakumar, and J.H. Masliyah, *An experimental and numerical study of the Dean problem: flow development towards two-dimensional multiple solutions*. Journal of Fluid Mechanics, 1992. **244**: p. 339-376.
77. Turgeon, M.L., *Clinical Hematology: Theory and Procedures*. 2004: Lippincott Williams & Wilkins.
78. Miller, M.C., G.V. Doyle, and L.W. Terstappen, *Significance of Circulating Tumor Cells Detected by the CellSearch System in Patients with Metastatic Breast Colorectal and Prostate Cancer*. J Oncol, 2010. **2010**: p. 617421.

79. Guo, Q., S.P. Duffy, and H. Ma, *Microfluidic Technologies for Deformability-Based Cell Sorting*, in *Microtechnology for Cell Manipulation and Sorting*, W. Lee, P. Tseng, and D. Di Carlo, Editors. 2017, Springer International Publishing: Cham. p. 225-254.
80. Lee, W., P. Tseng, and D. Di Carlo, *Microfluidic Cell Sorting and Separation Technology*, in *Microtechnology for Cell Manipulation and Sorting*, W. Lee, P. Tseng, and D. Di Carlo, Editors. 2017, Springer International Publishing: Cham. p. 1-14.
81. Priye, A., *Membraneless high throughput separation*. not yet published.
82. Sangani, A.S., A. Acrivos, and P. Peyla, *Roles of particle-wall and particle-particle interactions in highly confined suspensions of spherical particles being sheared at low Reynolds numbers*. *Physics of Fluids*, 2011. **23**(8): p. 083302.
83. Khoo, B.L., et al., *Clinical validation of an ultra high-throughput spiral microfluidics for the detection and enrichment of viable circulating tumor cells*. *PLoS One*, 2014. **9**(7): p. e99409.
84. Guckenberger, D.J., et al., *Micromilling: a method for ultra-rapid prototyping of plastic microfluidic devices*. *Lab Chip*, 2015. **15**(11): p. 2364-78.
85. Wan, A.M., T.A. Moore, and E.W. Young, *Solvent Bonding for Fabrication of PMMA and COP Microfluidic Devices*. *J Vis Exp*, 2017(119).
86. Ng, S.P., F.E. Wiria, and N.B. Tay, *Low Distortion Solvent Bonding of Microfluidic Chips*. *Procedia Engineering*, 2016. **141**: p. 130-137.
87. Li, C., et al., *Isoelectric focusing in cyclic olefin copolymer microfluidic channels coated by polyacrylamide using a UV photografting method*. *ELECTROPHORESIS*, 2005. **26**(9): p. 1800-1806.

88. Warkiani, M.E., et al., *Slanted spiral microfluidics for the ultra-fast, label-free isolation of circulating tumor cells*. Lab Chip, 2014. **14**(1): p. 128-37.
89. Wan, A.M., A. Sadri, and E.W. Young, *Liquid phase solvent bonding of plastic microfluidic devices assisted by retention grooves*. Lab Chip, 2015. **15**(18): p. 3785-92.
90. Lai, D., et al., *Simple Multi-level Microchannel Fabrication by Pseudo-Grayscale Backside Diffused Light Lithography*. RSC Adv, 2013. **3**(42): p. 19467-19473.
91. Kang, M., et al., *Fabrication of functional 3D multi-level microstructures on transparent substrates by one step back-side UV photolithography*. RSC Adv., 2017. **7**(22): p. 13353-13361.
92. Martel, J.M., *Inertial Focusing in Microfluidics*. Vol. 16. 2014. 371-396.
93. Zhang, J., et al., *Fundamentals and applications of inertial microfluidics: a review*. Lab on a Chip, 2016. **16**(1): p. 10-34.

APPENDIXES

Simulation Movie clip

S1. Top view of particle simulation [Figure 3-3]

S2. Cross section view along main-flow direction: Quasi-inertial focusing [Figure 3-12]

S3. Cross section view along main-flow direction: Dean vortices dominant [Figure 3-12]